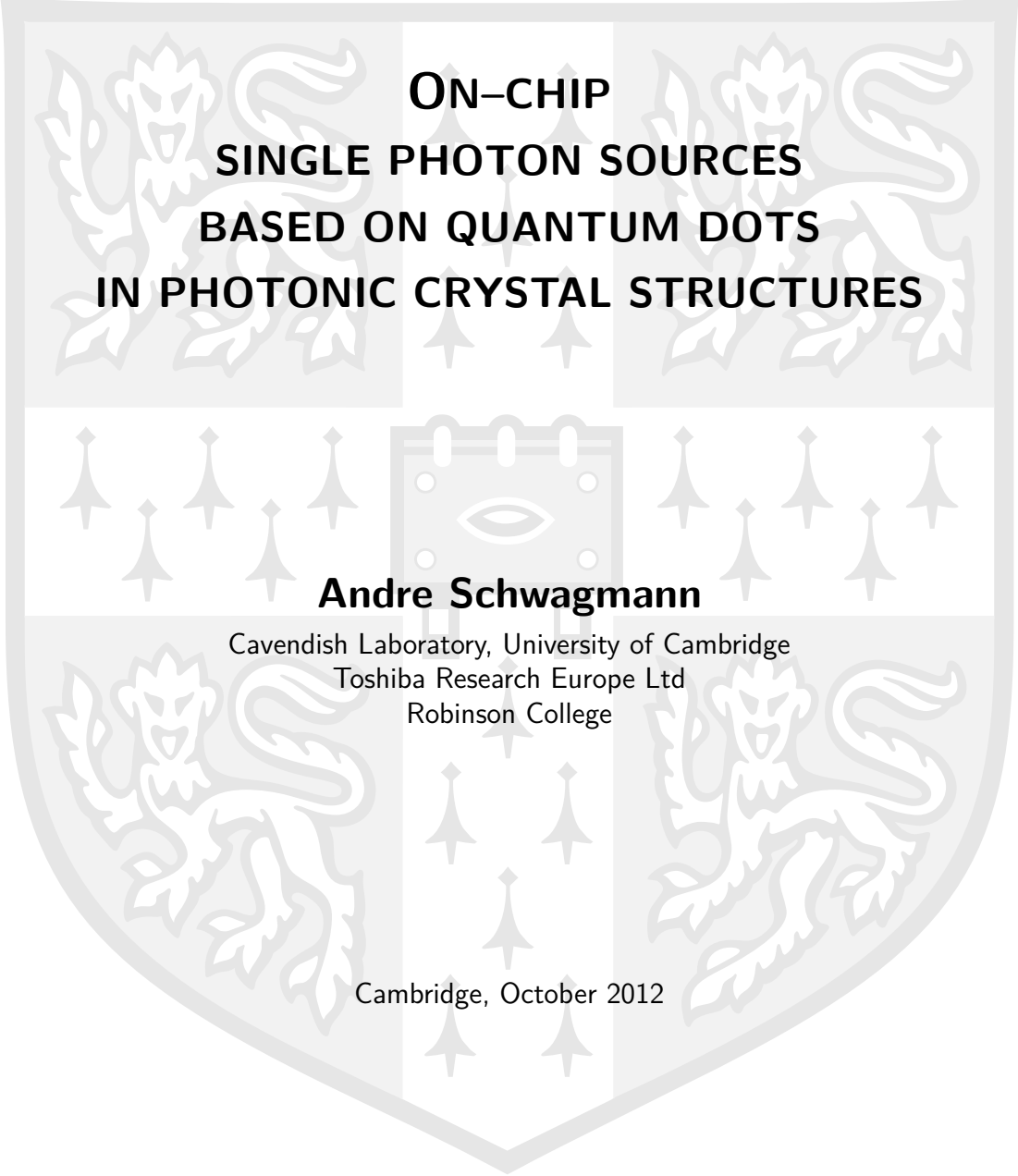


Dissertation

for the degree of Doctor of Philosophy



**ON-CHIP
SINGLE PHOTON SOURCES
BASED ON QUANTUM DOTS
IN PHOTONIC CRYSTAL STRUCTURES**

Andre Schwagmann

Cavendish Laboratory, University of Cambridge
Toshiba Research Europe Ltd
Robinson College

Cambridge, October 2012

University of Cambridge

Cavendish Laboratory

Declaration

This dissertation describes original work carried out in the Semiconductor Physics Group at the Cavendish Laboratory and at the Cambridge Research Laboratory of Toshiba Research Europe Ltd, from October 2009 to October 2012.

Except where otherwise stated this dissertation is the result of my own work. It has not been submitted in part, or as a whole, for any degree at any university. It does not exceed 60 000 words.

Andre Schwagmann

Cambridge, October 2012

Acknowledgements

This work would not have been possible without the help and expertise of a number of people. In particular, I would like to thank...

- Dave Ritchie and Andrew Shields for giving me the opportunity to work on this project at two world-class institutions; for helpful guidance, support and encouragement during my work; for giving me a lot of freedom in pursuing ideas; for proof-reading this dissertation; and for support in attracting funding.
- Sokratis Kalliakos for his help with all optical measurements taken in the photonics lab; for many helpful discussions; for good company during long hours in the lab; and for proof-reading this dissertation.
- Jon Griffiths and Geb Jones for performing the electron beam lithography for the photonic crystals; for their patience with and ambitious work on sorting out the various challenges we faced; for many long and late hours they spent getting samples done just in time; and for proof-reading parts of this dissertation.
- Dave Ellis for his help with the dry etching processes; for keeping the etching facilities going; for proof-reading parts of this dissertation; and for helpful discussions.
- Joanna Skiba-Szymanska for her help with the processing of PIN diodes; for the raw data for the atomic force micrograph shown in Figure 3.1 b; for helpful discussions; for critical comments on the figures contained in this report; and for good company.
- Ian Farrer for the molecular beam epitaxial growth of all the wafers used in this project; for his keen interest in the project; and for proof-reading parts of this dissertation.
- Anthony Bennett for sharing his deep understanding of the physics of quantum dots; for many helpful and insightful discussions; and for proof-reading parts of this dissertation.
- Sam Dewhurst for introducing me to the project; and for a very well prepared handover.
- Cameron Salter for the raw data for Figure 2.2 b and for good company at Toshiba.
- Martin Ward, Mark Stevenson, and Niklas Sköld for their help with and advice on experimental issues on various occasions.

- Ken Cooper and Melanie Tribble for training and advice in all matters concerning sample processing and the cleanroom; for performing the final cleaning etch on all photonic crystal samples used in this work; and for keeping the cleanroom facilities running.
- Andy Croxall, Deepyanti Taneja , Bo Zheng, and Francois Sfigakis for advice on using polyimide.
- Jon Rickard, Eric Tapley, and Richard Langford for training and advice on the scanning electron microscope and for keeping the microscopy facilities running.
- Richard Hobbs and Neil Baker at Toshiba and Andrew Alderwick at the Cavendish for keeping the IT facilities running.
- Emma Faid, Fiona Winter, Kim Cole, and Teri Bartlett at the Cavendish and Linda Price, Will Dunn, and Carol Meldrum at Toshiba for excellent secretarial support.
- Adrian Chan, Matt Pooley, Raj Patel, Antoine Boyer de la Giroday, Frederick Floether, Rob Taylor and many more fellow CASE students for good company and making working at Toshiba thoroughly enjoyable.

I would like to extend my special gratitude to Yang Zou and my family for their love, encouragement and support both in good and difficult times.

Financial support for this work was generously provided by the Engineering and Physical Sciences Research Council, the Semiconductor Physics Group, Toshiba Research Europe Ltd, the Cambridge European Trust, the Thomas Gessmann-Stiftung, the Richard-Winter-Stiftung, and the Kurt Hahn Trust.

Publications

Aspects of this dissertation have appeared or will appear in form of the following journal articles and contributed talks at international conferences.

Articles

A. Schwagmann, S. Kalliakos, I. Farrer, J. P. Griffiths, G. A. C. Jones, D. A. Ritchie, and A. J. Shields. “On-chip single photon emission from an integrated semiconductor quantum dot into a photonic crystal waveguide.” *Applied Physics Letters* **99**, 261108 (2011).

A. Schwagmann, S. Kalliakos, D. J. P. Ellis, I. Farrer, J. P. Griffiths, G. A. C. Jones, D. A. Ritchie, and A. J. Shields. “In-plane single-photon emission from a L3 cavity coupled to a photonic crystal waveguide.” *Optics Express* **20**, 28614 (2012).

Conference contributions

S. Kalliakos, A. Schwagmann, I. Farrer, J. P. Griffiths, G. A. C. Jones, D. A. Ritchie, and A. J. Shields. “On-chip transmission of non-classical light from an integrated quantum emitter.” *Conference on Lasers and Electro-Optics 2012*, San Jose (USA), 6 May 2012.

A. Schwagmann, S. Kalliakos, I. Farrer, J. P. Griffiths, G. A. C. Jones, D. A. Ritchie, and A. J. Shields. “Slow-light enhanced on-chip single photon emission from an InAs quantum dot into a photonic crystal waveguide.” *International Conference on Quantum Dots 2012*, Santa Fe (USA), 17 May 2012.

S. Kalliakos, A. Schwagmann, I. Farrer, J. P. Griffiths, G. A. C. Jones, D. A. Ritchie, and A. J. Shields. “On-chip generation and transmission of non-classical light from an InAs quantum dot.” *International Conference on the Physics of Semiconductors 2012*, Zurich (Switzerland), 31 July 2012.

Abstract

In order to harness the enormous potential of schemes in optical quantum information processing, readily scalable photonic circuits will be required. A major obstacle for this scalability is the monolithic integration of quantum light sources with the photonic circuit on a single chip.

This dissertation presents the experimental demonstration of different in-plane single photon sources that allow for this integration with planar light circuits. To this end, the spontaneous recombination of excitons in single indium arsenide quantum dots was exploited to generate single photons. The emission into on-chip waveguides was achieved by the use of advanced two-dimensional photonic crystal structures. First, slow-light effects in a unidirectional photonic crystal waveguide were exploited to achieve on-demand single photon emission with a rate of up to 18.7 MHz, corresponding to a remarkable estimated internal device efficiency of up to 47%. Waveguide-coupled L3 defect cavities with record Q -factors of up to 5 150 were then studied for improved Purcell enhancement of the emission, and in-plane single photon generation from such a device was demonstrated. Finally, an electrically tunable, integrable quantum light source with a total tuning range of 1.9 nm was demonstrated by exploiting the quantum-confined Stark effect in an electrical PIN diode.

These results are the first demonstrations of in-plane single photon emission at optical wavelengths and mark an important cornerstone for the realisation of fully integrated quantum photonic circuits in optical quantum information science.

Contents

Declaration	III
Acknowledgements	V
Publications	VII
Abstract	IX
1 Introduction and motivation	1
2 Theoretical background	3
2.1 Semiconductor quantum dots as single photon sources	3
2.1.1 Electronic structure of indium arsenide quantum dots	3
2.1.2 Optical properties of indium arsenide quantum dots	5
2.2 Cavity quantum electrodynamics with quantum dots	7
2.2.1 Characteristics of optical cavities	7
2.2.2 Quantum dot–cavity coupling	9
2.2.3 Design principles for quantum dot–cavity systems	12
2.3 Photonic crystal-based solid state cavities	14
2.3.1 Properties of defect-free photonic crystals	14
2.3.2 Microcavities in photonic crystal systems	17
2.3.3 Two-dimensional photonic crystal slabs	19
2.3.4 Defects in two-dimensional photonic crystal slabs	23
3 Methods	27
3.1 Simulation tools	27
3.1.1 Finite-difference time-domain simulations	27
3.1.2 Plane wave expansion simulations	29
3.2 Device fabrication	30
3.2.1 Sample growth with molecular beam epitaxy	31
3.2.2 Fabrication of photonic crystal slabs	33
3.3 Optical characterisation	38
3.3.1 Micro-photoluminescence spectroscopy	39

3.3.2	Time-resolved photoluminescence spectroscopy	40
3.3.3	Hanbury Brown and Twiss interferometry	42
4	Slow-light enhanced on-chip quantum light source	45
4.1	Slow-light effects in photonic crystal waveguides	45
4.1.1	Discussion of design parameters	50
4.2	Experimental demonstration of an in-plane single photon source	52
4.2.1	Spectral characterisation	53
4.2.2	Time-resolved photoluminescence and the Purcell effect	56
4.2.3	Photon statistics	57
5	Waveguide-coupled L3 cavities for on-chip single photon emission	63
5.1	Mode structure of the stand-alone L3 defect cavity	64
5.1.1	Optimisation of the design parameters for the M_0 mode of the L3 defect cavity	69
5.2	Coupling of the L3 defect cavity to a waveguide	71
5.2.1	Fundamental requirements for cavity–waveguide coupling	71
5.2.2	Cavity–waveguide separation	73
5.3	On-chip single photon emission from a quantum dot in a waveguide-coupled L3 defect cavity	77
6	Electrically controllable on-chip single photon sources	83
6.1	Quantum-confined Stark effect	84
6.2	Device design and nanofabrication	86
6.3	Electrically tunable in-plane single photon emission	89
6.3.1	Device A: tuning range of 1.3 nm	90
6.3.2	Device B: tuning range of 1.9 nm	92
7	Summary and outlook	97
	Bibliography	XIII

1 Introduction and motivation

The famous Moore's Law states that the density of transistors that can be manufactured at minimum component cost doubles every 12-18 months [1]. Remarkably, the miniaturisation of digital electronic devices has approximately kept pace with this prediction ever since it was established in 1965 [2]. However, as devices are getting smaller and smaller, device performance will increasingly be limited by quantum mechanical effects [3]. Turning this problem on its head, the emerging field of quantum information science aims to *exploit* rather than *avoid* quantum mechanical effects for information processing [4]. A particularly appealing concept in this field is the quantum computer, which would exponentially outperform current computing technology for certain tasks such as factorising and database search [5, 6].

A number of promising physical implementations of such a quantum computer are being developed [7, 8], but using single photons as quantum bits by encoding information on polarisation, time bin or path has emerged as one of the leading approaches owing to their insensitivity to decoherence and ease of manipulation [9]. Early proposals for optical quantum computation required strong optical non-linearities [10] that are not available with current materials [9], but seminal work in 2001 showed that linear optical quantum computation is possible using only single photon sources, beamsplitters, phaseshifters and photodetectors [11]. Experimental demonstrations of this concept [12] have so far been restricted to logical operations involving a few photons that were externally fed into setups comprising bulk optics [13, 14] or waveguide circuits [15, 16]. However, scaling to useful devices with larger photon numbers will require single photon sources that can be monolithically implemented into fully integrated quantum photonic circuits [9]. This work is concerned with the experimental study, development and demonstration of such integrable in-plane single photon sources.

Single photons can be generated using a number of different physical processes [17], but in this work the spontaneous recombination of electron-hole pairs in semiconductor quantum dots is employed as it is uniquely suited for the seamless integration with mature semiconductor technology [18]. Quantum dots are also attractive single photon sources because they allow for electrical excitation [19, 20], offer excellent emission efficiencies [21], and can generate indistinguishable single photons on-demand [22]. Both the efficiency of the source and the photon indistinguishability, which is indispensable for schemes in linear optical quantum computation as they rely on two-photon interference [23, 24], can be improved by cavity quantum electrodynamic effects such as Purcell enhancement [18, 25]. To this end, this work

is concerned with the study of defects in photonic crystals, which are materials with a periodic variation of the refractive index [26], since they are particularly well suited for exploiting cavity quantum electrodynamics [27]. Simultaneously, they allow for on-chip waveguiding, which makes them very attractive systems for the realisation of integrable in-plane single photon sources with semiconductor quantum dots [28].

The outline of this dissertation is as follows: this introduction is followed by a discussion of the theoretical background in Chapter 2. The relevant concepts regarding semiconductor quantum dots, cavity quantum electrodynamics, and photonic crystals are introduced there. This is followed by Chapter 3, which presents the methods used in this work. This includes a discussion of the tools used to simulate photonic crystal structures, as well as the nanofabrication techniques employed to fabricate devices, and the experimental techniques used to optically characterise these devices. The first demonstration of an integrable in-plane single photon source at optical wavelengths is presented in Chapter 4, where slow-light effects in photonic crystal waveguides are exploited to Purcell-enhance the single photon emission. The device concept is refined in Chapter 5, where the superior properties of point defect cavities for Purcell enhancement are combined with the on-chip light guiding of photonic crystal waveguides. In-plane single photon emission from such a device is demonstrated as well. In Chapter 6, the quantum-confined Stark effect is exploited to electrically tune the emission wavelength of in-plane single photon sources. This dissertation concludes with a summary and an outlook to possible future research directions in Chapter 7.

2 Theoretical background

In this chapter, the theoretical underpinnings of the three main physical concepts studied in this dissertation are discussed. The first section covers the properties of semiconductor quantum dots which lead to the efficient generation of single photons. This is followed by a discussion of cavity quantum electrodynamics with quantum dots, with a focus on the Purcell effect. Finally, the third section is dedicated to photonic crystals in general, and to defects in two-dimensional photonic crystal slabs in particular.

2.1 Semiconductor quantum dots as single photon sources

In semiconductor quantum dots, charge carriers are confined in all three spatial directions to dimensions on the order of their de Broglie wavelength [29]. Among the various fabrication techniques [29–32], epitaxially grown self-assembled quantum dots [33, 34], which are studied in this work, provide particularly strong carrier confinement [35]. Self-assembled quantum dots have been demonstrated with a range of semiconductor systems, such as group IV heterostructure systems (Ge/Si [36]), group III-V semiconductor compounds (InP/InGaP [37], InGaN/GaN [38]), and group II-VI heterostructure systems (CdSe/ZnSe [39]), but self-assembled indium arsenide quantum dots in a gallium arsenide matrix remain the most widely studied [40]. Since small indium arsenide quantum dots have been shown to be excellent sources of single photons [18], this material system is used in this work as well. The origin of the carrier confinement in indium arsenide quantum dots and the resulting electronic properties are discussed in the first subsection, whereas their optical properties will be discussed in a second subsection.

2.1.1 Electronic structure of indium arsenide quantum dots

Most of the interesting properties of semiconductor quantum dots can be understood by analysing the band structure of the system. The indium arsenide quantum dots in a gallium arsenide matrix studied here are type I dots, i.e. the quantum dots' valence (conduction) band edge is higher (lower) in energy than that of the surrounding gallium arsenide matrix such that they trap both electrons and holes [41]. In its pure form, gallium arsenide has a band gap energy of 1.42 eV, while indium arsenide exhibits a much smaller band gap energy of 0.35 eV (both values at 300 K [42]). However, the indium arsenide in the quan-

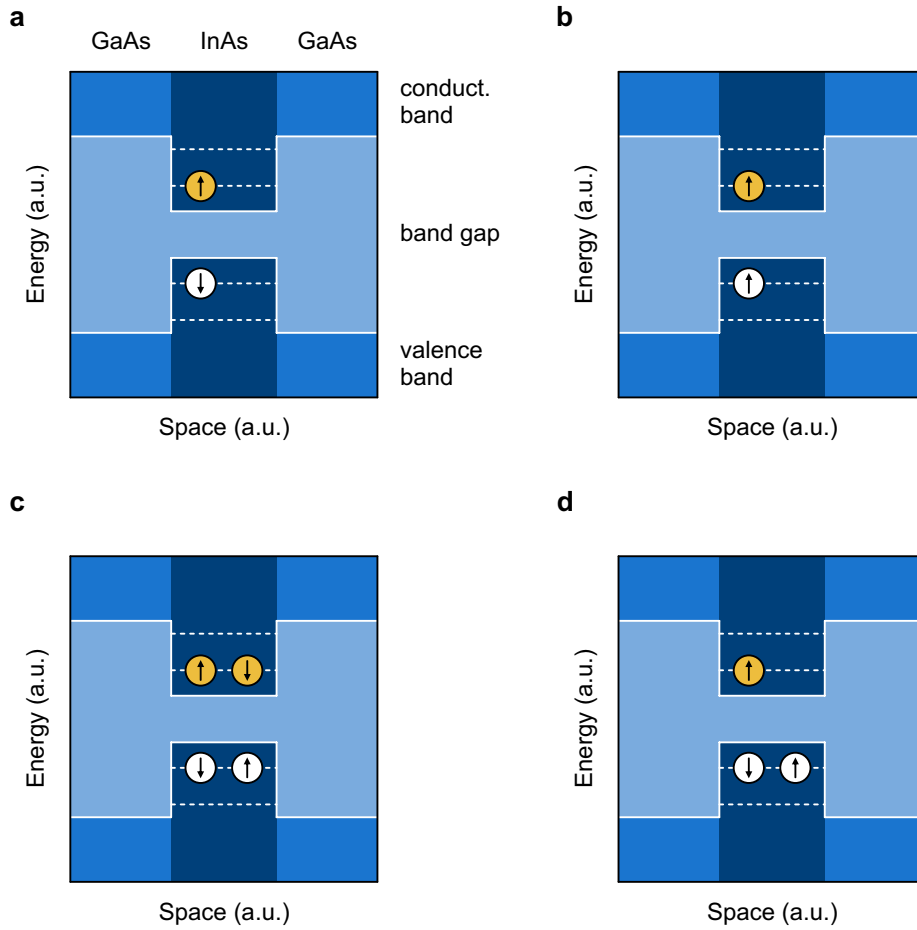


Figure 2.1 | Simplified schematic of the band structure of indium arsenide quantum dots in a gallium arsenide matrix. Shown are exemplary electronic states of the quantum dot. **a**, Neutral exciton. **b**, Dark exciton. **c**, Neutral biexciton. **d**, Positively charged exciton.

tum dot is coherently strained [43] (see also Section 3.2.1), which leads to a complex band structure in general and to a considerably larger band gap for the material in the quantum dot in particular [44]. Moreover, the quantum dot does not consist of pure indium arsenide as there is a diffusion of gallium atoms during the growth process, resulting in a gradient of gallium composition in the quantum dot, further increasing its overall band gap energy [45]. In a first approximation, the band structure of the system can nevertheless be represented by a step-like change in the electronic band gap, as illustrated in Fig. 2.1. The confinement of charge carriers in the indium arsenide quantum dot provided by the surrounding energy barrier, i.e. the larger band gap energy of the gallium arsenide matrix, leads to a quantisation of energy states within the quantum dot [46]. The combination of strain, gallium composition, and confinement quantisation leads to a lowest energy level separation for electron and hole states of about 1.37 eV for the dots studied here [47]. Experiments with similar

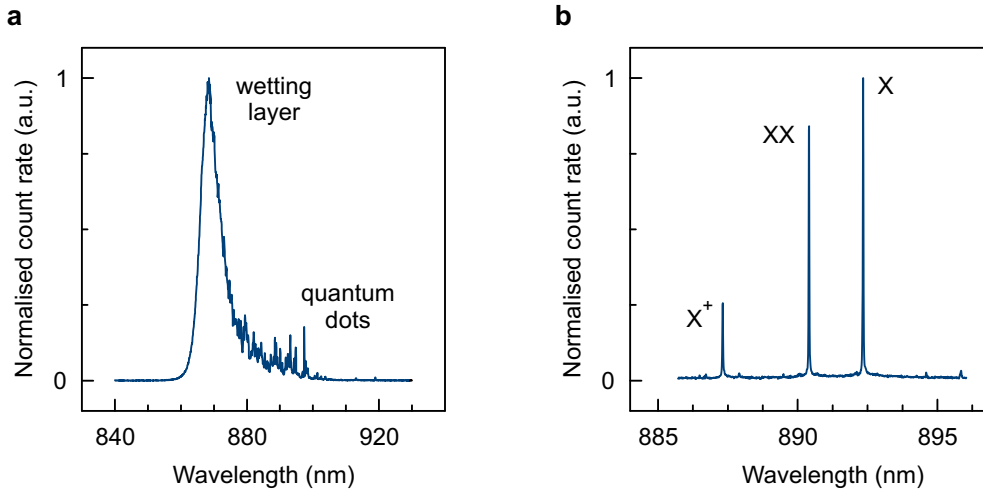


Figure 2.2 | Typical photoluminescence spectra of indium arsenide quantum dots grown in the Stranski-Krastanow growth mode. **a**, Spectrum of an ensemble of dots, exhibiting the bright wetting layer and many different quantum dot transitions. **b**, Spectrum of a single dot, exhibiting sharp, characteristic transitions for the neutral exciton (X), the neutral biexciton (XX) and the positively charged exciton (X^+) states.

dots furthermore showed that a single quantum dot contains only one to two energy levels for electrons and holes, respectively [47]. Since the Pauli exclusion principle applies to the fermionic charge carriers, each discrete energy level can accommodate up to two charge carriers of opposite spin. This electronic structure leads to interesting optical properties, which are discussed in the following subsection.

2.1.2 Optical properties of indium arsenide quantum dots

Since this work aims to exploit quantum dots as single photon sources, this subsection will concentrate on the optical properties of indium arsenide quantum dots. Due to the direct band gap of indium arsenide [48], the efficient radiative relaxation of excited states of the quantum dot is possible. These excited states can be generated by the injection of charge carriers, which can be achieved electrically [19, 49] or optically [50], and pulsed or continuously [51]. The excitation might be non-resonant, where charge carriers are generated in the surrounding bulk gallium arsenide and relax into the wetting layer and the discrete energy states of the quantum dot via the Auger effect or via scattering by acoustic phonons [20, 51]; quasi-resonant via the creation of a phonon [52, 53]; or resonant by exciting a specific transition in the quantum dot selectively [51, 54]. Regardless of the excitation mechanism, the excited charge carriers in the quantum dot typically recombine spontaneously after a radiative lifetime τ of about 1 ns for the exciton state [51]. Since the photons' energies are lower

than the band gap energy of the surrounding gallium arsenide matrix, they can propagate through the material without being reabsorbed and eventually escape from the sample. A typical spectrum, for which an ensemble of indium arsenide quantum dots was probed by non-resonant excitation, is presented in Fig. 2.2 a. The spectrum exhibits a bright peak at about 870 nm, which is attributed to emission from the wetting layer resulting from the epitaxial growth mode (see also Section 3.2.1). In the wavelength range from 875 nm to about 900 nm, a collection of many distinct transitions can be observed. This is emission from the ensemble of quantum dots that is probed. The emission characteristics of a single quantum dot will be discussed in the following paragraph.

Due to the Pauli exclusion principle, the number of different possible excitonic configurations in a quantum dot is limited. Some of these states are illustrated in Fig. 2.1. The neutral exciton (X , Fig. 2.1 a) consists of a single electron and hole of opposite spin, such that radiative recombination of these charge carriers is dipole allowed, releasing the excitonic energy in form of a single photon. Another possible configuration is the dark exciton state (X_{dark} , Fig. 2.1 b), where radiative recombination is dipole forbidden due to parallel spins of the electron and hole. The population of the quantum dot by two electron-hole pairs leads to the formation of a neutral biexciton (XX , Fig. 2.1 c), which can recombine radiatively emitting two photons successively [47]. Due to Coulomb interaction between the biexciton's charge carriers in the quantum dot, the two photons of the recombination cascade of a biexciton have slightly different energies. Finally, charged excitonic states are also possible when different numbers of electrons and holes populate the corresponding states in the quantum dot. An example is the positively charged exciton (X^+) shown in Fig. 2.1 d. Similar to the (neutral) biexciton recombination cascade, photons emitted due to radiative recombination of charged states have different energies as compared to those emitted from the corresponding neutral states because of Coulomb interaction between the charge carriers. A typical spectrum of a single quantum dot is shown in Fig. 2.2 b. As a result of the discretisation of the energy levels in the quantum dot, it exhibits very sharp transitions. The transitions corresponding to the exciton, the biexciton and the positively charged exciton states appear at decreasing wavelengths, i.e. at increasing photon energies, due to the Coulomb interaction.

A combination of two factors makes quantum dots attractive as single photon sources. First, the emission that results from the radiative recombination cascade of an excited quantum dot are spectrally distinguishable, allowing for the selection of a particular transition. Secondly, after spontaneous radiative recombination, a quantum dot cannot immediately emit another photon of the same energy since the quantum dot is not in the required excited state. Another photon of the same energy can only be emitted after repopulation of the corresponding excited state [55]. This leads to the generation of a stream of single photons of a particular energy. Moreover, the radiative lifetime of excitonic states in the quantum dot is much longer than the free carrier lifetime in the surrounding bulk gallium

arsenide [51]. This prohibits the refilling of quantum dot states immediately after radiative recombination if a pulsed excitation scheme with a pulse duration shorter than the radiative lifetime is employed [20, 21]. Pulsed excitation of the quantum dot can therefore further improve the single photon statistics and give deterministic control over the repetition rate of the single photon emission.

This concludes the discussion of the properties of semiconductor quantum dots, which has identified them as attractive sources of single photons. The following section will discuss cavity quantum electrodynamic effects, which can be exploited to improve the source efficiency and the indistinguishability of the single photons emitted by quantum dots.

2.2 Cavity quantum electrodynamics with quantum dots

This section will discuss cavity quantum electrodynamics, which describes the enhanced interaction between light and matter when confined inside a resonant cavity. The resulting effects can be exploited to increase the efficiency of single photon sources, and are important for rendering single photons indistinguishable [18]. After introducing the basic characteristics of optical cavities in the first subsection, the interaction between a quantum dot and an optical cavity is discussed for the weak coupling regime, resulting in Purcell enhancement. This is followed by a brief description of the strong coupling regime. This section concludes with a discussion of the design rules for quantum dot–cavity systems that can be deduced from the preceding theoretical discussion.

2.2.1 Characteristics of optical cavities

An ideal optical cavity is essentially a volume surrounded by perfectly reflective material. The properties of an optical cavity can be analysed by introducing light fields into the cavity. The light is strongly confined to that cavity, as it is reflected at its boundaries and repeatedly propagates through the cavity. During this process, fields of certain frequencies, which depend on the geometry of the cavity, may interfere constructively. This leads to a strongly increased intensity of these light fields. The corresponding frequencies ω_{cav} are called resonant frequencies of the optical cavity, and they are key parameters to characterise its properties. On the contrary, light fields with frequencies other than the resonant frequencies ultimately interfere destructively after a number of reflections at the boundaries of the cavity. Consequently, the intensity of these fields with off-resonant frequencies is strongly suppressed. Hence, for an ideal cavity, there is a set of δ -like resonant modes, i.e. modes of a light field that are preferentially selected by a cavity, at frequencies ω_{cav} . It is noteworthy that this selection of modes by the cavity is equivalent to a redistribution of the free-space optical density of states into the resonant modes, where it is consequently very large, while it is strongly reduced to negligible levels off-resonance.

Neglecting absorption in the cavity volume, the perfectly reflective boundaries of an ideal optical cavity entail that a certain number of photons N_0 , once inserted into a resonant mode, will stay in that cavity forever, i.e. the photon lifetime in the cavity τ_{cav} is infinite. However, for a real optical cavity, the boundaries are never perfectly reflective. This leads to a finite photon lifetime, and the time evolution of the number of photons in a cavity $N(t)$ can be described by [56]

$$N(t) = N_0 \exp\left(-\frac{t}{\tau_{\text{cav}}}\right). \quad (2.1)$$

In accordance with the energy formulation of Heisenberg's uncertainty principle,

$$\Delta E \cdot \Delta t \gtrsim \hbar, \quad (2.2)$$

the finite photon lifetime in the cavity leads to lifetime broadening of the resonant modes. Setting $\Delta t = \tau_{\text{cav}}$ and $\Delta E = \hbar \cdot \Delta\omega_{\text{cav}}$, the broadening must satisfy

$$\Delta\omega_{\text{cav}} \gtrsim \frac{1}{\tau_{\text{cav}}}. \quad (2.3)$$

In fact, it can be shown [56] that the lifetime broadening $\Delta\omega_{\text{cav}}$ is *equal* to the reciprocal of the photon lifetime in the cavity, and that the resulting mode shape is described by a Lorentzian function. To account for the mode broadening due to the imperfect reflectivity of the boundaries of the cavity, the quality factor Q of a mode is defined as

$$Q = \frac{\omega_{\text{cav}}}{\Delta\omega_{\text{cav}}}. \quad (2.4)$$

The quality factor is a key parameter to characterise the properties of resonant modes in optical cavities.

While the Q -factor characterises the *spectral* (or equivalently the *temporal*) properties of a mode in an optical cavity, the effective mode volume V_{m} characterises the *spatial* extension of a cavity mode. It is defined [57] as the volume integral of the normalised electric field energy density over a quantisation volume V encompassing the resonator and a boundary in the radiation zone of the cavity mode as

$$V_{\text{m}} = \int_V \frac{\rho_{\text{e}}(\vec{r})}{\max[\rho_{\text{e}}(\vec{r})]} d^3 r, \quad (2.5)$$

where

$$\rho_{\text{e}}(\vec{r}) = \frac{1}{2} \varepsilon(\vec{r}) |\vec{E}(\vec{r})|^2 \quad (2.6)$$

is the electric field energy density and $\varepsilon(\vec{r})$ and $\vec{E}(\vec{r})$ are the dielectric function and the electric field at position \vec{r} , respectively. The effective mode volume V_{m} is typically given in units of cubic wavelengths $\left(\frac{\lambda}{n}\right)^3$.

The basic characteristics of optical cavities and their modes introduced in this subsection will be referred to frequently in the following subsections, which discuss the coupling of semiconductor quantum dots to optical cavities.

2.2.2 Quantum dot – cavity coupling

The coupling of a quantum dot to an optical cavity leads to a modification of the photon emission process. There are two different regimes of this coupling, depending on the characteristics of the cavity mode and the positioning of the quantum dot in the cavity. In the weak coupling regime, which is discussed first, the emission process remains an irreversible process, just as in an uncoupled quantum dot, but the rate of spontaneous emission is modified by the Purcell effect. This is followed by a brief discussion of the strong coupling regime, in which the photon emission is a reversible process because photons emitted into the cavity mode are reabsorbed by the quantum dot.

Weak coupling regime

For the weak coupling of a quantum dot to a cavity mode, it is instructive to directly compare the process of spontaneous emission for a quantum dot in free space and for a quantum dot coupled to a cavity mode. For both cases, it is valid to calculate the transition rate of spontaneous emission, W , by applying Fermi's golden rule [35]. According to this rule, the spontaneous emission rate is given by [58, 59]

$$W = \frac{2\pi}{\hbar} |\langle \vec{p} \cdot \vec{E} \rangle|^2 \rho(\omega), \quad (2.7)$$

where $\langle \vec{p} \cdot \vec{E} \rangle$ is the dipole transition matrix element of the transition in the quantum dot, \vec{p} is the transition dipole, \vec{E} the the electric field, and $\rho(\omega)$ is the density of final states.

In the absence of external field sources, the electric field can be assumed to be the vacuum electric field $\vec{\mathcal{E}}$. The dipole transition matrix element is then found to be [56]

$$\langle \vec{p} \cdot \vec{\mathcal{E}} \rangle = \xi \sqrt{\frac{\mu_{12}^2 \hbar \omega}{2\epsilon_0 V_m}}, \quad (2.8)$$

where μ_{12} is the transition dipole moment of the transition in the quantum dot and the normalised dipole orientation factor ξ is defined as

$$\xi = \frac{|\vec{\mathcal{E}}(\vec{r})| |\vec{p} \cdot \vec{\mathcal{E}}(\vec{r})|}{|\vec{\mathcal{E}}_{\max}| |\vec{p}| |\vec{\mathcal{E}}(\vec{r})|}. \quad (2.9)$$

Here, $\vec{\mathcal{E}}(\vec{r})$ is the vacuum field at the position \vec{r} of the quantum dot, and $\vec{\mathcal{E}}_{\max}$ is the maximum vacuum field. Please note that for obtaining this result, no assumptions on the environment of the quantum dot were made, i.e. the dipole transition matrix element takes this form for both a quantum dot weakly coupled to a cavity mode and for a quantum dot in free space.

In contrast, the density of final states, i.e. the density of optical states, differs significantly in free space and in an optical cavity. In free space, this density is found to be [56]

$$\rho_{\text{free}}(\omega) = \frac{\omega^2 V}{\pi^2 c^3}, \quad (2.10)$$

where c is the speed of light, and V a volume that is large enough not to affect the spontaneous emission process (it is needed for mathematical reasons).

One of the main features of optical cavities is the redistribution of this density of optical states into resonant optical modes. Under the assumption that there is only a single resonant cavity mode at a frequency ω_{cav} (with linewidth $\Delta\omega_{\text{cav}}$) close to the transition frequency of the quantum dot, the density of final states $\rho(\omega)$ can be approximated by a normalised Lorentzian function [56]

$$\rho_{\text{cav}}(\omega) = \frac{2}{\pi \Delta\omega_{\text{cav}}} \frac{(\Delta\omega_{\text{cav}})^2}{4(\omega - \omega_{\text{cav}})^2 + (\Delta\omega_{\text{cav}})^2}. \quad (2.11)$$

The difference between the densities of optical states in Eqns. 2.10 and 2.11 leads to different rates of spontaneous emission, which is called the Purcell effect [60]. The combination of Eqns. 2.7–2.9 and 2.11 yields the rate of spontaneous emission of a quantum dot placed in a cavity, W_{cav} . Taking into account that ξ^2 averages to $\frac{1}{3}$ for a randomly oriented dipole in free space [56], the rate of spontaneous emission of a quantum dot placed in free space, W_{free} , can analogously be obtained by combining Eqns. 2.7–2.10. The ratio of these emission rates,

$$F_{\text{P}} = \frac{W_{\text{cav}}}{W_{\text{free}}} \equiv \frac{\tau_{\text{free}}}{\tau_{\text{cav}}}, \quad (2.12)$$

is called the Purcell factor [60]. It serves as a figure of merit for the weak coupling in a quantum dot–cavity system and takes the following explicit form [61]:

$$F_{\text{P}} = \frac{3}{4\pi^2} \frac{\lambda_{\text{cav}}^3}{n^3} \frac{Q}{V_{\text{m}}} \left(\frac{|\vec{\mathcal{E}}(\vec{r})| |\vec{p} \cdot \vec{\mathcal{E}}(\vec{r})|}{|\vec{\mathcal{E}}_{\text{max}}| |\vec{p}| |\vec{\mathcal{E}}(\vec{r})|} \right)^2 \frac{(\Delta\omega_{\text{cav}})^2}{4(\omega_{\text{qd}} - \omega_{\text{cav}})^2 + (\Delta\omega_{\text{cav}})^2}, \quad (2.13)$$

where ω_{qd} is the frequency of the transition in the quantum dot. The individual components of the Purcell factor will be discussed in detail in the following subsection in order to deduce practical design principles for quantum dot–cavity systems with maximum Purcell effect.

By definition of the Purcell factor, $F_{\text{P}} > 1$ means that the spontaneous emission process is enhanced by placing the quantum dot inside a cavity (typically when the transition in the quantum dot is in resonance with the cavity mode), whereas $F_{\text{P}} < 1$ implies a suppression of spontaneous emission in the cavity as compared to a quantum dot placed in free space (typically in the off-resonance case). Hence, placing the quantum dot in a cavity gives the opportunity to tailor the process of spontaneous emission [62]. The Purcell effect is illustrated in Fig. 2.3. Figure 2.3 a shows how a quantum dot transition (labelled X) is thermo-optically tuned [63] through a cavity mode (labelled M). The corresponding time-resolved photoluminescence measurements shown in Fig. 2.3 b illustrate the Purcell effect for the quantum dot transition on- and off-resonance with the cavity mode.

The modification of the spontaneous emission process by the Purcell effect is equivalent to an angular redistribution of the emission [64–67]. This is a result of the modification of the optical density of states by the cavity, which only acts in the preferential direction of the

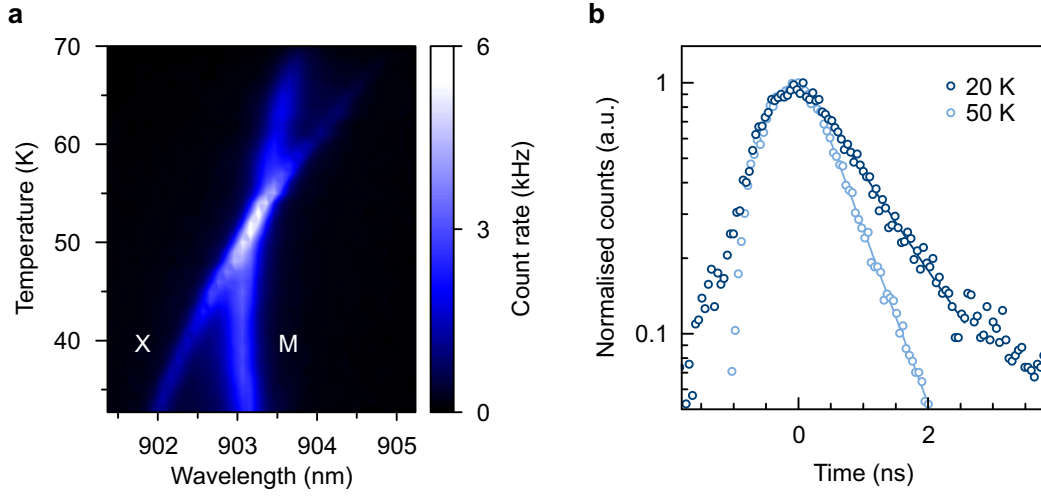


Figure 2.3 | Purcell enhancement of a quantum dot transition. All data was recorded in-plane from a waveguide-coupled L3 cavity at $T = 5$ K. **a**, Thermo-optical tuning of the quantum dot transition (X) through resonance with the cavity mode (M). This data was recorded with $P_{\text{ex}} = 66$ nW. **b**, Time resolved photoluminescence signal of the excitonic transition. Off-resonance at $T = 20$ K, the lifetime $\tau = 1.1$ ns is significantly shorter than on-resonance at $T = 50$ K, where $\tau = 0.6$ ns. This data was recorded with $P_{\text{ex}} = 0.21$ μ W.

resonant cavity mode, while it leaves the optical density of states in other directions (mostly) unaffected. This leads to a higher rate W_{cav} of spontaneous emission in the direction of the cavity mode as compared to other directions unaffected by the cavity, in which photons can be assumed to be emitted at the free space rate W_{free} . This redistribution effect is quantified by the spontaneous emission coupling factor β , which is defined as the ratio of the spontaneous emission rate into the cavity mode and the total spontaneous emission rate:

$$\beta = \frac{W_{\text{cav}}}{W_{\text{cav}} + W_{\text{free}}} \equiv \frac{F_{\text{P}}}{1 + F_{\text{P}}}. \quad (2.14)$$

This factor is always ≤ 1 and approaches unity only for an emitter perfectly coupled to an ideal cavity.

Both manifestations of the Purcell effect are very interesting for potential applications. Purcell enhancement of the spontaneous emission rate leads to a reduced time jitter and hence to more indistinguishable single photons [24] and to higher possible repetition rates for pulsed light sources based on a quantum dot-cavity system [21]. Furthermore, the angular redistribution of the emission facilitates efficient collection of the emitted photons [68].

Strong coupling regime

For the nearly ideal coupling of a transition in a quantum dot to a cavity with a sufficiently large Q -factor, strong coupling can be observed. In this regime, which is described by the Jaynes-Cummings model [69], the emission of a photon from the quantum dot into a cavity mode is a reversible process. Due to the strong confinement of light to the cavity, an emitted photon is confined to the immediate surroundings of the quantum dot for long enough to be reabsorbed by this two-level system. These oscillations between an excited state of the quantum dot and the cavity mode are called vacuum Rabi oscillations [70], and the corresponding quasi-particles are called exciton-polaritons [71]. Rabi oscillations in the time domain correspond to a splitting of energy levels in the frequency domain. Since the strong coupling between a quantum dot transition and a cavity mode collapses on detuning [72], this results in a characteristic anti-crossing as a strongly coupled quantum dot transition is spectrally tuned through the cavity mode [73–75].

Single photon sources in the strong coupling regime are expected to exhibit very high extraction efficiencies [76, 77], but the indistinguishability of the emitted photons could be compromised by spectral broadening due to the strong coupling [78].

2.2.3 Design principles for quantum dot – cavity systems

The previous subsection was concerned with the weak and strong coupling regimes of cavity quantum electrodynamics, and Purcell enhancement in the weak coupling regime was identified as highly desirable for single photon sources in quantum information processing due to the resulting increase in source efficiency and photon indistinguishability. This section aims to deduce practical design principles for quantum dot – cavity systems with maximum Purcell enhancement from the formulae derived in the preceding section. Also, experimental techniques used to meet the requirements will be pointed out briefly.

The explicit form of the Purcell factor F_P in Eqn. 2.13 can be separated into four components according to their physical meaning as follows

$$F_P = \underbrace{\frac{3}{4\pi^2} \frac{\lambda_{\text{cav}}^3}{n^3} \frac{Q}{V_m}}_{\text{cavity characteristics}} \cdot \left(\underbrace{\frac{|\vec{\mathcal{E}}(\vec{r})|}{|\vec{\mathcal{E}}_{\text{max}}|}}_{\text{spatial overlap}} \underbrace{\frac{|\vec{p} \cdot \vec{\mathcal{E}}(\vec{r})|}{|\vec{p}| |\vec{\mathcal{E}}(\vec{r})|}}_{\text{orientation alignment}} \right)^2 \cdot \underbrace{\frac{(\Delta\omega_{\text{cav}})^2}{4(\omega_{\text{qd}} - \omega_{\text{cav}})^2 + (\Delta\omega_{\text{cav}})^2}}_{\text{spectral overlap}}. \quad (2.15)$$

These four components will be discussed separately in the following.

Cavity characteristics

The resonant wavelength of the cavity λ_{cav} should ideally match the transition in the quantum dot, and is therefore restricted by the type of quantum dot used. Likewise, the refractive

index of the cavity n is defined by the material system used for the device. These two parameters are therefore in general not used as design parameters to optimise for maximum Purcell enhancement. In contrast, the cavity mode's Q -factor and mode volume V_m can be optimised by careful design of the cavity. Therefore, a first design rule is to maximise the ratio Q/V_m to allow for optimal Purcell enhancement. In practice, this is achieved by simulating cavity structures with the finite-difference time-domain technique (see Section 3.1) and thereby identifying the cavity design parameters with the most favourable Q/V_m ratio within the remaining constraints of the experiment.

Spatial overlap

In order to maximise the Purcell enhancement, the quantum dot should be placed at the position of maximum vacuum field \vec{E}_{\max} , i.e. at an anti-node of the target resonant cavity mode. In that case, the corresponding factor in Eqn. 2.15 is unity, whereas in general it is ≤ 1 . The position of these anti-nodes inside the cavity volume can also be determined by finite-difference time-domain simulations. This requirement is the most challenging since the self-assembled semiconductor quantum dots used here nucleate at random positions during growth (see section 3.2.1).

In order to address this problem, two types of approaches have been demonstrated successfully. Post-growth techniques [74, 79–83] have relied on identifying the position of randomly positioned quantum dots, and then fabricating the cavity around the quantum dot accordingly. However, these approaches are inherently not scalable and therefore of limited use for applications in quantum information processing. The desired scalability is offered by an alternative technique, which determines the sites of dot formation by patterning the substrate prior to growth [84, 85]. Devices can then be designed around these pre-defined dot sites accordingly [86]. While progress has been made in this field [85], the optical properties of these quantum dots are still poor compared to those of randomly nucleated quantum dots, which is why the latter are used in this work.

Orientation alignment

For maximum Purcell enhancement, the orientation of the electric dipole of the quantum dot transition and that of the electric field vector of the resonant mode of the cavity should be aligned in parallel. The corresponding factor in Eqn. 2.15 approaches unity for perfect alignment, while it is ≤ 1 in general. The electric dipoles of the neutral excitonic transitions in a quantum dot are oriented along precise crystallographic axes within the sample plane [87]. For efficient coupling between a quantum dot and a cavity mode, it is therefore required to design the cavity mode such that it exhibits an even parity for the electric field components with respect to the sample plane (see also Section 2.3.3).

Spectral overlap

It is intuitively clear that the coupling between a cavity mode and a quantum dot is most efficient when they are spectrally in resonance. Therefore, the spectral overlap term in Eqn. 2.15, which is always ≤ 1 , is maximum for $\omega_{\text{qd}} = \omega_{\text{cav}}$. While resonant frequencies of cavities can be designed and predicted relatively well, the emission wavelengths of semiconductor quantum dots vary within a given sample due to the self-assembly and the resulting variation in quantum dot size. This is a major obstacle for the scalability of schemes relying on two-photon interference of single photons from different sources. However, the emission wavelengths of quantum dot transitions can be tuned to a limited degree by thermo-optical [63] or – more promisingly – by electro-optical tuning [88–90].

2.3 Photonic crystal-based solid state cavities

For the cavity quantum electrodynamic effects discussed in the previous section, cavities with a small mode volume V_m and a high Q -factor are necessary. Several cavity types have been employed for this purpose [25, 91, 92], but point defects in photonic crystals are particularly attractive [27] due to their extremely small mode volumes [93] and high Q -factors [94]. Since line defects in photonic crystals furthermore allow for on-chip waveguiding, photonic crystal structures are a natural choice for the realisation of Purcell-enhanced integrable single-photon sources [28]. The first part of this section will discuss the properties of defect-free photonic crystals in different dimensionalities, which is followed by a brief overview of defect cavities in these systems. The third subsection is dedicated to two-dimensional photonic crystal slabs, and an overview of different defect types in two-dimensional photonic crystal slabs is given in the fourth and last subsection.

2.3.1 Properties of defect-free photonic crystals

Photonic crystals are materials with a periodic variation of the refractive index. Analogously to the electronic band gap in the periodic atomic crystals of semiconductors, the periodicity of the refractive index in photonic crystals leads to the formation of a photonic band gap. This photonic band gap is characterised by the absence of any optical states for the corresponding photon energy range [26].

The most common type is the one-dimensional photonic crystal, which consists of alternating layers of two materials with different refractive indices, as illustrated in Fig. 2.4 a. Here, the refractive index varies in a periodic manner with a lattice constant a in one spatial direction, but is constant in the two other directions. Due to the discrete translational symmetry of the system in the direction of periodicity, the wave vector k corresponding to this spatial direction can be restricted to the one-dimensional Brillouin zone, i.e. $-\frac{\pi}{a} < k \leq \frac{\pi}{a}$. The photonic band gap forms at the edge of the Brillouin zone, where $k = \pm \frac{\pi}{a}$ and the corresponding

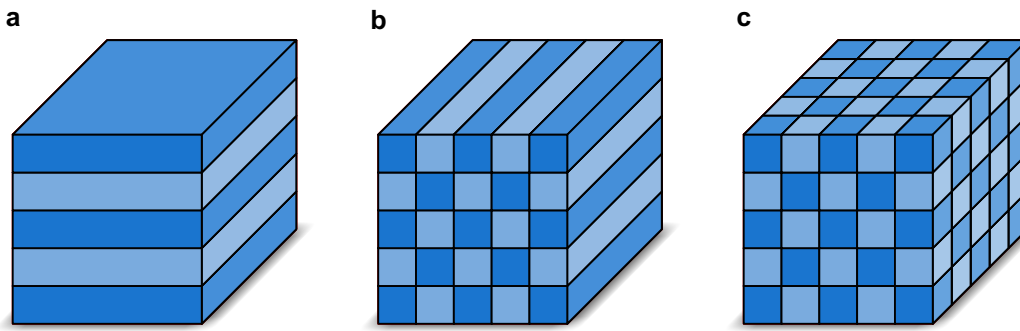


Figure 2.4 | Schematic illustration of photonic crystal structures. The different colours represent materials with different refractive indices. **a**, One-dimensional photonic crystal (also known as distributed Bragg reflector). **b**, Two-dimensional photonic crystal. **c**, Three-dimensional photonic crystal.

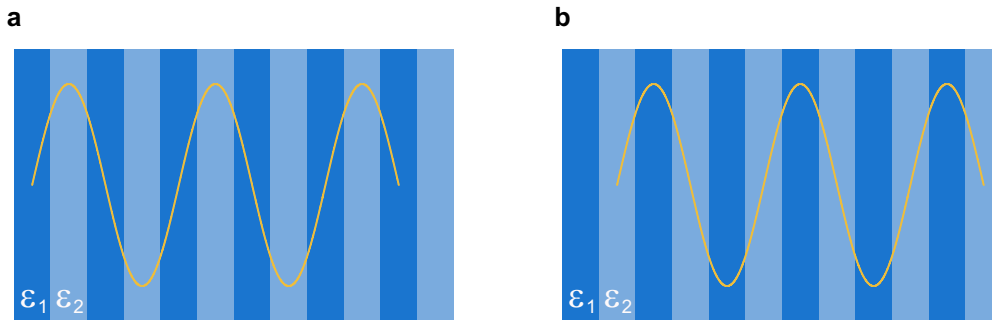


Figure 2.5 | Illustration of the origin of photonic band gaps. The different colours represent materials with different refractive indices $\epsilon_1 < \epsilon_2$. **a**, Electric field with the energy concentrated in the higher-index region. **b**, Electric field with the energy concentrated in the lower-index region.

modes hence have a wavelength of $2a$. There are two possibilities for such a mode to form in line with the symmetry of the material system, which are illustrated in Fig. 2.5. The electric field maxima are either centred in the high-index region (Fig. 2.5 a), or in the low-index region of the alternating layers (Fig. 2.5 b). This configuration at the edge of the Brillouin zone leads to two different modes that are separated by the photonic band gap: a low-frequency mode with a concentration of the electric energy density in the high-index regions, and a high-frequency mode with a concentration of the electric energy density in the low-index regions of the one-dimensional photonic crystal. As a result of the absence of extended optical states within this photonic band gap, electromagnetic radiation that is incident on a one-dimensional photonic crystal in the direction of periodicity decays exponentially into the crystal, and the radiation is reflected off the crystal [95]. From a theoretical point of view, the

behaviour of light in photonic crystals, and the formation of photonic band gaps, is governed by Maxwell's equations. A brief outline of the corresponding derivation of optical modes in a periodic dielectric medium is presented in Section 3.1.

One-dimensional photonic crystals, which are much better known as distributed Bragg reflectors, are compatible with mature coating and semiconductor growth techniques and have been used at least since the 1970s [96]. A cross-sectional transmission electron micrograph of a semiconductor Bragg reflector is shown in Fig. 2.6 a.

While one-dimensional photonic crystals were already studied theoretically by Lord Rayleigh in 1887 [97], the extension of this concept to two and three dimensions was remarkably suggested only a full century later [98, 99]. In two-dimensional photonic crystals, the refractive index varies periodically along two directions in a plane, while it remains constant in the direction perpendicular to this plane (Fig. 2.4 b). Consequently, the photonic band gap in such a system forms for light propagating in the plane of varying refractive index. Such a structure can be fabricated, for instance, by etching a periodic array of holes into a bulk material, as shown in a top view scanning electron micrograph in Fig. 2.6 b. The periodically varying refractive index is then provided by the contrast in refractive index between the vacuum-filled holes and the bulk material.

Ultimately, in a three-dimensional photonic crystal, the refractive index varies periodically in all three spatial directions, as illustrated in Fig. 2.4 c. This leads to the formation of a full, three-dimensional photonic band gap. The fabrication of such structures is technically challenging and was first demonstrated for dimensions on the micron-scale by the careful arrangement of polycrystalline silicon rods in a woodpile configuration in 1998 [100], as shown in Fig. 2.6 c.

While the analogy to semiconductor crystals is helpful for understanding the formation of photonic band gaps in photonic crystals, there is a fundamental difference in that in semiconductor crystals, the lattice constant and hence the characteristics of the band gap are given by the material that is used. In contrast, the properties of photonic crystals can be designed and tailored as required. In particular, the position of the photonic band gap (in frequency space) and its width scale linearly with the dimensions of the photonic crystal [95], and are limited towards higher frequencies only by the technical challenges in fabricating smaller photonic crystal structures accurately.

Both the perfectly reflective properties of photonic crystals in up to three dimensions and the possibility to tailor these properties to the requirements of the application make photonic crystals very interesting materials for the guiding of light on a chip, and for the formation of optical cavities, which will be discussed in the following section.

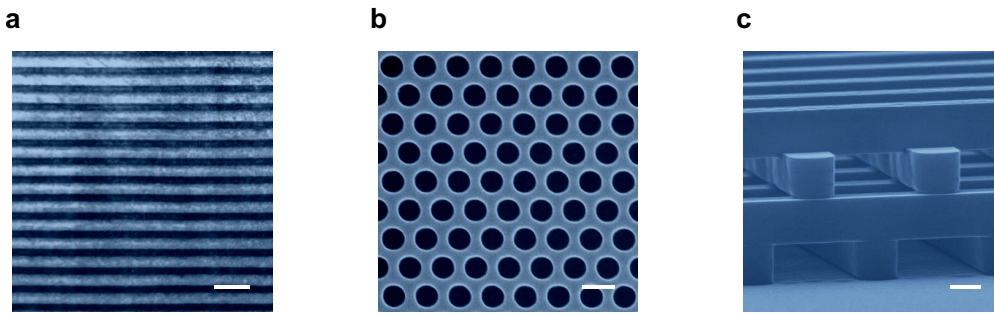


Figure 2.6 | Experimental realisations of photonic crystals in different dimensionalities. **a**, Cross-sectional transmission electron micrograph of a one-dimensional photonic crystal (Bragg reflector) [101]. The scale bar corresponds to 200 nm. **b**, Top view of a two-dimensional photonic crystal, fabricated by etching holes into gallium arsenide. The scale bar corresponds to 300 nm. **c**, Three-dimensional photonic crystal made of polycrystalline silicon [100]. The scale bar corresponds to 1 μm .

2.3.2 Microcavities in photonic crystal systems

The photonic band gap of photonic crystals and the resulting reflectivity of these structures that was discussed in the previous subsection make them ideal for strong confinement of light in high- Q cavities by the introduction of defects in an otherwise regular photonic crystal. Moreover, the dimensions of photonic crystals are by its very nature on the order of a wavelength of light, so that they also allow for the design of cavities with an extremely small mode volume V_m . These properties combined with the possibility to tailor them by careful design makes photonic crystal cavities very promising candidates for the cavity quantum electrodynamic effects that are crucial for the generation of indistinguishable single photons.

Cavities based on photonic crystals typically confine light in one or more spatial directions by the effect of the photonic band gap, and in the remaining spatial directions by total internal reflection at a dielectric–vacuum interface. The widely used micropillar cavity shown in Fig. 2.7 a is an example of a defect cavity in a one-dimensional photonic crystal in which light is confined vertically by the photonic band gap, and laterally by total internal reflection at the semiconductor–vacuum interface. Q -factors of up to 160 000 have been reported for such micropillars in gallium arsenide [105], and the mode volume is typically on the order of five cubic wavelengths [25].

Another variation of one-dimensional light confinement by a photonic crystal and two-dimensional confinement by index guiding is shown in Fig. 2.7 b. A strip waveguide fabricated from a silicon-on-insulator substrate is patterned with a one-dimensional periodic array of holes, and the cavity is formed by the omission of one hole along this line [57]. Light in this cavity is confined to the waveguide by total internal reflection, and along the waveguide-

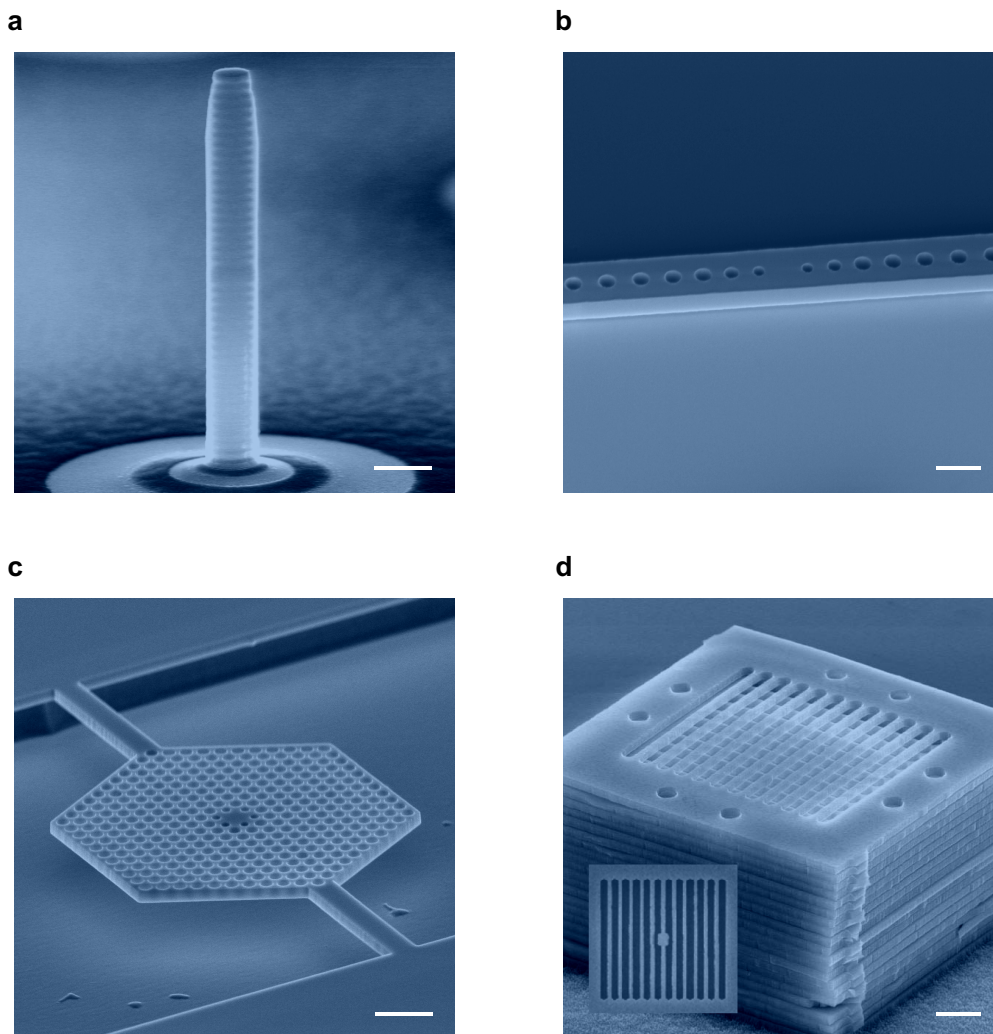


Figure 2.7 | Defect cavities in photonic crystals of different dimensionalities. **a**, GaAs/AlGaAs micropillar with a defect cavity in a one-dimensional photonic crystal (Bragg mirror) [73]. The scale bar corresponds to $1\ \mu\text{m}$. **b**, Silicon on insulator ridge waveguide with a tapered one-dimensional photonic crystal defect cavity [102]. The scale bar corresponds to $0.5\ \mu\text{m}$. **c**, H1 defect cavity in a two-dimensional photonic crystal patterned in a suspended gallium arsenide slab. The scale bar corresponds to $1\ \mu\text{m}$. **d**, Three-dimensional gallium arsenide photonic crystal fabricated by micromanipulation [103]. The defect cavity is created by including the layer shown in the inset at the centre of the stack [104]. The scale bar corresponds to $3\ \mu\text{m}$.

uide axis by the band gap of the one-dimensional photonic crystal. Q -factors of up to 58 000 and simultaneously small mode volumes of 0.6 cubic wavelengths have been reported with this design in silicon [102]. In contrast to the micropillar cavity, this waveguide-based design is also inherently integrable with planar light circuits and is therefore an interesting system for on-chip single photon sources.

A more versatile platform, however, are defect cavities in suspended two-dimensional photonic crystal slabs, which typically consist of periodic arrays of holes in a thin semiconductor slab, as shown in Fig. 2.7 c. Here, light is confined in the slab plane by the band gap of the two-dimensional photonic crystal, and vertically by total internal reflection. For these systems, impressive Q -factors of up to 700 000 have been demonstrated in gallium arsenide [94] for passive cavities with a mode volume of about 1.5 cubic wavelengths [106]. Owing to their ability to couple to waveguides in the same structure, two-dimensional photonic crystals are also well suited for the realisation of integrable single photon sources. A more detailed discussion of this type of photonic crystals will therefore be provided in the next subsection.

Ultimately, photonic crystal microcavities can also be created by defects in three-dimensional photonic crystals, as shown in Fig. 2.7 d. In this type of cavities, light is confined in all spatial directions by the photonic band gap. Q -factors of up to 13 600 [107] and mode volumes of 0.4 cubic wavelengths [108] have been reported for such microcavities. While this material system is theoretically very attractive for the realisation of multilayer optical networks [109], the nanofabrication of these structures is very challenging [110].

After the discussion of defect cavities in photonic crystals of different dimensionalities in the previous paragraphs, the remainder of this section will be dedicated to the discussion of two-dimensional photonic crystal slabs, which were employed in this work.

2.3.3 Two-dimensional photonic crystal slabs

As discussed in the previous subsection, two-dimensional photonic crystal slabs are a versatile and attractive platform for the integration of photonic circuits. Therefore, the combination of these structures with semiconductor quantum dots is employed in this work to demonstrate integrable single photon sources. This subsection will first cover theoretical aspects that affect two-dimensional photonic crystal slabs in particular, and then discuss some practical design considerations.

Two-dimensional photonic crystal slabs typically consist of a thin semiconductor slab that is patterned with an array of holes. This concept was first demonstrated experimentally at optical wavelengths in 1996 [111]. Since the patterned slab, combined with the vacuum cladding on both sides, exhibits a mirror symmetry with respect to the centre of the slab, the optical modes in the slab can be classified by even or odd parity. Modes with an even parity have non-zero electric field components in the plane of the slab, and a non-zero magnetic field component vertical to the slab. Only these modes are of interest for the interaction with

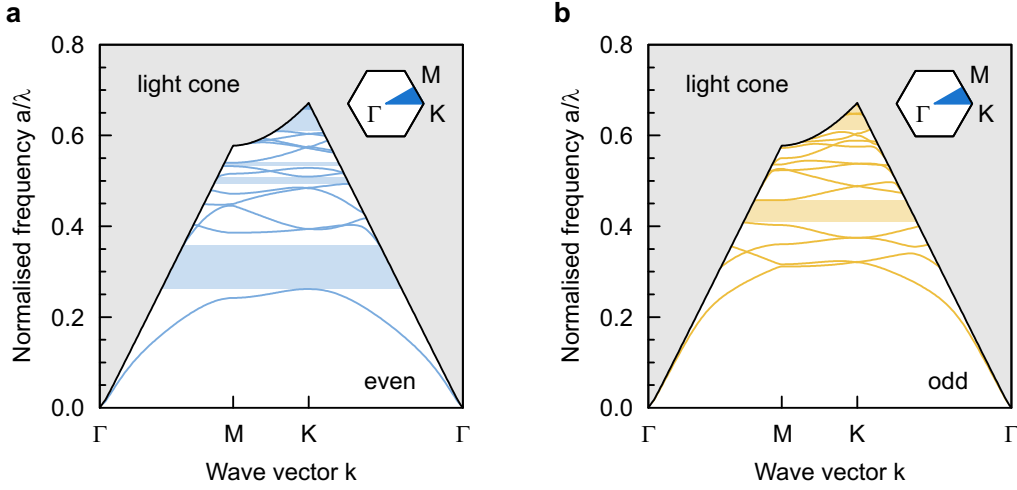


Figure 2.8 | Band diagrams for a two-dimensional photonic crystal slab. In the simulation, the slab thickness was $\frac{d}{a} = 0.7$, and the radius of the holes in a hexagonal lattice was $\frac{r}{a} = 0.36$. **a**, Band diagram for modes with an even parity with respect to the slab plane. **b**, Band diagram for modes with an odd parity.

quantum dots, as their transition dipoles are oriented in the plane of the slab [87]. The band diagrams for even and odd modes for a two-dimensional photonic crystal slab can have very different properties. As an example, Figs. 2.8 a and b show the band diagrams for even and odd modes, respectively, for a hexagonal lattice of circular holes in a gallium arsenide slab. The optical modes with even and odd parities are entirely different. Consequently, the resulting photonic band gaps, which are highlighted by the shaded areas, appear in different frequency ranges.

Another notable feature of these band diagrams is the appearance of a light cone, which is a result of the incomplete vertical confinement of light by total internal reflection and the resulting radiation loss from the slab into the vacuum cladding. In order to describe this leakage theoretically, it is instructive to consider first the extended modes in the vacuum cladding, which are superpositions of plane waves with the frequency ω and obey the dispersion relation

$$\omega = c_0 |\vec{k}| = \sqrt{\vec{k}_{\parallel}^2 + k_{\perp}^2}, \quad (2.16)$$

where c_0 is the speed of light, \vec{k}_{\parallel} is the projection of the wave vector into the slab plane (i.e. the dependent variable in the band diagrams in Fig. 2.8), and k_{\perp} is the vertical wave vector component. Since k_{\perp} can take any value, for a given \vec{k}_{\parallel} , there is a continuum of states in the vacuum cladding with $\omega \geq c_0 |\vec{k}_{\parallel}|$, which is called the light cone. On the contrary, the dispersion in a semiconductor slab can be written in a first approximation as

$$\omega = \frac{c_0}{n_{\text{slab}}} |\vec{k}|, \quad (2.17)$$

where n_{slab} is the refractive index of the slab material. Optical states in the slab will therefore leak into the vacuum cladding with \vec{k}_{\parallel} as a conserved quantity [95] provided that

$$c_0 \sqrt{\vec{k}_{\parallel}^2 + k_{\perp}^2} \leq \frac{c_0}{n_{\text{slab}}} \sqrt{\vec{k}_{\parallel}^2 + k_{\perp}^2}. \quad (2.18)$$

All other optical states, i.e. those below the light cone, are confined to the slab by total internal reflection. This statement is equivalent to Snell's law in geometric optics [95]. The incomplete confinement by total internal reflection effectively limits the range of vertically confined wave vectors, in particular for higher frequencies (see Fig. 2.8). The higher order band gaps are therefore of limited use for effective light confinement, and in this work, only the lowest-energy band gap is employed.

Since two-dimensional photonic crystals are artificial materials, there is a number of design parameter that can be chosen to suit the experimental needs. These parameters will be discussed in the remainder of this subsection.

The choice of the material system in this work is dictated by the excellent single photon emission properties of indium arsenide quantum dots in a gallium arsenide matrix. In the discussion of two-dimensional photonic crystal slabs, the material is considered as pure gallium arsenide, as the quantum dot layer comprises only a negligible amount of the total material. It is worth noting, however, that the photonic crystal structures studied in this work are by no means restricted to this material system. In fact, two-dimensional photonic crystal slabs have been studied in a wide range of materials, including silicon [112], indium phosphide [113], gallium nitride [114], silicon carbide [115], diamond [116], and lithium niobate [117].

The shape of the holes that pattern the slab to form a two-dimensional photonic crystal was chosen to be circular, as circles are most readily reproduced with lithographic techniques due to the absence of sharp angles. For the same reason, circular features are also the most widely studied, even though square, triangular, and hexagonal hole shapes have been considered theoretically [118]. A limited number of experimental studies have been performed on two-dimensional photonic crystal slabs with triangular [119] and hexagonal [120] feature shapes as well.

The circular holes in this work are arranged in a hexagonal lattice in order to form a photonic crystal, since this lattice has a small unit cell and offers a relatively wide band gap for even parity [95], both of which make this lattice very versatile. Alternative lattice configurations include the square lattice [121], which has attracted relatively little attention due to the small band gap [122]; the honeycomb lattice, which offers a relatively wide joint band gap for both even and odd parities [95]; and the kagome lattice [123]. A band gap map of a two-dimensional gallium arsenide photonic crystal slab with a hexagonal lattice of circular, vacuum-filled holes is shown in Fig. 2.9. The band gap position and width is shown as a function of hole radius (Fig. 2.9 a) and slab thickness (Fig. 2.9 b). Since the ideal hole radius

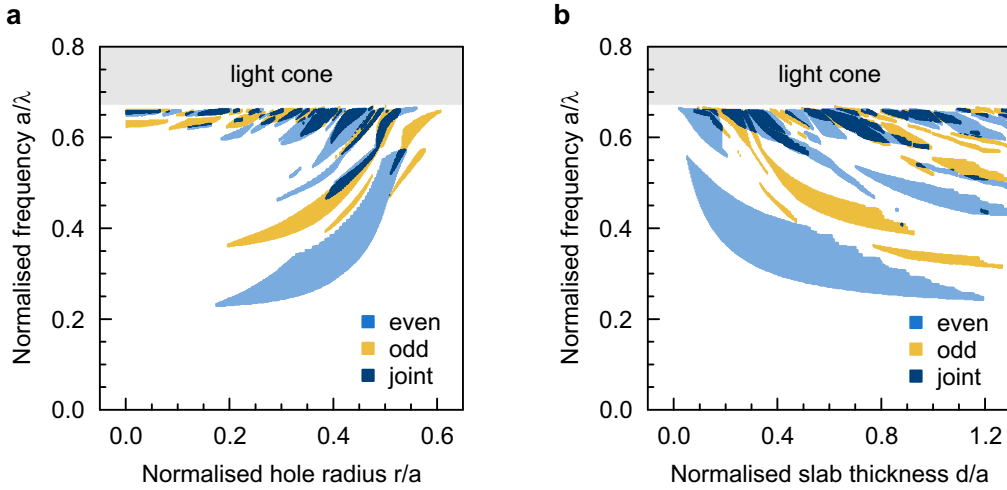


Figure 2.9 | Band gap maps of the hexagonal lattice in a photonic crystal slab. The photonic crystal consists of an array of circular, vacuum-filled holes ($n = 1.0$) in a gallium arsenide slab ($n = 3.5$). The grey areas indicate the regions in which the continuum of states above the light line exists for all k -vectors. **a**, Band gap map for varying normalized hole radius for a fixed normalized slab thickness $\frac{d}{a} = 0.7$. Please note that suspended photonic crystal slabs with vacuum-filled holes characterised by $\frac{r}{a} \geq 0.5$ are not feasible. **b**, Band gap map for varying normalized slab thickness for a fixed normalized hole radius $\frac{r}{a} = 0.36$.

and slab thickness depend on the particular photonic crystal structure under study, however, these parameters will be discussed separately in the corresponding chapters.

The two-dimensional photonic crystal slabs studied here have a vacuum cladding both above and below the slab, as this leads to more efficient confinement of light to the slab as compared to other, higher-index claddings [124]. The vacuum cladding below the slab is realised by the selective etching of a sacrificial layer, as described in Section 3.2. The thickness of the sacrificial layer therefore determines the thickness of the lower vacuum cladding, or equivalently the distance between the slab and the substrate. In order to avoid undesired optical losses from the slab, a vacuum cladding thickness equivalent to the free space wavelength was found to be sufficient [125]. This was confirmed independently with finite-difference time-domain simulations, and all photonic crystal slabs studied in this work have a bottom vacuum cladding of 900 nm thickness, which corresponds to the typical wavelength of photons emitted by the indium arsenide quantum dots studied here.

This concludes the discussion of bulk two-dimensional photonic crystal slabs. A selection of possible defects in these structures is presented in the following subsection.

2.3.4 Defects in two-dimensional photonic crystal slabs

Optical cavities can be created in two-dimensional photonic crystal slabs by the introduction of defects into an otherwise regular crystal lattice. These defects can be created by changing the properties of one or more holes in the lattice, including the modification of the refractive index [126], a change of the hole diameter [127, 128], or shifting the hole position [129]. For the coupling of semiconductor quantum dots to such a defect cavity, however, the simple omission of one or more holes is the most attractive defect type since this creates a sufficiently large slab material volume to contain the quantum dot.

Typical defects in hexagonal lattices are illustrated in Fig. 2.10. A widely studied point defect cavity is the H1 cavity, which is created by the omission of a single hole (Fig. 2.10 a). For H1 cavities in gallium arsenide, Q -factors of 17 000 have been reported and mode volumes of less than 0.4 cubic wavelengths were achieved [130]. A slightly larger point defect cavity is the L3 cavity, which is formed by the omission of three holes along a line (Fig. 2.10 b). It is one of the most popular types of microcavities [131]. Compared to the H1 cavity, modes in the L3 cavity typically exhibit slightly larger mode volumes on the order of 0.7 cubic wavelengths [79], as intuitively expected. However, considerably higher Q -factors of up to 30 000 [79] were achieved in gallium arsenide. For both the H1 and the L3 cavities, additional modifications to the position and the size of the holes adjacent to the defect are typically introduced in order to minimise leakage to the vacuum cladding and hence maximise the achievable Q -factors [112].

Alternatively, the formation of a line defect by the omission of an entire row of holes leads to the formation of a W1 photonic crystal waveguide, as illustrated in Fig. 2.10 c. Photonic crystal waveguides are attractive for the miniaturisation of planar light circuits, as they can provide sharp bends with low radiation losses [132]. Moreover, they can easily be interfaced with more traditional waveguides [133–135]. While photonic crystal waveguides are not optical cavities in the traditional sense of light confinement in all three spatial directions, slow-light effects [136–138] at the edge of the Brillouin zone can still be exploited for cavity quantum electrodynamic effects, as is demonstrated in Chapter 4.

Additional, local modifications of the photonic crystal lattice adjacent to the waveguide allow for the design of optical cavities in the traditional sense. As an example for this concept, Fig. 2.10 d shows such a waveguide-based double-heterostructure cavity. It is obtained by a slight modification of the lateral lattice constant for a few periods along the waveguide. Different photonic band gaps in the areas with a different lateral lattice constant lead to a localised confinement of light in the area with the larger lateral lattice constant. The confinement mechanism along the waveguide is therefore analogous to the confinement of electrons in a quantum dot. In gallium arsenide photonic crystal slabs, such double-heterostructure cavities have been demonstrated with Q -factors up to 250 000 [139], about one order of magnitude larger than for other photonic crystal-based cavities. The mode volume for this type of

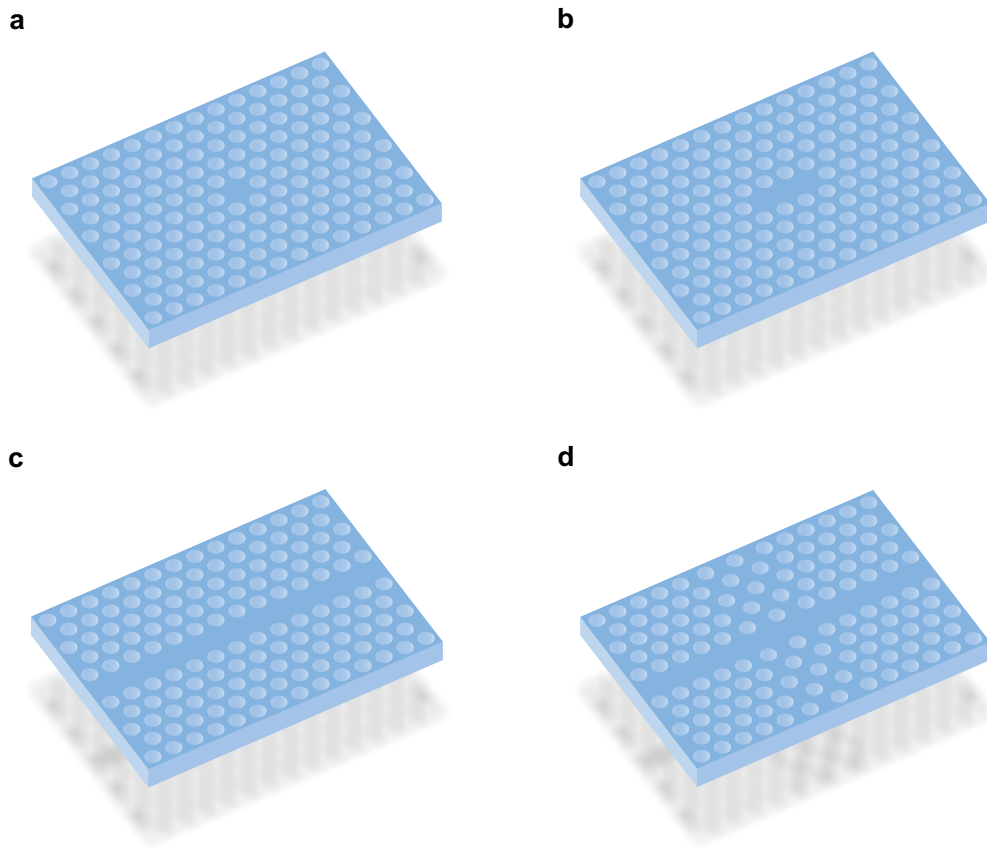


Figure 2.10 | Illustration of cavities in two-dimensional photonic crystal slabs. a, H1 cavity created by the omission of one hole. **b,** L3 cavity, which is obtained by the omission of three holes along a line. **c,** A W1 waveguide is formed by the omission of an entire line of holes. **d,** Heterostructure waveguide cavity, created by a change of the lateral period for a lattice constants along the waveguide.

cavities is approximately 1.2 cubic wavelengths [140]. In a similar approach, the width of the photonic crystal waveguide is modified locally, leading to the experimental demonstration of a record Q -factor of 700 000 in a gallium arsenide slab, with a mode volume of 1.5 cubic wavelengths [106]. It must be noted, however, that this was demonstrated for a pure gallium arsenide slab, and similar experiments with a layer of quantum dots embedded at the centre of the slab reached only much more modest Q -factors of about 13 000, which was attributed to material absorption introduced by the quantum dot layer [141].

In summary, this chapter introduced and discussed the three theoretical concepts that are central to the demonstration of on-chip single photon sources in this work. The electronic properties of indium arsenide quantum dots and their resulting suitability as efficient sources of single photons were presented first. The importance of cavity quantum electrodynamic

effects for the demonstration of efficient sources of indistinguishable photons was discussed next, and photonic crystal cavities in general and two-dimensional photonic crystal slabs in particular were identified as a promising platform for the integration of single photon sources with quantum photonic circuits. The following chapter provides a discussion of the methods that were employed in order to exploit the theoretical concepts presented in this chapter.

3 Methods

This chapter introduces the methods and techniques used for the demonstration of integrable on-chip single photon sources based on quantum dots in photonic crystal structures described in the following chapters. The simulation tools used to study and optimise device concepts are described in the first section of this chapter, while the second section is dedicated to the experimental methods employed to fabricate real devices. Finally, the techniques used for the optical characterisation of the devices are described the third section.

3.1 Simulation tools

The device concepts discussed in the following chapters were first studied with simulation tools in order to optimise the design parameters of the devices. Experimental results were then compared to theoretical predictions by simulating the particular devices under study in order to confirm the interpretation of the observed behaviour. For these purposes, the finite-difference time-domain and the plane wave expansion techniques were used, which are described in this section. For both techniques, a model of the device structure was created with a graphical CAD software interface. The refractive indices at $\lambda = 900$ nm and $T = 5$ K used here were 1.0 for vacuum for the holes and the cladding above and below the slab, and 3.5 for gallium arsenide [142] as the slab material. Only modes with an even parity with respect to the slab plane were considered, since quantum dots can only couple to this type of modes because their main transition dipoles are directed in the slab plane [87].

3.1.1 Finite-difference time-domain simulations

The finite-difference time-domain technique [143] is used to calculate mode structures, resonant frequencies, Q -factors, mode profiles and mode volumes. The technique provides a rigorous solution of the time-dependent Maxwell's equations, which, in the absence of currents ($\vec{j} = 0$), relate the temporal evolution of the electric field \vec{E} to the spatial distribution of the magnetic field \vec{H} , and vice versa, by

$$\vec{\nabla} \times \vec{E} = -\mu_0 \frac{\partial \vec{H}}{\partial t} \quad (3.1)$$

$$\vec{\nabla} \times \vec{H} = \epsilon_0 \epsilon(\vec{x}) \frac{\partial \vec{E}}{\partial t}, \quad (3.2)$$

where μ_0 is the magnetic vacuum permeability, ϵ_0 is the electric vacuum permeability, $\epsilon(\vec{x})$ is the spatial distribution of the refractive index, and t is time. By discretising both time and space, the temporal evolution of the electric and magnetic fields can be calculated efficiently using only addition, subtraction and multiplication. The commercial implementation used here (Fullwave, RSoft) employs Yee's mesh [144], in which space is discretised into a Cartesian grid and field components are staggered in such a way that electric field components are half way between magnetic field components, and vice versa. The field components are calculated for the resulting grid points in a leapfrog manner, alternating between the electric and magnetic field components for subsequent time steps.

In order to obtain accurate results while at the same time minimising simulation times, the spatial and temporal grid size need to be chosen carefully. For the simulations presented in the following chapters, convergence studies were performed, confirming that the obtained results converge for a spatial grid size of $\frac{1}{16}$ of the photonic crystal periodicity in the slab plane and $\frac{1}{16}$ of the slab thickness perpendicular to this plane. An appropriately small time step size for convergent simulations can be deduced from the spatial grid size via the Courant condition [145].

With regard to the temporal domain size, simulations for the devices studied here were found to converge for 2^{16} time steps, while the spatial domain size was chosen such that it comprised the entire device structure to be simulated, including a vacuum cladding above and below the slab with a thickness of at least twice the slab thickness. The spatial domain was typically bound by a perfectly matched layer [146], which absorbs impinging electromagnetic waves without reflections. Convergence studies confirmed that a perfectly matched layer thickness of ten grid points provided accurate results.

In order to calculate mode structures, which show photonic band gap edges and the frequencies at which the structures exhibit resonances, the cavity is excited in a first attempt with a number of randomly positioned and polarised impulse sources with a δ -function-like temporal evolution which excite across a broad band of frequencies. The field then decays over time without further driving, and the time response of the system is monitored at different positions. The corresponding spectra are calculated from these time responses with a discrete Fourier transform. An estimate of the spectral position of the photonic band gap can be extracted from these simulations by placing monitors outside the device, where they are separated from the sources in the cavity by typically ten periods of the two-dimensional photonic crystal. The recorded field amplitudes at these positions are strongly suppressed at frequencies within the photonic band gap due to the lack of optical states in the photonic crystal. In contrast, resonances were identified by placing randomly positioned field monitors inside the cavity. The frequency-analysed signal reveals narrow intensity peaks at the resonant frequencies of the structure.

In order to calculate resonant frequencies more precisely and extract accurate Q -factors

from these simulations, a very high frequency resolution is required. According to the time-frequency uncertainty of the discrete Fourier transform, a higher frequency resolution can be obtained for longer time series. However, for the accurate calculation even of moderate Q -factors, this requires prohibitively long simulation times [147]. Exploiting the knowledge about the nature of the signals, the recorded temporal evolution of the field is therefore approximated by advanced harmonic analysis as the sum of complex exponentials,

$$f(t) = \sum_n c_n e^{-i\nu_n t}, \quad (3.3)$$

where the complex frequency $\nu_n = \omega_n + i\gamma_n$ comprises the oscillatory frequency ω_n and the loss rate γ_n , which is directly related to the Q -factor. This approach reduces the problem to a fit of the parameters c_n and ν_n . By focussing on narrow frequency bands of interest, this technique allows to extract accurate values for the resonant frequency and the Q -factor with relatively short simulation times [148].

Once precise resonant frequencies were identified, mode profiles were calculated by exciting the structure with a spectrally narrow continuous-wave source emitting at the resonant frequency. The field distributions of the E_x , E_y , and H_z components were recorded with spatial monitors at the end of the simulations, when a steady state has been obtained. Recording the field distributions part way through an optical cycle allows to extract both electric and magnetic field components from a single simulation.

Finally, mode volumes were calculated according to Eqn. 2.5 from the electric energy density distribution of a mode across the computational domain. For consistency, the mode volume is evaluated at the point of the optical cycle when the electric energy density is maximal.

In an iterative process, the knowledge of the mode profiles was used to optimise the position of excitation sources and field monitors in order to obtain balanced mode profiles; more accurate calculations of resonant frequencies and Q -factors; and mode profiles that are virtually free of distortions introduced by the excitation sources. Moreover, the symmetries of the mode profiles were exploited in order to reduce simulation times by reducing the size of the computational domain and introducing symmetric or anti-symmetric boundary conditions as applicable. This led to a significant reduction of simulation times, in particular for the parameter scans in the design optimisation.

3.1.2 Plane wave expansion simulations

For point defect cavities in photonic crystal structures, the finite-difference time-domain technique described in the previous section is sufficient to study all the properties of interest. Since the following chapters are concerned with the integrability of single photon sources, however, photonic crystal waveguides feature prominently in all chapters. For these structures, dispersion relations and full band structures are of paramount interest as they are

essential to understand the properties of the guided modes in the waveguide. In contrast to the finite-difference time-domain simulations, band structures were calculated in the frequency domain with the plane wave expansion technique. This method equally relies on the time-dependent Maxwell's equations given in Eqns. 3.1 and 3.2. Since these equations are linear, their solutions can be separated into spatially and temporally dependent parts as

$$\vec{E}(\vec{x}, t) = \vec{E}(\vec{x}) e^{-i\omega t} \quad (3.4)$$

$$\vec{H}(\vec{x}, t) = \vec{H}(\vec{x}) e^{-i\omega t}. \quad (3.5)$$

Combining equations 3.1, 3.2, 3.4, and 3.5, the vector Helmholtz equation is obtained as [26]

$$\vec{\nabla} \times \frac{1}{\varepsilon(\vec{x})} \vec{\nabla} \times \vec{H}(\vec{x}) = \left(\frac{\omega}{c}\right)^2 \vec{H}(\vec{x}), \quad (3.6)$$

where $c = 1/\sqrt{\mu_0\varepsilon_0}$ is the speed of light. Since this equation, when applied to photonic crystal structures, represents a linear eigenvalue problem in a periodic system, the eigenstates can be chosen according to Bloch's theorem as

$$\vec{H}(\vec{x}) = e^{i\vec{k}\cdot\vec{x}} \vec{H}_{\vec{k}}(\vec{x}), \quad (3.7)$$

where \vec{k} is the wave vector and $\vec{H}_{\vec{k}}(\vec{x})$ is a field with the periodicity of the lattice. The vector Helmholtz equation then becomes a linear eigenvalue problem in the unit cell with

$$\underbrace{\left(\vec{\nabla} + i\vec{k}\right) \times \frac{1}{\varepsilon(\vec{x})} \left(\vec{\nabla} + i\vec{k}\right) \times}_{\hat{A}_{\vec{k}}} \vec{H}_{\vec{k}}(\vec{x}) = \left(\frac{\omega}{c}\right)^2 \vec{H}_{\vec{k}}(\vec{x}). \quad (3.8)$$

Since $\hat{A}_{\vec{k}}$ is a Hermitian operator and has a compact support, the solutions are a discrete sequence of real eigenvalues $\omega_n(\vec{k})$ that form the band structure [149]. This eigenvalue problem is solved numerically with a commercial software (Bandsolve, RSoft) by expanding the unknown eigenstates $H_{\vec{k}}(\vec{x})$ in a truncated Fourier series of plane waves (hence the name plane wave expansion technique).

Since the band diagram is calculated for an infinite structure by applying periodic boundary conditions to all boundaries of the computational domain, an appropriate computational domain has to be chosen to calculate band structures: while for the band diagram of a bulk photonic crystal a single unit cell is sufficient, defects require significantly larger computational domain to ensure dispersions are not unintentionally affected by these periodic boundary conditions.

3.2 Device fabrication

This section describes the experimental techniques employed to fabricate self-assembled indium arsenide quantum dots and photonic crystal slabs. It is divided into two subsections, the first of which is dedicated to the sample growth with molecular beam epitaxy, and the second to the processing steps for the device fabrication.

3.2.1 Sample growth with molecular beam epitaxy

The growth of slab structures with embedded self-assembled quantum dots requires the ability to deposit thin films of high-quality semiconductors with abrupt changes in the material composition and excellent control over growth conditions. Molecular beam epitaxy, and some other advanced epitaxial techniques such as metal-organic vapour phase epitaxy, meet these criteria [40]. The former is employed to grow the samples that were used to demonstrate on-chip single photon emission in the following chapters.

Molecular beam epitaxy is the growth of compound semiconductor films through the reaction of one or more thermal molecular beams with a crystalline surface [150]. A simplified schematic of a typical growth chamber for this technique is shown in Fig. 3.1 a. The chamber is kept at ultra-high vacuum, at a base pressure of about 10^{-10} mbar in the system used here, and includes a set of effusion cells containing the required elements, such as gallium, arsenic, aluminium and indium. The temperature of each effusion cell, and with it the molecular flux emanating from it, can be controlled independently, and the molecular beams can be intercepted by externally controlled shutters [150]. The beams are directed at a pre-cleaned, epi-ready (100) gallium arsenide substrate that is maintained at elevated temperatures of 470 – 580 °C. The substrate is rotated during growth in order to compensate for the flux variation across the substrate due to the geometrical arrangement of the sources. Growth rates are relatively low (on the order of $1 \frac{\mu\text{m}}{\text{h}}$), and the growth progress is monitored in-situ using reflection high-energy electron diffraction [151]. Additional diagnostic tools, such as a mass spectrometer and a beam flux gauge, are used to monitor growth conditions.

In a typical layer sequence for photonic crystal slabs, a 250 nm gallium arsenide buffer is grown first in order to smooth out surface roughness and recover good crystallinity [152]. This is followed by a 900 nm thick sacrificial layer of aluminium gallium arsenide with an aluminium composition of 75%, and then the lower half of the gallium arsenide slab with a typical thickness of 100 nm. Since these two materials are lattice-matched to about 0.1% ($a = 5.653 \text{ \AA}$ for GaAs and $a = 5.659 \text{ \AA}$ for $\text{Al}_{0.75}\text{Ga}_{0.25}\text{As}$ at $T = 300 \text{ K}$ [42]), they can be grown in sequence in nearly strain-free layers, with smooth interfaces [153], and virtually without thickness limitations [154]. The corresponding two-dimensional layer-by-layer growth is called the Frank-van der Merwe growth mode [155, 156], one of three possible heteroepitaxial growth modes [157, 158].

In order to embed a layer of quantum dots at the centre of the slab, indium arsenide is then grown on top of the first half of the gallium arsenide slab. Heteroepitaxial growth of this material combination results in the Stranski-Krastanow growth mode [34, 159], and its natural growth progression is illustrated in Fig. 3.1 c. The deposited indium arsenide first forms a wetting layer of about one monolayer thickness. In contrast to the heterointerfaces discussed in the previous paragraph, however, there is a substantial lattice mismatch of about 7% between the gallium arsenide substrate and the indium arsenide film ($a = 6.058 \text{ \AA}$ for InAs

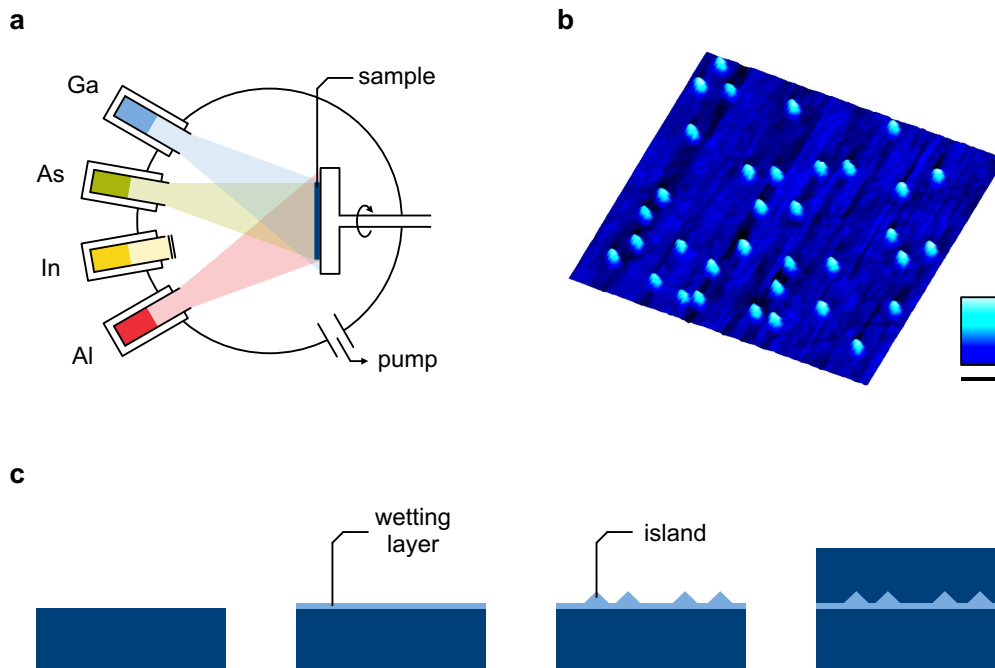


Figure 3.1 | Molecular beam epitaxy of self-assembled quantum dots. **a**, Simplified schematic of a growth chamber for molecular beam epitaxy. **b**, Atomic force micrograph of a high density of self-assembled nano-islands. The scale bar corresponds to 100 nm, the colour bar range to a height of 22 nm. **c**, Schematic of the natural growth progression (from left to right) of indium arsenide (light blue) on (100) gallium arsenide (dark blue) leading to the formation of quantum dots.

at $T = 300$ K [42]). Therefore, the indium arsenide layer is in compression to accommodate the lattice constant of the substrate. At a critical indium arsenide layer thickness of about 1.5 monolayers, there is a phase transition from two to three-dimensional growth [160] as it is energetically favourable for the indium arsenide film to form randomly positioned nano-islands, thus partly releasing the built-up strain. This relaxation mechanism leads to three-dimensional coherently strained, defect- and dislocation-free [43, 161] indium arsenide nano-islands. On further deposition of indium arsenide, the formed islands increase in size, and neighbouring islands start to coalesce, allowing for a degree of control over the size of the islands. Figure 3.1 b shows an atomic force micrograph of randomly positioned indium arsenide nano-islands on a gallium arsenide substrate.

Finally, the indium arsenide nano-islands are capped with another layer of typically 100 nm of gallium arsenide to complete the slab. In this process, the crystallinity of the overgrown gallium arsenide improves gradually starting at the indium arsenide interface [33]. The overgrowth also leads to a complete encapsulation of the indium arsenide islands in gallium arsenide, which provides the three-dimensional confinement of excitonic states in the resulting

quantum dots. Moderate substrate temperatures during overgrowth ensure that the excellent structural properties of the indium arsenide nano-islands are maintained [162]. The resulting quantum dots have a typical diameter of 20-30 nm and a height of 6-8 nm [160], and are composed of about 100 000 individual atoms [163].

Exploiting the easy cleaving mechanisms offered by (100) gallium arsenide [164], the completed wafer is then divided into dies of typically $6 \times 6 \text{ mm}^2$ size for the subsequent processing of photonic crystal structures described in the following subsection.

3.2.2 Fabrication of photonic crystal slabs

The complete sequence of processing steps required to fabricate two-dimensional photonic crystal slab structures is described in this subsection. Figure 3.2 gives an overview of the processing steps, which include electron-beam lithography, reactive ion etching and selective wet etching. The subfigures will be referred to at the appropriate paragraphs of the following description of the processing.

Electron beam lithography

The mask required to pattern the sample with a photonic crystal structure is defined lithographically. For photonic crystals with the fundamental band gap around 900 nm, the lattice constant is typically on the order of 200–300 nm, with feature sizes below 100 nm. The diffraction limit renders optical lithography unsuitable for patterns of these dimensions, as even state-of-the-art deep ultraviolet lithography is limited to patterning photonic crystals with lattice constants above 400 nm [165]. Therefore, electron beam lithography is employed for the definition of the mask. In this technique, electrons with a high kinetic energy are used to expose the resist. In the Leica VB6-UHR electron beam lithography tool used here, electrons are extracted from a tungsten tip by field emission and accelerated in an electric field to kinetic energies of 100 keV. The resulting electron beam is focussed and deflected by electron optics in order to write the required pattern into the resist layer.

ZEP 520 A (Zeon) is used as the electron beam resist. It allows for feature sizes down to 10 nm [166], which is comparable to the standard electron beam resist polymethyl methacrylate (PMMA) [167]. However, ZEP 520 A exhibits a substantially higher dry etch resistivity than PMMA [168, 169], resulting in a selectivity of the ZEP 520 A mask to gallium arsenide of 1 to 7 for an etching mechanism similar to the one used here [170]. A layer of approximately 280 nm of ZEP 520 A is spun directly onto the substrate (see Fig. 3.2 a). A thin anti-charging layer of highly conductive ESPACER 300Z (Showa Denko) is spin-coated on top of the ZEP 520 A in order to avoid beam deviation due to a built-up of charge on the resist layer surface during the writing process.

ZEP 520 A is positive-tone resist consisting of copolymers of α -chloromethacrylate and α -methylstyrene [171]. Irradiation by electrons leads to chain scission that breaks polymer

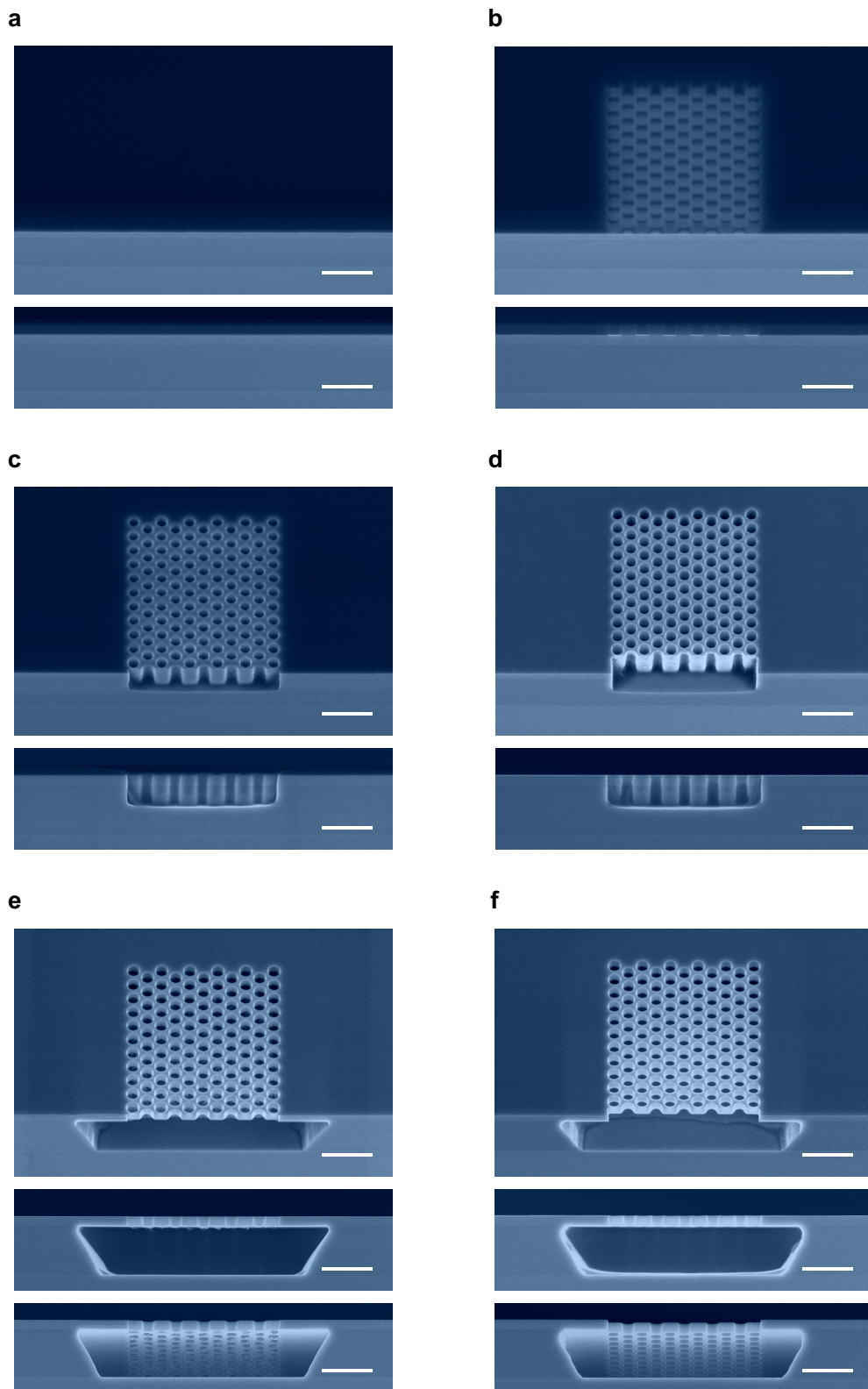


Figure 3.2 | Illustration of the process flow for the fabrication of photonic crystal slabs.
The scale bars correspond to 1 μm . For a detailed description, see main text.

bonds and effectively reduces the molecular weight of the resist in the exposed region [172]. After the completion of the exposure, the anti-charging layer is removed. Subsequent development of the resist in *n*-amyl acetate [173] leads to the selective removal of the exposed resist through aggregate removal [172] and yields the desired mask (see Fig. 3.2 b) for the following pattern transfer by reactive ion etching.

Inductively coupled plasma reactive ion etching

The photonic crystal pattern in the electron beam resist is subsequently transferred into the substrate by etching (see Fig. 3.2 c). This etching mechanism needs to be independent of the crystallographic orientation and provide a precise pattern transfer into the substrate. Furthermore, the etching should be highly anisotropic and result in straight, vertical side walls and the etched surfaces should be smooth and devoid of crystallographic damage. Finally, the etching selectivity between gallium arsenide and aluminium gallium arsenide should be negligible in order to be able to etch well into the sacrificial layer without damage to the pattern in the membrane.

These requirements can be met by inductively coupled plasma reactive ion etching (ICP-RIE), in which substrate material is removed by a combination of chemical reactions with suitable elements and the directional bombardment of the substrate with ions [174]. A typical reactor for this technique is shown in Fig. 3.3 a. It comprises a vacuum chamber with two internal electrodes (one of which is typically formed by the chamber walls) and an attached dielectric tube surrounded by an inductive coil. The process gas mix is fed into the chamber via the dielectric tube, and the application of a radio frequency electric field to the coil induces an axial alternating magnetic field. This in turn induces an electric field in the tube concentric to the coil, which leads to strong ionisation of the process gas and hence to the formation of a plasma [175]. The plasma density can be controlled by adjusting the radio frequency power supplied to the inductive coil [176]. Additionally, a second radio frequency field is applied to the internal electrodes and superimposed on the plasma. In this alternating electric field, electrons in the plasma are accelerated to higher velocities than ions due to their much lower mass. Therefore, electrons reach surfaces in contact with the plasma, such as the electrodes or a sample mounted on them, at much higher rates than ions. This leads to a negative self-biasing of these surfaces with respect to the plasma [174]. The directional acceleration of ions towards the sample resulting from this self-biasing is a crucial part of reactive ion etching, as will be discussed in the following paragraph. By adjusting the radio frequency power supplied to the internal electrodes, the self-biasing and hence the impact energy of the ions can be controlled [176].

For the process gas, a mixture of silicon tetrachloride and argon is a suitable choice in order to meet the etching requirements. In this mixture, chlorine is the chemical etching agent,

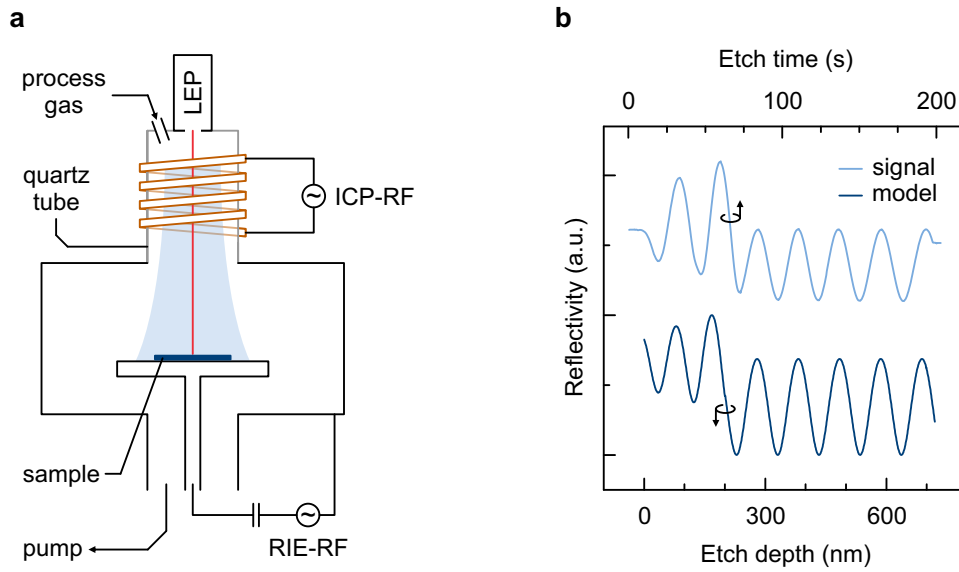
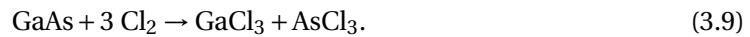


Figure 3.3 | Inductively coupled plasma reactive ion etching. **a**, Schematic of a typical reactor for this technique. The laser end point (LEP) technique is used for etch rate monitoring. **b**, Comparison of a typical measured signal and the modelled reflectivity for the in-situ etch rate monitoring by laser reflectometry.

which reacts with gallium arsenide on the substrate surface as [177]



This reaction is rate limited by the relative non-volatility of gallium trichloride, which accumulates on the surface and impedes the reaction of chlorine ions with the underlying gallium arsenide. However, through ion bombardment, gallium trichloride can be excited to a more volatile state, which increases the etch rate considerably [177]. In a pure chlorine plasma, the ion bombardment by impinging chlorine atoms is inefficient [175], which leads to rough surfaces due to micromasking [175, 178]. Therefore, argon is added to the process gas mix as it provides efficient ion bombardment [175, 178] and does not react chemically with the substrate materials [179].

While chemical etching is inherently isotropic [180], the ion-enhancement described in the previous paragraph provides a degree of anisotropy. The argon ions are accelerated by the self-bias and impinge on the sample normal to the surface. Therefore, they enhance the etching only at the bottom of any etched feature but do not affect the side walls [177]. In order to amplify this anisotropy of the etching, the process gas mixture comprises silicon tetrachloride rather than pure chlorine. The addition of silicon to the plasma results in the deposition of silicon dichloride radicals [180] and silicon dioxide [181] on the substrate surface. While this silicon-based layer is inert to chlorine chemistry [182], it is sputtered efficiently by argon ions from the bottom of etched features but not from side walls. This leads to a very effective

side wall passivation and to extremely vertical side walls [182]. Furthermore, decomposition products of silicon tetrachloride remove moisture and oxygen from the background atmosphere in the reactor, which reduces the etch selectivity between gallium arsenide and aluminium gallium arsenide due to aluminium oxidation [183]. This is of particular importance here as the reactor used for etching in this work is not equipped with a load lock.

The etch rate and depth are monitored in-situ using laser reflectometry [184]. In this technique, a laser beam is focussed onto an unmasked reference sample with an identical layer structure and the reflected signal is measured. The signal depends on the interference between partially reflected light at the interfaces between materials with different refractive indices, such as the plasma, gallium arsenide and aluminium gallium arsenide. During the etching, the reflectivity changes with the thickness of these layers, and by modelling these changes, the etch rate and depth can be inferred from the measured signal [185] (see Fig. 3.3 b).

Mask stripping

After exposure to the plasma of the reactive ion etching, the remaining ZEP 520 A mask layer is relatively hard and stripping therefore requires an aggressive mechanism. To this end, the polymers in the resist are first decomposed by flood exposure with ultraviolet radiation [186], and then dissolved in *n*-methyl-2-pyrrolidone (NMP) at an elevated temperature, resulting in a clean sample surface (see Fig. 3.2 d).

Selective under-etching with hydrofluoric acid

In order to form a two-dimensional gallium arsenide photonic crystal slab surrounded by a vacuum cladding on both sides, the aluminium gallium arsenide sacrificial layer is selectively removed by wet etching with hydrofluoric acid (see Fig. 3.2 e). The etching selectivity between aluminium gallium arsenide with an aluminium composition of 75% and gallium arsenide in hydrofluoric acid is about 2×10^5 [187]. For an under-etch of $1 - 2 \mu\text{m}$, which is required to remove the sacrificial layer underneath the photonic crystal structure completely, the gallium arsenide photonic crystal structure is therefore etched by less than 0.1 \AA , which is negligible in view of other fabrication imperfections.

A short dip in concentrated hydrofluoric acid is required first to remove an oxide layer that covers the exposed surfaces of the sacrificial layer. This is followed by the actual under-etching in a buffered hydrofluoric acid etching solution, which allows for a better control of the under-etching owing to a more moderate etch rate.

Side wall passivation layer removal

The lower panel in Fig. 3.2 e shows a bottom view of an under-etched photonic crystal slab. It can be seen that a thin membrane covers the walls of the holes and partly extends into the under-etched volume. This is attributed to remaining parts of the silicon-based side wall passivation layer formed during the dry etching of the holes. Since this represents a deviation from the ideal photonic crystal structure, it is expected that it has a detrimental effect on the performance of the photonic crystal devices. Therefore, the thin membrane is removed with a short plasma etch (Fig. 3.2 f).

Sample cleaving for in-plane optical access

The integrable in-plane single photon sources presented in the following chapters all (eventually) emit light into a photonic crystal waveguide for on-chip light guiding. In order to analyse the in-plane emission, these waveguides are terminated at one end by an etched facet, from which light is collected with a microscope objective. In order to allow for optical access to this facet, the sample is cleaved through a 10 μm wide etched rectangular feature adjacent to this facet. Precise rotational alignment of the devices to the crystallographic axes of the gallium arsenide substrate, the use of a precision scribe and the ease of cleaving (100) gallium arsenide [164] ensure a good yield in this step of the sample fabrication.

Quality control with scanning electron microscopy

After completion of the sample processing, a subset of the fabricated devices is imaged with a scanning electron microscope for quality control purposes. The resulting images are analysed using the ImageJ software package [188], yielding statistical information on the holes' diameter and its distribution across the device. The information gained by this image analysis is fed back into the design process, thus iteratively improving the structural properties of the photonic crystals. Deviations in the real device from the designed structure can occur due to the proximity effect during electron beam exposure [189], or process microloading in the resist layer development [189] or the reactive ion etching [190]. Structural parameters extracted from scanning electron micrographs in this way are also used to simulate the behaviour of experimentally characterised devices for comparison between theory and experiment.

3.3 Optical characterisation

After completion of the device fabrication described in the previous section, the samples were characterised optically using three different techniques, which are discussed in this section. These include micro-photoluminescence spectroscopy to study the emission spectrum of

devices; time-resolved photoluminescence spectroscopy to probe the temporal evolution of excitonic states in quantum dots; and Hanbury Brown and Twiss interferometry to gain information on photon statistics.

3.3.1 Micro-photoluminescence spectroscopy

Micro-photoluminescence spectroscopy is performed on the samples in order to study the emission spectrum of devices. It is useful to identify transitions in quantum dots and cavity modes, and to study their tuning behaviour, polarisation, and power dependence.

A schematic of the experimental setup for micro-photoluminescence spectroscopy is shown in Fig. 3.4. The sample is placed in an optical continuous-flow liquid helium cryostat with a base temperature of $T = 5$ K. Using an integrated heater, the sample temperature can be controlled in a range from $T = 5 - 300$ K. For good thermal contact, the sample is attached to the cold finger with conductive silver paint. Optical access to the sample is possible both in- and out-of-plane due to an extended cold finger and an appropriate corner window. The sample is excited optically above-band by using either a continuous-wave helium-neon gas laser [191] emitting at 632.8 nm [192], or a pulsed diode laser emitting pulses of a duration of 400 ps at a central wavelength of 785 nm with a repetition rate of 80 MHz. The laser emission is focussed from the top onto the sample using a vertically mounted microscope objective with a magnification of $\times 50$ and a numerical aperture of 0.4. The objective is attached to a three-axis translation stage to allow for the precise positioning and focussing of the laser spot on the sample. In order to facilitate the navigation on the sample, white light is coupled into the beam path with a beamsplitter, and its normal reflection off the sample is collected with the same objective and imaged with a camera.

In-plane emission is collected with a horizontally mounted, but otherwise identical microscope objective. The objective is likewise attached to a three-axis translation stage. A removable beamsplitter is inserted into the beam path and directs a part of the emission onto a second camera to facilitate the navigation along the edge of the sample. A long-pass filter removes any scattered laser emission, and the filtered emission is then coupled into a Czerny-Turner spectrometer [193] with a lens. In the spectrometer, the light is dispersed with a blazed grating and recorded with a charge-coupled device. Finally, a personal computer is employed to record the signal, which represents the detected light intensity as a function of the wavelength. A typical signal is shown in the previous chapter in Fig. 2.2 a.

For the experiments described in Chapters 5 and 6, the in-plane emission was first coupled into a multimode fibre and then filtered and coupled into the spectrometer with the same free-space arrangement of long-pass filter and lens. This improvement of the setup was introduced to simplify the alignment by maintaining the efficient coupling of the emission into the spectrometer when moving from one device to another. Since the microscope objective, the beamsplitter used for imaging and the fibre coupler were rigidly mounted in

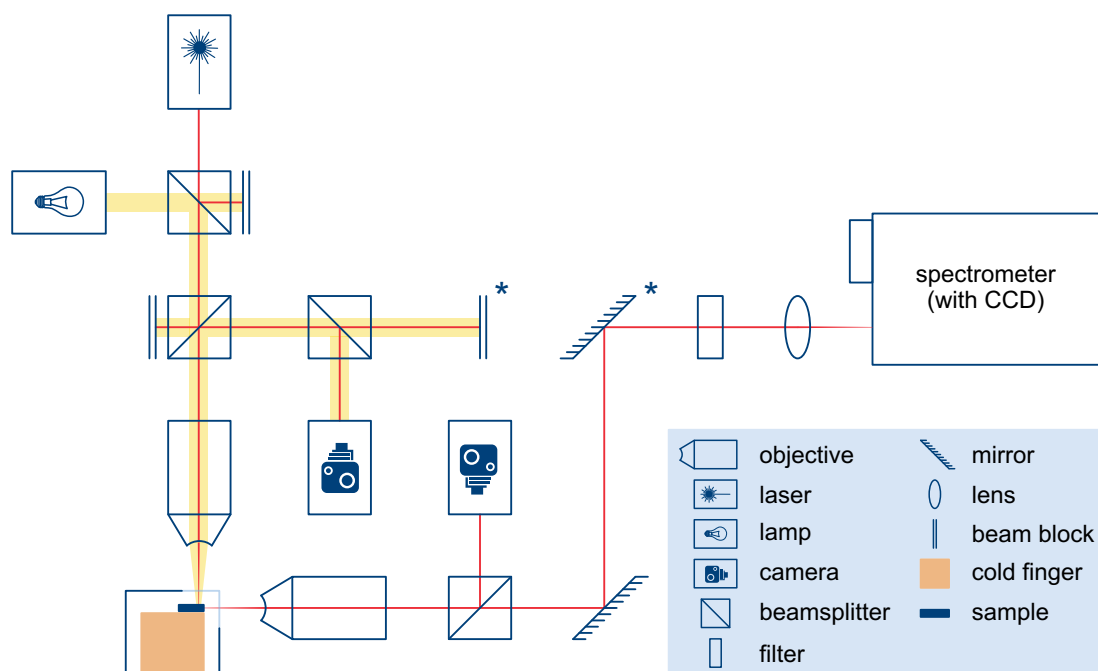


Figure 3.4 | Schematic of the setup for in-plane micro-photoluminescence measurements. For out-of-plane micro-photoluminescence measurements, the components marked with an asterisk could be removed.

a cage system, however, the beamsplitter was not removable any more in this arrangement. In order not to unnecessarily compromise the efficiency of the setup, a beamsplitter with a large transmission of 87% was chosen.

For the out-of-plane micro-photoluminescence measurements presented in Chapter 4, the in-plane emission was blocked, and the emission collected out-of-plane with the vertical objective was coupled into the spectrometer by removing the components marked with an asterisk in Fig. 3.4.

3.3.2 Time-resolved photoluminescence spectroscopy

Time-resolved photoluminescence spectroscopy was employed to study the temporal evolution of the carrier population of the quantum dot. To this end, the sample is excited with a pulsed laser, and the emission is collected and coupled into the spectrometer as described in the previous subsection. Here, the spectrometer is used as a monochromator by directing the dispersed light onto a narrow slit rather than onto a charge-coupled device. In this arrangement, only emission from the transition of interest is coupled out of the spectrometer, where it is then recorded with an avalanche photodiode operated in the Geiger mode [194] (see Fig. 3.5). The counts on the avalanche photo diode are recorded electronically as a function of the time delay with respect to the trigger signal from the pulsed laser.

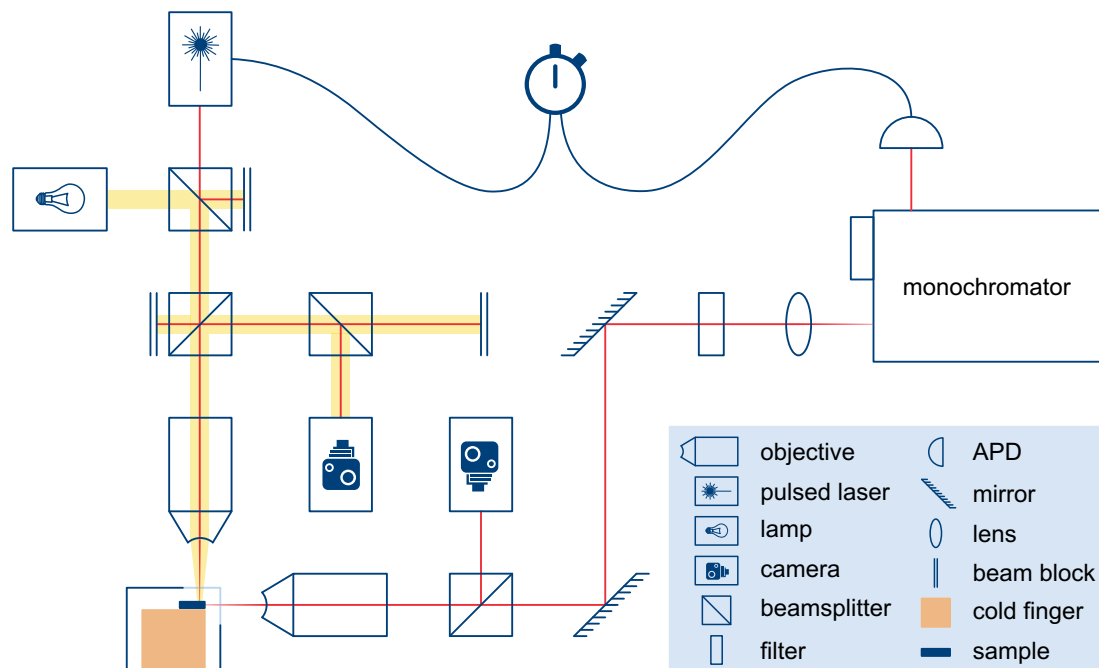


Figure 3.5 | Schematic of the setup for time-resolved photoluminescence spectroscopy.

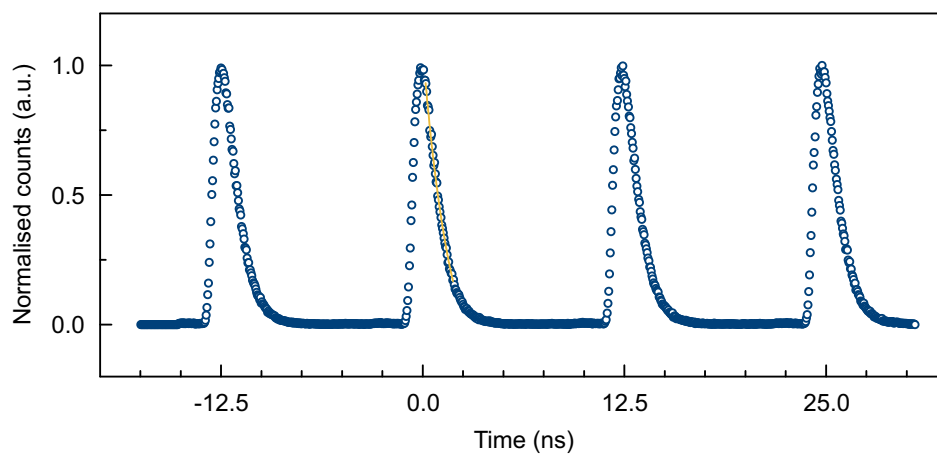


Figure 3.6 | Typical signal of time-resolved photoluminescence spectroscopy. Exponential fitting of the falling edge of the signal (shown in yellow) allows for the extraction of information about radiative lifetimes.

Figure 3.6 shows a typical signal of time-resolved photoluminescence spectroscopy. The signals at integer multiples of 12.5 ns are a result of consecutive excitation pulses from the excitation laser, which operates at a repetition frequency of 80 MHz. Information about the radiative lifetime of the corresponding excitonic state in the quantum dot can be extracted from this signal by fitting an exponential function to the falling edge of the signal [195].

3.3.3 Hanbury Brown and Twiss interferometry

The photon statistics of emission from a device is studied with autocorrelation measurements using a Hanbury Brown and Twiss setup, which was originally employed for experiments in astronomy [196]. The corresponding setup is shown in Fig. 3.7. Similarly to the the time-resolved photoluminescence spectroscopy described in the previous subsection, the device emission is collected and spectrally filtered with the monochromator. However, the spectrally filtered emission is split with a 50/50 beamsplitter and recorded with a pair of avalanche photo diodes operated in the Geiger mode. Coincidences are recorded electronically as a function of the time delay between the detection events on the avalanche photo diodes. In the limit of low count rates, the histogram of these coincidences gives a direct measure of the second order correlation function [18, 197]

$$g^{(2)}(\tau) = \frac{\langle I(t)I(t+\tau) \rangle}{\langle I(t) \rangle^2}, \quad (3.10)$$

which describes the temporal correlation between the intensity I of a light field and that after a delay τ . A perfect single photon source is characterised by the absence of two-photon pulses, and hence by a vanishing second order correlation function at $\tau = 0$ [18]. However, in experiments, background emission often leads to non-zero values for $g^{(2)}(\tau = 0)$, as illustrated by typical experimentally observed histograms for continuous-wave and pulsed excitation in Fig. 3.8 a and b, respectively. It is still possible to confirm whether the emission stems from an individual single photon source, since the second order correlation function of the combined emission of a set of N perfect single photon sources can be shown to obey [198]

$$g^{(2)}(0) \simeq 1 - \frac{1}{N}. \quad (3.11)$$

The condition $g^{(2)}(\tau = 0) < 0.5$ is therefore sufficient to prove that the emission stems from an individual single photon source.

In conclusion, this chapter presented the methods employed in order to achieve the experimental demonstration of integrable single photon sources in the following chapters. The simulation tools used to optimise device designs were introduced, followed by a description of the nanofabrication steps required to manufacture these devices. Finally, the experimental techniques for the optical characterisation of the devices were discussed. The remainder of this dissertation will be dedicated to the presentation and discussion of experimental results.

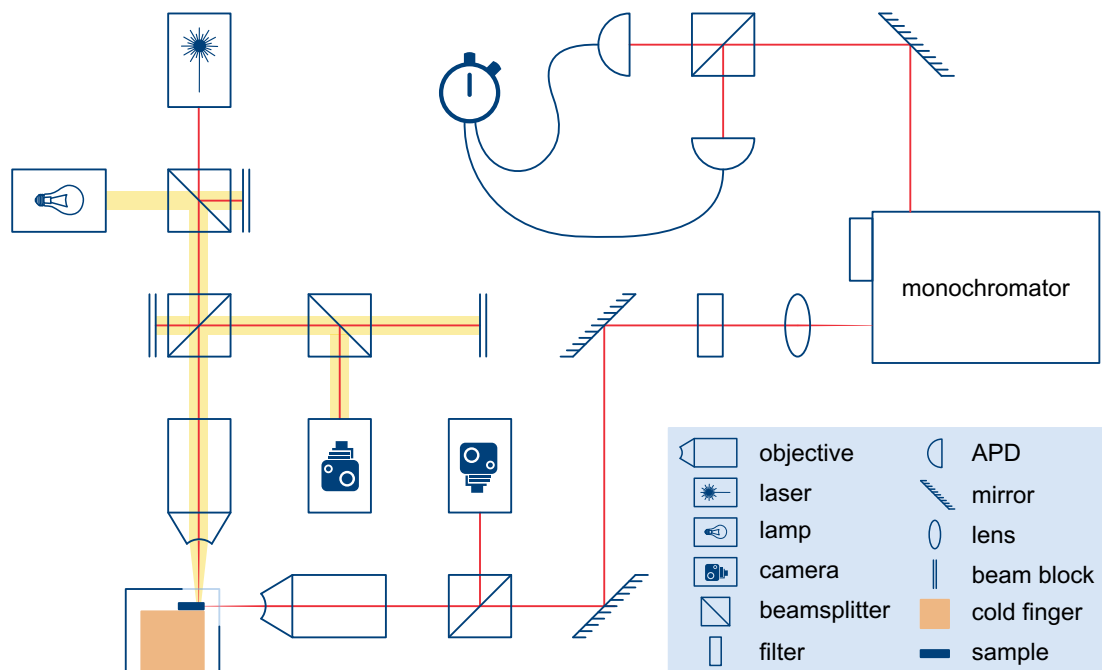


Figure 3.7 | Schematic of the Hanbury Brown and Twiss setup.

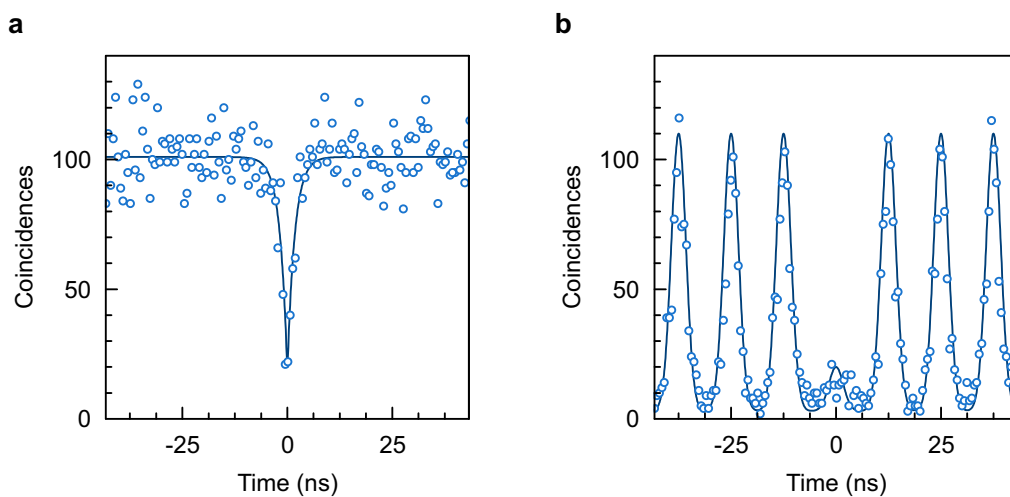


Figure 3.8 | Autocorrelation functions of a quantum dot transition. The circles represent data recorded experimentally with a Hanbury Brown and Twiss interferometer. The lines show the corresponding fit function. **a**, Autocorrelation function under continuous-wave optical excitation. **b**, Same for pulsed excitation.

4 Slow-light enhanced on-chip quantum light source

As motivated in the introduction, the scalability of schemes in optical quantum information processing requires in-plane single photon sources that can be integrated into a planar light circuit. This chapter describes the first demonstration of such an on-chip quantum light source at optical wavelengths [199, 200], and Fig. 4.1 illustrates the device concept used to achieve this. Single photons are generated by the spontaneous recombination of excitonic states in an indium arsenide quantum dot (shown in yellow), which is embedded at the centre of a gallium arsenide photonic crystal slab and optically excited from the top by focusing a laser beam onto the slab (red cone). By coupling the quantum dot to a slow-light mode of a photonic crystal waveguide [137, 138], two highly desirable effects are realised: first, the spontaneous emission rate is Purcell enhanced due to the larger density of optical states at the edge of the Brillouin zone; and second, emission of single photons is emitted into a waveguide in the chip plane, making the device monolithically integrable with on-chip quantum photonic circuits. The unidirectional waveguide is terminated in one end by a photonic crystal mirror in order to direct all emission into the negative x -direction, and the in-plane emission is collected from the device at the other end of the waveguide, which is formed by an etched gallium arsenide–vacuum interface. Please note that in the remainder of this chapter, the coordinate system is used as defined in Fig. 4.1.

This chapter is subdivided into two sections, the first of which comprises the theoretical discussion of slow-light resonances in photonic crystal waveguides as well as the design optimisation by parameter scans with finite-difference time-domain simulations. This is followed by the second section, which contains a brief description of the real device under study and the comprehensive optical characterisation of this device, including the demonstration of slow-light enhanced on-chip single photon emission.

4.1 Slow-light effects in photonic crystal waveguides

This section contains a discussion of the theoretical underpinnings of slow-light effects in photonic crystal waveguides and of the optimal structural parameters for a device exploiting these effects for Purcell-enhanced on-chip single photon emission.

As mentioned in the introduction to this chapter, on-chip single photon emission can be

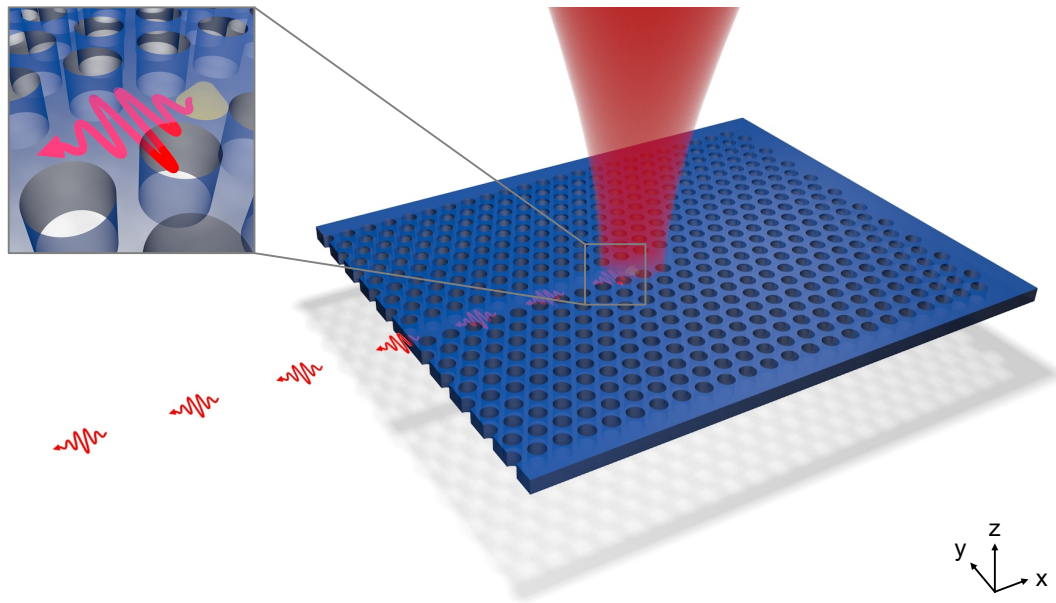


Figure 4.1 | Illustration of the device concept for an in-plane single photon source. The quantum dot (yellow) is embedded in a unidirectional waveguide in a photonic crystal slab (blue). It is optically excited with a focussed laser beam (red cone) and emits single photons, here shown as wavepackets. The inset shows an enlarged illustration of the quantum dot emitting a single photon into the unidirectional waveguide.

realised by coupling a quantum dot to a W1 photonic crystal waveguide [200, 201], which is formed by the omission of one row of holes along the $\Gamma - K$ direction in a hexagonal array of vacuum-filled holes in a gallium arsenide slab. In a two-dimensional photonic crystal waveguide, light is guided in the plane by the band gap of the adjacent photonic crystal structure, and out-of plane by total internal reflection at the gallium arsenide–vacuum interface. Figure 4.2 a shows the band diagram of such an infinite photonic crystal waveguide as calculated with the plane wave expansion method. Since the waveguide is periodic in the x -direction, the band diagram is plotted for the first Brillouin zone $\Gamma - K'$ of the projected hexagonal lattice [127]. The light cone defines the continuum of states that is formed by the leakage of light out of the slab plane into the surrounding vacuum cladding, which is due to the limitations of the confinement by total internal reflection. Below this light cone, a photonic band gap forms between two continua of states in the patterned slab. Within this band gap, several guided modes are present. Due to the periodicity of the waveguide along the x -direction, this band diagram expands symmetrically beyond $k = 0.5$ (or K'). The dispersion of these guided modes has a vanishing slope at the edge of the Brillouin zone [127] because dispersion relations are generally smooth [202]. Since the first derivative of these dispersion

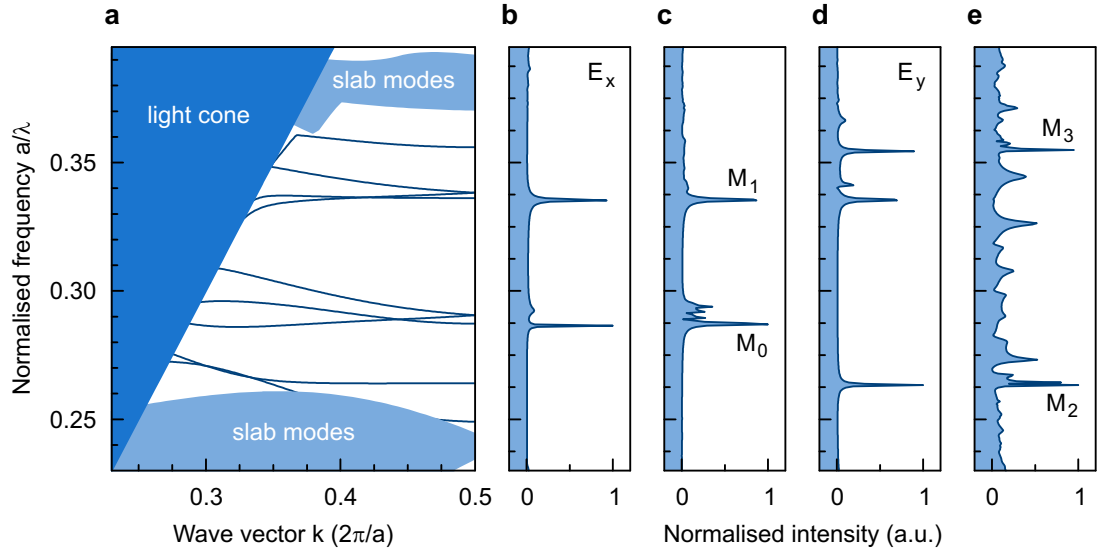


Figure 4.2 | Band diagram and slow-light resonances of a W1 waveguide. The photonic crystal slab is characterised by $\frac{r}{a} = 0.345$ and $\frac{d}{a} = 0.637$. **a**, Band diagram for an infinite waveguide. **b**, Resonances of an infinite waveguide for the x -polarised electric field component. **c**, Resonances of a unidirectional waveguide for the x -polarised field component. **d**, Resonances of an infinite waveguide for the y -polarised electric field component. **e**, Resonances of a unidirectional waveguide for the y -polarised field component.

relations $\frac{\partial\omega}{\partial k}$ corresponds to the group velocity, this means that there are slow-light modes at the edge of the Brillouin zone. From a physical point of view, these slow-light modes stem from the partial coherent backscattering of the propagating waves at each unit cell of the crystal, which results in a slowly propagating interference pattern [137]. The formation of slow-light modes leads to an increase in the local optical density of states at these particular frequencies. Spectral matching of the excitonic transition dipole of the quantum dot to these slow-light modes can hence lead to Purcell enhancement of the spontaneous emission rate in photonic crystal waveguides [201, 203].

The properties of the slow-light induced resonances in such a photonic crystal waveguide structure can be studied in greater detail with finite-difference time-domain simulations. Figures 4.2 b and d show the mode structures for an *infinite* waveguide for x - and y -polarised electric field components, respectively. Please note that only modes with an even parity with respect to the x - y -plane are studied since the main transition dipoles of indium arsenide quantum dots are in this plane [87]. Therefore, only the E_x and E_y field components appear in this discussion. Most resonances found with these finite-difference time-domain simulations are directly attributed to the slow-light modes shown in the band diagram. The corresponding mode structures of a *finite, unidirectional* waveguide such as described in the in-

roduction to this chapter are shown in Figs. 4.2 c and e. The resonances found for the infinite waveguide persist in the unidirectional device. However, the mode structure for the E_y field component, with its propagation direction along the waveguide, exhibits several broad resonances of lower intensity that partly obscure some of the features of the mode structure of the infinite waveguide. These resonances are attributed to Fabry-Perot reflections between the photonic crystal mirror and the gallium arsenide – vacuum interface terminating the waveguide [203]. Among the four clearly discernible slow-light resonances of the unidirectional waveguide labelled M_0 to M_3 in Figs. 4.2 c and e, only the y -polarised modes (M_2 and M_3) are of interest for the desired functionality as an in-plane single photon source. This is because only the y - and z -polarised electric fields propagate along the direction of the waveguide and only these polarisations can be collected at the exit of the waveguide, whereas x -polarised light can only be observed as out-of-plane emission. The indium arsenide quantum dots used for this experiment emit at about 900 nm, such that devices must be designed with modes at this target wavelength. Hence, a device for coupling a quantum dot to the M_2 mode (appearing at $\frac{a}{\lambda} = 0.263$ for the finite structure) would require a lattice constant $a = 237$ nm, whereas a device designed for the M_3 mode (at $\frac{a}{\lambda} = 0.354$) would have to exhibit a lattice constant of 319 nm. Since slow light modes are extremely sensitive to unavoidable fabrication imperfections [203, 204] and these imperfections are less significant in larger structures, it is favourable to focus on the M_3 mode.

Figures 4.3 a-c show the mode profiles of this mode for the E_x , E_y , and H_z field components, respectively. The top views (top left panels) show that the mode is well confined to the waveguide area and decays within a few periods in the photonic crystal. The side views (bottom and right panels) confirm the good mode confinement within the slab due to total internal reflection as the fields barely extend into the vacuum cladding. These mode profiles also illustrate the origin of the y -polarisation of the M_3 mode. Since the E_x field is anti-symmetric with respect to the centre line of the waveguide, it cancels in the far field, whereas the mirror symmetry of the E_y field prohibits this cancellation [205]. This results in y -polarised light emission in the far field. Analogous considerations apply to the x -polarised modes, which is exemplified for the M_0 mode in Figs. 4.3 d-f. Here, the anti-symmetry of the E_y field leads to cancellation in the far field, whereas the symmetry of the E_x field prohibits this cancellation, leading to x -polarised emission in the far field.

This concludes the discussion the theoretical properties of a unidirectional waveguide, which led to the identification of mode M_3 as a suitable target mode for the demonstration of slow-light enhanced on-chip single photon emission from a quantum dots. The following subsection will discuss the optimisation of the structural design parameters for this mode.

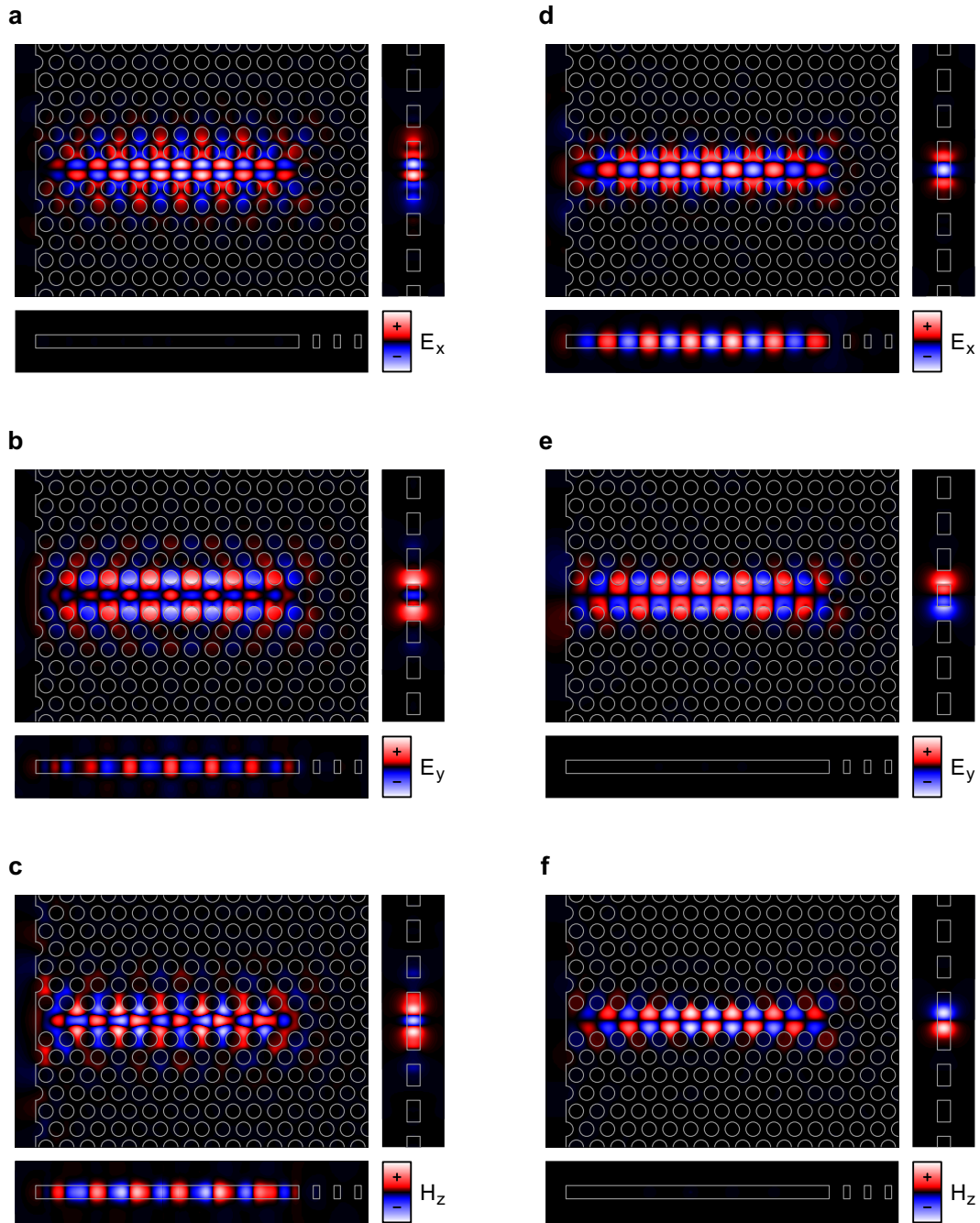


Figure 4.3 | Mode profiles of selected modes of the unidirectional waveguide. The photonic crystal slab is characterised by $\frac{r}{a} = 0.345$ and $\frac{d}{a} = 0.637$. In each subfigure, the top left panel shows the x - y -plane at the middle of the slab, the top right panel shows the y - z -plane at a field maximum, and the bottom panel shows the x - z -plane at the centre of the waveguide. **a**, Mode profile of the M_3 mode for the E_x field component. **b**, E_y field component. **c**, H_z field component. **d**, Mode profile of the M_0 mode for the E_x field component. **e**, E_y field component. **f**, H_z field component.

4.1.1 Discussion of design parameters

Conceptually, the general device design has been discussed theoretically [201, 204, 206] and studied experimentally [203], such that some of the design parameters have been taken from that work. The Q -factors of the slow-light modes in a unidirectional waveguide have been found to increase with increasing length of the waveguide since the confinement is based on coherent backscattering at the periodic array of neighbouring holes [137, 206]. On the other hand, increasing waveguide lengths result in larger mode volumes and a decreasing extraction efficiency at the gallium arsenide–vacuum interface [201]. A waveguide length of 12 unit cells has been identified to be a reasonable compromise [203]. For such a waveguide length, the termination of the waveguide with the gallium arsenide–vacuum interface *between* the waveguide’s nearest neighbour holes, rather than *across* these holes, leads to larger maximum Purcell factors [206]. This increases the waveguide length to 12.5 unit cells. Figure 4.3 suggests that the field components theoretically decay within a few periods in the photonic crystal. However, for the real device, ten periods of the photonic crystal to both sides of the waveguide and an equally thick photonic crystal mirror at one end of the unidirectional waveguide were chosen to balance a potential decrease in reflectivity in the real structure due to fabrication imperfections. Please note that the device shown in Fig. 4.1 exhibits these features.

While the general design parameters discussed in the previous paragraph apply to the study of all modes in unidirectional waveguides, the optimal hole diameter and the slab thickness differ for different modes. The dependencies of the Q -factor and mode volume of the M_3 mode on hole radius and slab thickness were simulated in order to find the optimum values. The results are shown in Fig. 4.4. As the normalised hole radius $\frac{r}{a}$ is varied from 0.34 to 0.42, the Q -factor (Fig. 4.4 a, top panel) oscillates between approximately 3750 and 6000. The origin of these oscillations is not very well understood, but these results imply that in the device processing, great care has to be taken to obtain a suitable hole radius. At $\frac{r}{a} < 0.34$, the Q -factor rapidly decreases to almost zero because the mode shifts spectrally out of the photonic band gap. In this range, the mode volume (middle panel) also greatly increases as a result of the poor confinement of the light to the waveguide region. For the normalised hole radius range from 0.34 to 0.42, however, the mode volume shows little variation about an average of about $2.9 \left(\frac{\lambda}{n}\right)^3$. Correspondingly, the maximum obtainable Purcell factor (bottom panel) as a function of the normalised hole radius follows the oscillatory behaviour of the Q -factor, with maxima of approximately 150 for $\frac{r}{a} = 0.35$ and $\frac{r}{a} = 0.37$.

With increasing normalised slab thickness, the Q -factor of the M_3 mode (Fig. 4.4 b, top panel) increases monotonically from 4050 at $\frac{d}{a} = 0.45$ and peaks at 6260 at $\frac{d}{a} = 0.8$. For even thicker slabs, the Q -factor decreases again. As intuitively expected, the mode volume generally increases slightly with increasing slab thickness (middle panel). For the maximum Purcell factors (bottom panel), this translates into a moderate increase with increasing slab

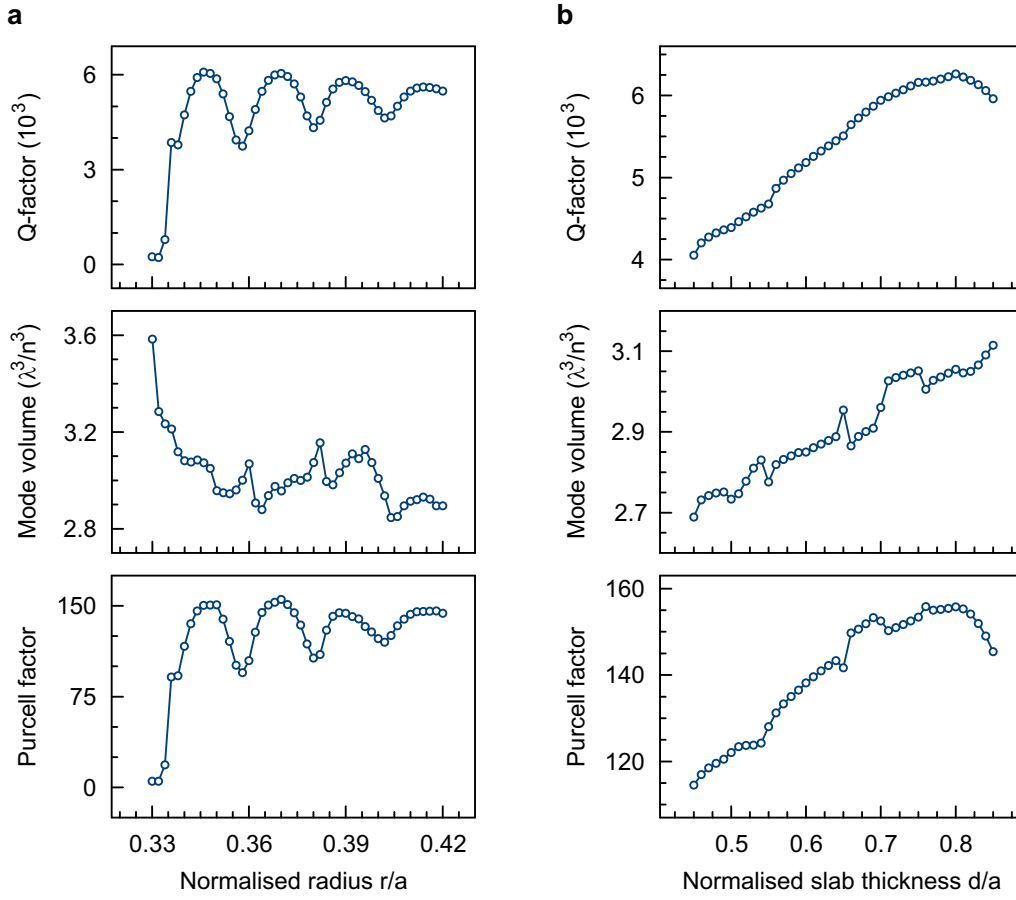


Figure 4.4 | Finite-difference time-domain optimisation scans for the unidirectional waveguide device. The figures show the Q-factor (top panels), mode volume (middle panels), and maximum Purcell factor (bottom panels) of the M_3 mode. **a**, Scan of the normalised hole radius $\frac{r}{a}$ for a fixed normalised slab thickness $\frac{d}{a} = 0.69$. **b**, Scan of the normalised slab thickness $\frac{d}{a}$ for a fixed normalised hole diameter $\frac{r}{a} = 0.35$.

thickness. However, for a wide range of slab thicknesses, from $\frac{d}{a} = 0.66$ to 0.84 , the Purcell factor remains relatively constant at about 150. This implies that the slab thickness is less critical than the hole radius for obtaining devices with a strong Purcell effect.

In conclusion, the optimised design parameters for the slow-light induced Purcell enhancement with the M_3 mode in a unidirectional photonic crystal waveguide are $\frac{r}{a} = 0.35$ or 0.37 and $\frac{d}{a} = 0.8$. The corresponding Q-factor is 6260, the mode volume is about 2.9 cubic wavelengths, and the resulting maximum Purcell factor is about 150. The next section will describe the experiments carried out with devices that were designed with these values in mind.

4.2 Experimental demonstration of an in-plane single photon source

For the experimental demonstration of slow-light enhanced on-chip single photon emission, devices were designed with a small range of lattice constants around 319 nm, for which the M_3 mode is expected to appear at the emission wavelength of the quantum dots of around 900 nm. The nominal $\frac{r}{a}$ ratio was 0.35, one of the optimised values determined in the previous section, and the slab thickness was 200 nm. Scanning electron micrographs of devices like the one studied in this section are shown in Fig. 4.5. In Fig. 4.5 b in particular, the bright halo surrounding the device shows how far the slab has been under-etched. The remaining aluminium gallium arsenide sacrificial layer is clearly discernible as a slightly brighter strip at the cleaved face of the sample. The particular device discussed in detail in this section has a lattice constant of 314 nm. The analysis of top view scanning electron microscope images of devices from the same chip showed that the holes in the photonic crystal have a radius of (108.3 ± 1.5) nm, corresponding to $\frac{r}{a} = 0.345 \pm 0.005$, very close to the designed value of 0.35. The slab thickness of 200 nm corresponds to a normalised value of $\frac{d}{a} = 0.637$. Please note that the band diagram and the mode structures in Fig. 4.2 and the mode profiles in Fig. 4.3 were calculated for these values, such that they can be referred to for the theoretical properties of the device studied in this section.

The comprehensive optical characterisation of the device includes the spectral characterisation with micro-photoluminescence experiments, the study of the temporal evolution of

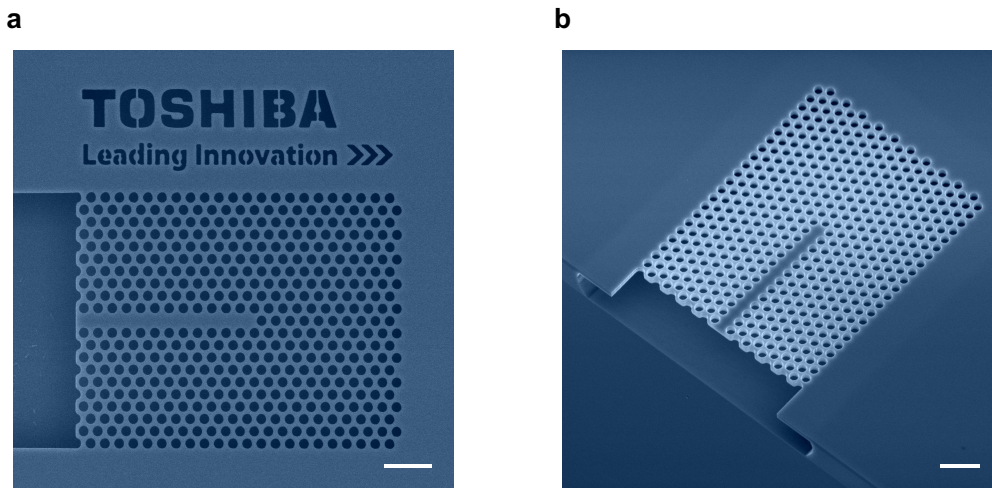


Figure 4.5 | Unidirectional waveguide devices for slow-light enhanced single photon emission. The scale bars correspond to 1 μm . **a**, Top view of a device. **b**, Oblique view of a device. The sacrificial layer of AlGaAs is clearly discernible on the cleaved face of the sample.

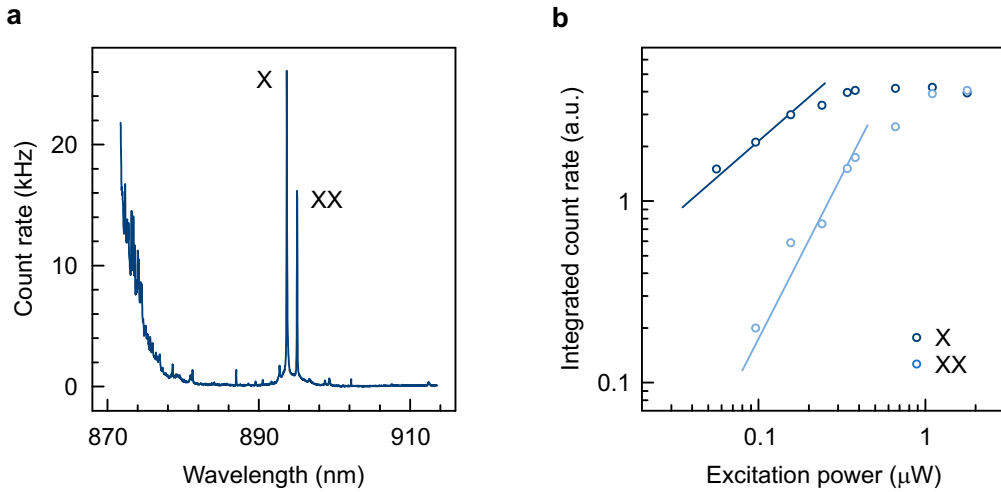


Figure 4.6 | In-plane emission spectrum of the unidirectional waveguide device. All data was recorded at $T = 5$ K. **a**, The spectrum is dominated by two sharp transitions (X and XX), while the wetting layer extends to about 880 nm. The spectrum was recorded for $P_{\text{ex}} = 1.1 \mu\text{W}$. **b**, The power dependence identifies the dominant transitions as exciton (X) and biexciton (XX) transitions of a quantum dot.

the excitonic states in the quantum dot with time-resolved photoluminescence, and an analysis of the photon statistics with autocorrelation experiments in a Hanbury Brown and Twiss setup. The corresponding results will be presented in the following in individual subsections.

4.2.1 Spectral characterisation

For the spectral characterisation in micro-photoluminescence experiments, the device was optically excited with the pulsed diode laser emitting at a central wavelength of 780 nm. Figure 4.6 a shows the in-plane emission spectrum from the device under study at $T = 5$ K. The spectrum is dominated by two sharp, bright transitions appearing at wavelengths of $\lambda = 893.7$ nm (labelled X) and $\lambda = 895.1$ nm (labelled XX), respectively. Other notable features of the spectrum include the tail of the wetting layer, extending up to a wavelength of approximately 880 nm, as well as other transitions of very low intensity. The dependency of the dominant transitions' emission intensity on the excitation power is shown in Fig. 4.6 b. For both transitions, the signal intensity increases for excitation powers $< 0.3 \mu\text{W}$ and levels off at higher powers due to saturation. The approximately linear ($\propto P^{0.8}$) and quadratic ($\propto P^{1.8}$) dependencies at lower powers allow for the attribution of the lines to excitonic (X) and biexcitonic (XX) transitions in a quantum dot, respectively [47].

The polarisation of the photoluminescence signal was studied by inserting a linear polariser between the collecting microscope objective and the spectrometer. In order to avoid artefacts due to the polarisation-dependent efficiency of the blazed grating in the spectrome-

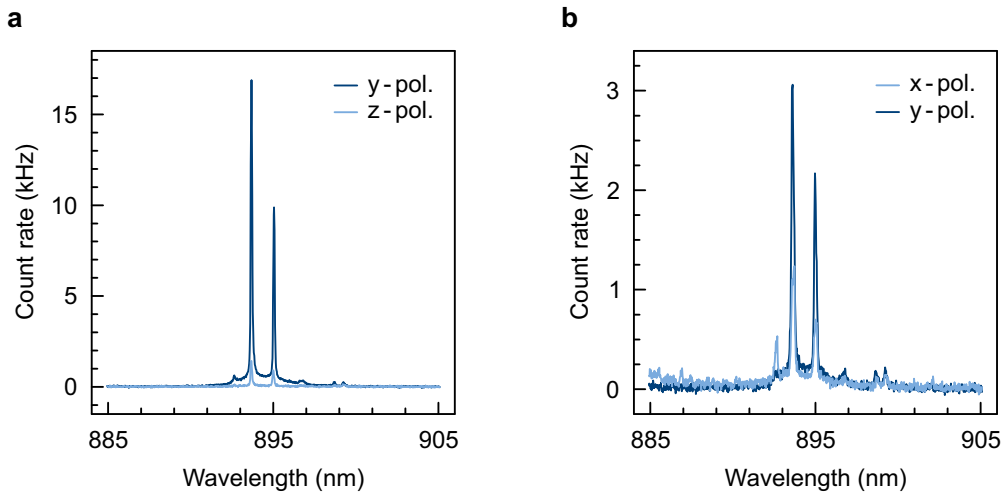


Figure 4.7 | Polarised emission spectra of the unidirectional waveguide device. All spectra were recorded at $T = 5$ K and $P_{\text{ex}} = 340$ nW. **a**, The in-plane emission is strongly y -polarised (92%). **b**, The out-of-plane emission is slightly y -polarised (71%) and considerably less intense than the in-plane emission.

ter, a half-wave plate was used to rotate one of the polarisations by 90° . Figure 4.7 a shows the polarised photoluminescence signals for the in-plane emission, which is found to be highly y -polarised (92%). This is in good agreement with the finding that the transition dipoles of a semiconductor quantum dot are directed in the plane of the chip [87], i.e. in the x - y -plane in the coordinate system used here. The small z -polarised component of the in-plane emission is attributed to polarisation scattering of the signal in the waveguide [203].

The polarisation of the out-of-plane emission was studied by collecting the light with the same microscope objective that is used for focussing the excitation light and directing the emission into the spectrometer. As shown in Fig. 4.7 b, the out-of-plane emission is slightly y -polarised (71%). This imbalance hints at a perturbation of the spontaneous recombination in the quantum dot, potentially owing to the Purcell effect. A comparison of Figs. 4.7 a and b also shows that the emission is highly anisotropic in that the in-plane emission is approximately four times brighter than the out-of-plane emission. Since this large difference is unlikely to arise from differences in the collection efficiencies alone, this is an indication of the coupling of the transition in the quantum dot to a waveguide mode.

A fitting procedure of the spectrum in a wavelength window about the dominant lines with Lorentzian functions reveals the presence of a broad mode. Figure 4.8 a shows the spectrum and the broad Lorentzian centred at $\lambda = 894.1$ nm as a light blue area. For the device under study with its lattice constant of $a = 314$ nm, the y -polarised slow-light mode M_3 is theoretically predicted to be spectrally located at $\lambda = 887.0$ nm. The good agreement between the experimental observation and the theoretical prediction allow for the identification of the M_3

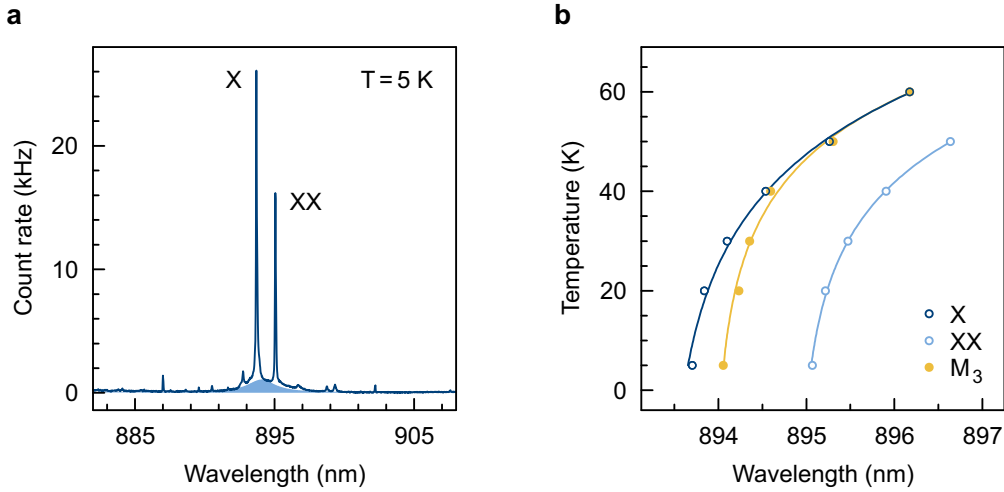


Figure 4.8 | Identification of the slow-light mode in the spectrum. All spectra were recorded at $P_{\text{ex}} = 240$ nW. **a**, The emission spectrum at $T = 5$ K. Lorentzian fitting reveals the presence of a mode, highlighted in light blue. **b**, Spectral positions of the exciton (X) and biexciton (XX) transitions and the mode (M_3) as a function of temperature in a range from 5 K to 60 K. The lines are guides to the eye.

mode in the emission spectrum of the device. From the fit, a Q -factor of 600 can be extracted, which is about one order of magnitude lower than predicted with simulations. This deviation is attributed to the detrimental effect of the active indium arsenide layer in the structure [207], which was not accounted for in the simulation, and to the sensitivity of slow-light modes to fabrication imperfections [203, 204]. This finding reaffirms the original preference of the M_3 mode in larger devices over the M_2 mode in smaller ones.

Due to the broadness of the mode, both the exciton and the biexciton transition overlap spectrally with the slow-light mode at $T = 5$ K (see Fig. 4.8 a). However, neither transition is fully in resonance. This changes when the temperature is increased from 5 K to 60 K, as shown in Fig. 4.8 b. The transitions in the quantum dot and the slow-light mode redshift at different rates with increasing temperature: the two transitions shift at a similar rate due to the temperature-dependence of the band gaps of indium arsenide and gallium arsenide [208]. In contrast, the mode of the photonic crystal structure redshifts at a much slower rate as a result of the temperature-dependence of the refractive index of gallium arsenide [209]. This leads to the exciton transition and the mode being thermo-optically tuned [63] into full resonance at $T = 60$ K. If the quantum dot is coupled to the slow-light mode, this temperature tuning of the exciton transition into full spectral resonance with the mode should lead to modifications of the lifetime of the excitonic state, which will be studied in the following section.

4.2.2 Time-resolved photoluminescence and the Purcell effect

The temporal evolution of the carrier populations of the quantum dot was studied with in-plane time-resolved photoluminescence experiments. Figure 4.9 a shows the recorded signal of the exciton transition in a temperature range from 5 K to 60 K. Exponential fitting of the falling edges of the signals shows that the lifetime decreases with increasing temperature from 0.9 ns at $T = 5$ K to 0.7 ns at $T = 60$ K. Since this cannot be accounted for by the temperature dependence of the radiative lifetime of exciton states in uncoupled indium arsenide quantum dots, which was actually found to increase slightly in this temperature range [210], this decrease in lifetime is a direct consequence of the increased coupling between the exciton transition and the slow-light mode due to better spectral overlap.

The measured change in the radiative lifetime with temperature tuning corresponds to a Purcell enhancement of 1.3. However, even at $T = 5$ K, the exciton transition is partly in resonance with the slow-light mode. In order to obtain a good estimate of the full Purcell factor for the exciton transition, the lifetime at maximum coupling (i.e. at $T = 60$ K) is to be compared to the lifetime of the excitonic state in an average quantum dot in an unpatterned part of the sample. Unfortunately, the limited collection efficiency for quantum dots in bulk gallium arsenide combined with the low emission intensity at $T = 60$ K leads to count rates that

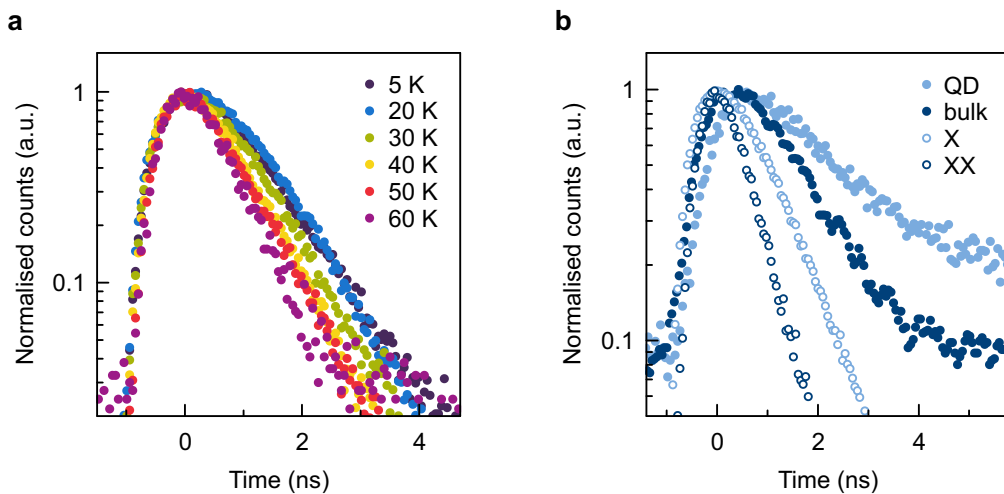


Figure 4.9 | Time-resolved photoluminescence signals of the device. **a**, Signal of the exciton transition (X) at different temperatures. As the temperature is increased from 5 K to 60 K, the exciton lifetime decreases from 0.9 ns to 0.7 ns. The signals were recorded at $P_{\text{ex}} = 240$ nW. **b**, Signals at $T = 5$ K of an off-resonant quantum dot transition (QD , at 887 nm, $\tau = 2.7$ ns), an average excitonic quantum dot transition in an unpatterned section of the sample ($bulk$, $\tau = 1.5$ ns), the exciton transition (X , $\tau = 0.9$ ns), and the biexciton transition (XX , $\tau = 0.6$ ns). The excitation power for these measurements ranged from 0.1 – 1.1 μW .

are too low for time-resolved measurements. However, due to the temperature dependence of the lifetime described in the previous paragraph, a comparison of the coupled lifetime at $T = 60$ K and the bulk lifetime at $T = 5$ K gives a good conservative estimate of the Purcell factor. Figure 4.9 b shows the time-resolved photoluminescence signal of different transitions in the sample at $T = 5$ K. The signal labelled *bulk* corresponds to the excitonic transition in a quantum dot in an unpatterned part of the sample with a radiative lifetime of 1.5 ns, which is close to the average lifetime measured for a set of ten such dots. This yields an estimate of the slow-light induced Purcell enhancement for the fully coupled exciton transition of 2.1. The theoretically expected Purcell enhancement for the M_3 mode with a Q -factor of 600 is 29, and the deviation is mainly attributed to poor spatial overlap between the electric field of the mode and the quantum dot in the device under study.

The signal labelled *QD* in Fig. 4.9 b corresponds to the well off-resonant weak transition at $\lambda = 887$ nm in Fig. 4.8 a. The extracted lifetime is 2.7 ns, which corresponds to Purcell suppression of that transition by a factor of 1.8. Finally, the radiative lifetime of the biexciton state (labelled *XX* in Fig. 4.9 b) was found to be 0.6 ns, shorter than that of the exciton state with its better spectral overlap. This finding agrees with previous studies of the lifetimes of different states in indium arsenide quantum dots [47].

In conclusion, the results presented in the previous subsections showed Purcell enhanced in-plane emission of a single indium arsenide quantum dot coupled to a slow-light mode in a photonic crystal. However, the main motivation for these experiments was the demonstration of an on-chip quantum light source. Therefore, a study of the photon statistics of the in-plane emission is presented in the following subsection.

4.2.3 Photon statistics

In order to analyse the photon statistics and hence confirm the quantum nature of the light source under study here, autocorrelation measurements were performed on the in-plane emission with a Hanbury Brown and Twiss experiment. Since applications in optical quantum information processing require on-demand sources of single photons, the photon statistics of the in-plane emission under pulsed excitation was studied first. This is followed by autocorrelation measurements under continuous-wave excitation to study the maximum device performance.

Pulsed excitation – on-demand source

For the autocorrelation experiments on the on-demand emission of the device, it is optically excited with the pulsed diode laser emitting at a central wavelength of 780 nm with a repetition frequency of 80 MHz. Figure 4.10 a shows the coincidence histogram measured for the in-plane emission of the excitonic transition, which shows well defined accumulations of coincidences at time delays of integer multiples of 12.5 ns. These coincidences stem from

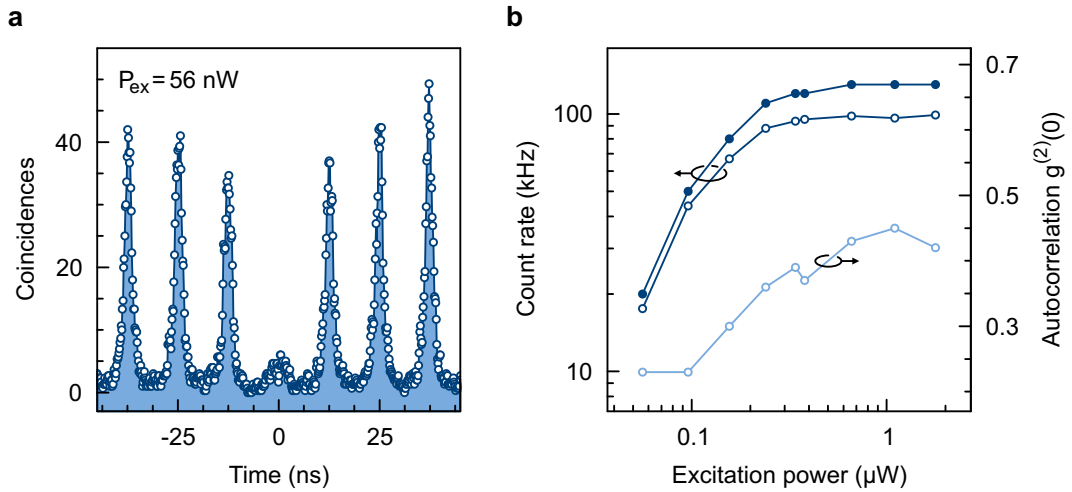


Figure 4.10 | Photon statistics of the in-plane emission under pulsed excitation. All measurements were taken for the exciton transition (X) at $T = 5$ K. **a**, Coincidence pattern for low excitation power. **b**, Photon count rate (dark blue solid discs), corrected single-photon count rate (dark blue circles), and autocorrelation function $g^{(2)}(0)$ (light blue circles) as a function of the excitation power.

photons emitted after consecutive excitation pulses. At a time delay $\tau = 0$ ns, however, the peak is strongly suppressed, confirming the demonstration of an on-demand single photon source. By integration of the central peak and normalisation to neighbouring peaks, a value of $g^{(2)}(\tau = 0) = 0.23$ can be inferred. The remaining coincidence events for zero time delay correspond to occasional multi-photon pulses, which are attributed to background emission from the substrate.

Figure 4.10 b shows the results of a more detailed study of the device performance as an on-demand single photon source. The occurrence of multi-photon pulses, indicated by the values of $g^{(2)}(0)$ (light blue circles) is found to increase with higher excitation powers owing to a combination of the saturation of the exciton transition and increasing emission from the substrate, the wetting layer and other quantum dots into the slow-light mode [211, 212]. At the same time, the combined count rate on the avalanche photo diodes (dark blue solid discs) increases substantially and levels off at about $0.3 \mu\text{W}$ due to saturation. Please note that this behaviour agrees well with the power dependence of the exciton transition shown in Fig. 4.6 b. In order to correct these count rates for multi-photon events, they were multiplied by a factor of $\sqrt{1 - g^{(2)}(0)}$ [213], yielding the actual single photon detection rates (dark blue circles). The maximum single photon detection rate is found to be 99 kHz for a pump power of $1.78 \mu\text{W}$. Given that the total detection efficiency of the setup was experimentally determined to be 1% (the largest losses occur in the spectrometer and the avalanche photo diodes with efficiencies of 7% and 40%, respectively), this translates into a single photon emission

rate into the first lens of 9.9 MHz. Furthermore, the extraction efficiency at the facet terminating the unidirectional waveguide has been calculated theoretically to be 53% for a similar device, while the remaining radiation is mainly lost to vertical leakage [201]. In the experiment, this value certainly represents an upper bound, such that this number gives a good conservative estimate. This yields an internal single photon emission rate of 18.7 MHz.

In order to deduce the device efficiency, this rate is to be compared to the excitation frequency. Here, it has to be taken into account that in the non-resonant optical excitation scheme used here, the quantum dot is populated with charge carriers that enable the emission of y -polarised photons with a probability of only 50%. In the remaining cases, the charge carrier configuration allows only x -polarised photon emission. While this emission was observed in out-of-plane measurements (see also Fig. 4.7 b), it cannot be extracted in-plane. With quasi-resonant optical excitation schemes [52, 53, 214–216], the spin state of the exciton in the quantum dot can be prepared such that the subsequently emitted photon is always y -polarised. Unfortunately, the pulsed diode laser used here is not wavelength-tunable, such that quasi-resonant excitation could not be applied. Therefore, a suitable exciton state was only prepared with an effective average repetition rate of 40 MHz. This allows for an estimate of an upper bound for the internal device efficiency of 47%.

Continuous-wave excitation – maximum device performance

In order to study the maximum emission rate of the device, autocorrelation measurements similar to those described in the previous paragraph were carried out with continuous-wave excitation using a helium-neon gas laser emitting at 632.8 nm. Under this excitation, the quantum dot is repopulated with charge carriers immediately after the emission of a photon, such that the single photon emission rate is theoretically limited only by the radiative lifetime of the exciton in the quantum dot.

Figure 4.11 a shows a coincidence histogram for continuous-wave excitation. As opposed to the histogram for pulse excitation (Fig. 4.10 a), it does not exhibit well-defined accumulations of coincidences but a continuum (reflecting the continuous nature of the excitation) with a clear dip at $\tau = 0$, evidencing single photon emission. Normalised to the continuum, the $g^{(2)}(0)$ value is estimated as 0.30, slightly higher than the low-power value for pulsed excitation. This deviation is attributed to the limited time resolution of the avalanche photo diodes. Figure 4.10 b shows that $g^{(2)}(0)$ (light blue circles) increases with higher excitation power, similar to the behaviour for pulsed excitation. For $P_{\text{ex}} > 2.5 \mu\text{W}$, this value exceeds the threshold value of 0.5 for a photon source based on a single quantum emitter. Similarly to the pulsed case, the count rate under continuous-wave excitation (dark blue solid discs) increases with higher excitation power. The corrected single photon count rate (dark blue circles) peaks for an excitation power of $3.6 \mu\text{W}$ at 240 kHz (albeit with $g^{(2)}(0) = 0.60 > 0.5$). For $P_{\text{ex}} = 2.2 \mu\text{W}$, the highest excitation power with $g^{(2)}(0) < 0.5$, the corrected single photon

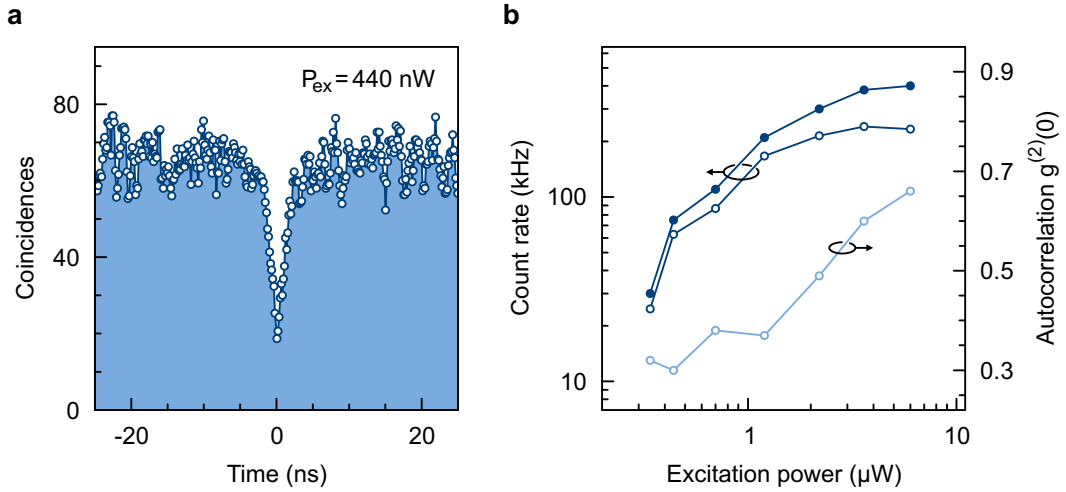


Figure 4.11 | Photon statistics of the in-plane emission under continuous-wave excitation. All measurements were taken for the exciton (X) line at $T = 5 \text{ K}$. **a**, Coincidence pattern for low excitation power. **b**, Photon count rate (dark blue solid discs), corrected single-photon count rate (dark blue circles), and autocorrelation function $g^{(2)}(0)$ (light blue circles) as a function of the excitation power.

count rate was 214 kHz. Taking into account the detection and collection efficiencies, this translates into an internal single photon emission rate of 40.4 MHz, which is about a factor of two higher than in the pulsed excitation case. This compares with a lifetime limited excitation rate of 1.1 GHz (the excitonic lifetime $T = 5 \text{ K}$ is 0.9 ns, see Fig. 4.9 a), about a factor of 14 higher than in the pulsed excitation case. This discrepancy by a factor of seven shows that the single photon emission rate under continuous-wave excitation is in fact not limited by the radiative lifetime. Possible limitations of the device performance include the longer lifetime of the spin configuration in the quantum dot that leads to the emission of x -polarised photons, which is not Purcell enhanced by the coupling to the slow-light mode; and the creation of dipole-forbidden dark states in the quantum dot. These limitations could be avoided by indirect [217] or quasi-resonant [53, 214, 216] excitation schemes and by using bright charged excitons in slightly doped [212] or charge-tunable [218] quantum dots, respectively.

In conclusion, a discussion of the theoretical underpinnings of slow-light effects in photonic crystal waveguides was presented in this chapter. Among several slow-light resonances present in a photonic crystal waveguide, the y -polarised M_3 mode was identified to be the most attractive for slow-light induced Purcell enhancement of the radiative transition in quantum dots, and the design parameters for this particular mode were discussed. Using an optimised device design, on-chip emission of single photons at optical wavelengths was presented for the first time. The coupling of an excitonic transition in a quantum dot to a slow-

light mode resulted in Purcell enhancement by an estimated factor of 2.1. On-demand single photon emission was demonstrated with a maximum emission frequency of 18.7 MHz, corresponding to an estimated internal device efficiency of up to 47 %. The maximum single photon emission rate under continuous-wave excitation was found to be 40.4 MHz, suggesting that this rate is not limited by the radiative lifetime of the corresponding transition.

5 Waveguide-coupled L3 cavities for on-chip single photon emission

The slow-light enhanced single photon source presented in the preceding chapter represents a major step towards fully integrated quantum photonic circuits. However, for applications in quantum information processing, single photon emission with a timing jitter less than the photon's coherence time is required in order to allow for on-demand two-photon interference with high visibility. This can be realised by shortening the radiative lifetime of the excitonic state in the quantum dot by Purcell enhancement of the spontaneous emission [219, 220]. As discussed in Chapter 2, strong Purcell enhancement requires a cavity with a large Q -factor and a small mode volume. However, devices relying on slow-light effects for Purcell enhancement exhibit relatively modest Q -factors and require a waveguide length of at least ten lattice constants to maximise Q -factors, which leads to comparatively large mode volumes.

In contrast, point defect cavities in photonic crystals slabs, such as the H1 or L3 cavity, simultaneously provide high Q -factors and mode volumes below one cubic wavelength, and are therefore much better suited for Purcell enhancement of the spontaneous recombination of excitonic states in quantum dots. However, stand-alone defect cavities direct most of their emission out of the chip plane and are therefore not suitable for integrated quantum photonics. To harness both the suitability of point defect cavities for Purcell enhancement and the integrability of photonic crystal waveguides, a combination of these two concepts is studied in this chapter. Figure 5.1 illustrates the device idea: the quantum dot as the emitter of single photons (shown in yellow) is coupled to a low mode volume, high- Q mode of a L3 defect cavity in a photonic crystal slab (see inset in Fig. 5.1). In order to allow for the on-chip extraction of single photons from the L3 cavity, it is evanescently coupled to a nearby photonic crystal waveguide. Analogous to the experiments in the previous chapter, the device is excited optically from the top (as illustrated by the red cone in Fig. 5.1), and the emission is collected in-plane with a second microscope objective (not shown).

The first section in this chapter is dedicated to the discussion and both the theoretical and experimental study of the complete mode structure of a stand-alone L3 defect cavity in order to identify the most suitable mode for the Purcell enhancement of radiative transitions in quantum dots. In the second section, the coupling of the L3 defect cavity to a photonic crystal waveguide is studied both with finite-difference time-domain simulations and experiments. Finally, on-chip single photon emission from such a waveguide-coupled L3 cavity is

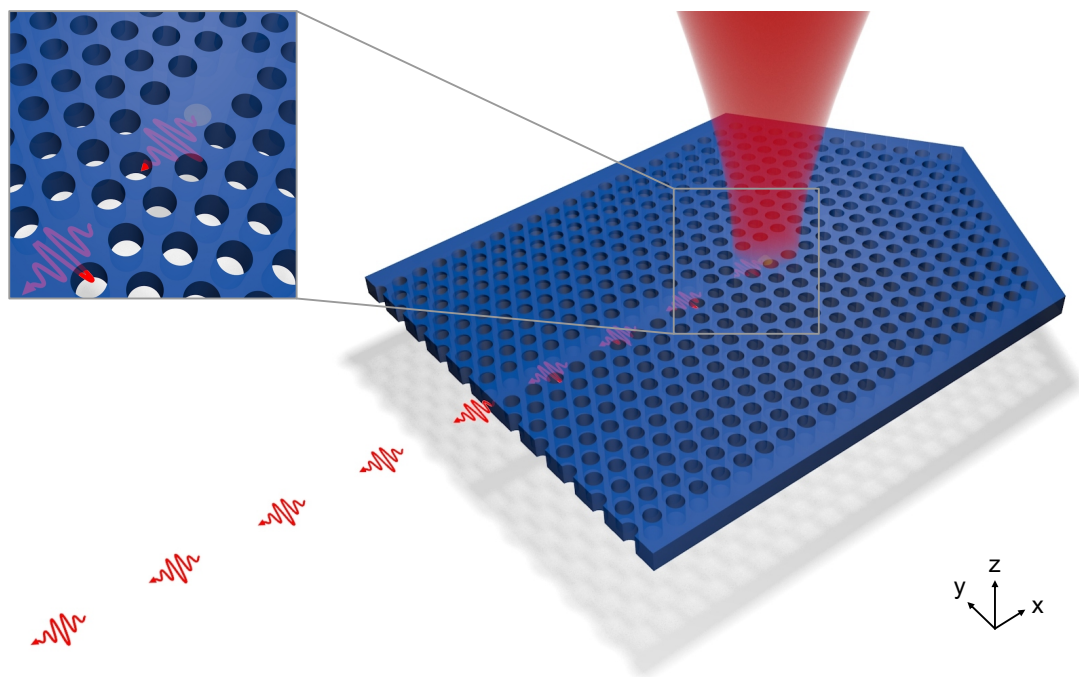


Figure 5.1 | Device concept for a waveguide-coupled L3 cavity for in-plane single photon emission. The quantum dot (yellow) is coupled to a low-volume, high- Q mode in a L3 defect cavity (inset). Single photons (shown as wavepackets) leak from the cavity into a photonic crystal waveguide, allowing for in-plane emission. The quantum dot is optically excited with a focussed laser beam (red cone).

presented in the third section.

5.1 Mode structure of the stand-alone L3 defect cavity

The L3 cavity is one of most popular nanocavity structures [131] and was the first type of photonic crystal defect cavity for which Q -factors exceeding 10000 were demonstrated experimentally [112]. It consists of three missing holes along a line in photonic crystal slab with a hexagonal lattice. A top view scanning electron micrograph of such a defect cavity surrounded by 10 periods of the photonic crystal is shown in Fig. 5.2 b. Figure 5.2 a shows the corresponding mode structure of this cavity as calculated with the finite-difference time-domain technique. Within the photonic band gap of the two-dimensional photonic crystal, the L3 cavity supports five different modes labelled M_0 through M_4 in order of decreasing normalised wavelength. This section is dedicated to the theoretical discussion and experimental study of this mode structure in order to identify the most suitable mode for Purcell enhancement.

An experimental micro-photoluminescence study of the complete mode structure of the

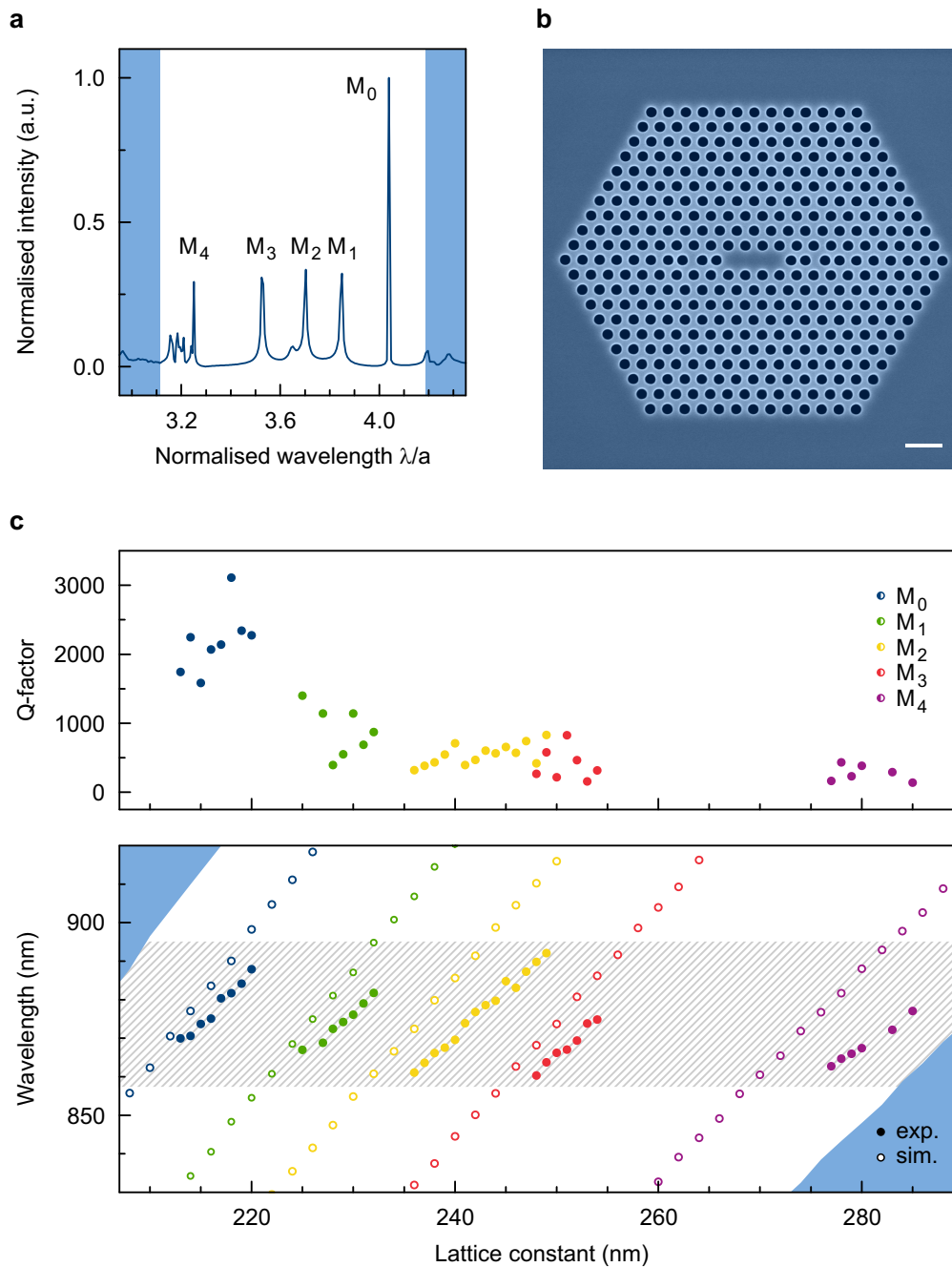


Figure 5.2 | Mode structure of the L3 defect cavity. **a**, Simulated mode structure of a L3 cavity with $\frac{r}{a} = 0.312$ and $\frac{d}{a} = 0.851$. **b**, A L3 cavity with the parameters from subfigure a. The scale bar corresponds to $0.5 \mu\text{m}$. **c**, Experimental study of the complete mode structure of the L3 cavity. The lower panel compares experimentally observed and simulated spectral positions of the different modes within the photonic band gap. The upper panel shows the corresponding experimentally observed Q -factors.

L3 defect cavity is presented in Figure 5.2 c. The wetting layer and the ensemble of medium-density quantum dots were used as an internal light source, emitting in a spectral range from approximately 860 nm to 895 nm (indicated by the hatched area in Fig. 5.2 c, lower panel). However, since the five modes of the L3 cavity span a spectral range of about 200 nm in the devices used here, it is not possible to observe all five modes simultaneously in one device with this technique. Therefore, the modes were spectrally tuned through the observable spectral window by fabricating a large number of L3 cavities with lattice constants ranging from 190 nm to 290 nm. The solid discs in the lower panel of Fig. 5.2 c represent the experimentally observed spectral position of the different modes as a function of the lattice constant, while the open circles show the spectral position of the modes according to finite-difference time-domain simulations with device parameters extracted from scanning electron micrographs (normalised hole radius of $\frac{r}{a} = 0.312$, constant nominal slab thickness of 200 nm). The generally reasonable agreement between experiment and simulation as well as the fact that all possible modes within the photonic band gap were observed systematically allow for an unambiguous assignment of the experimentally observed to the theoretically predicted modes $M_0 - M_4$. Despite earlier attempts [221, 222], this is the first time that the complete mode structure of the L3 defect cavity was observed experimentally.

The experimentally observed wavelengths tend to be slightly blueshifted with respect to the simulations for all modes, which has been shown to be attributable to local-field perturbations at the gallium arsenide–vacuum interface due to fabrication imperfections [223]. Notably, modes M_2 and M_4 are particularly affected, which suggests that the spectral position of these modes is more sensitive to these perturbations. The theoretically predicted inverse proportionality between the blueshift and the mode volume [223] cannot be responsible for this observation since the mode volumes of the modes M_2 and M_4 are the smallest and largest, respectively, among the five modes supported by the L3 defect cavity (see Table 5.1). However, the mode profiles presented in Fig. 5.3 show that in particular the electric field components of the modes M_2 and M_4 have their maxima just at gallium arsenide–vacuum interfaces, making them particularly sensitive to imperfection-induced local-field perturbations at these interfaces. The larger blueshifts for these modes are therefore attributable to their particular mode profiles rather than to their mode volumes.

The upper panel of Fig. 5.2 c shows the experimental Q -factors of the observed modes. As a general trend, experimental Q -factors decrease with increasing mode number from exceeding 3000 for mode M_0 to about 160 for mode M_4 . The comparison of the mean of the experimentally observed Q -factors with the simulated Q -factors for the ideal structures in Table 5.1 shows that for all modes, the experimentally achieved Q -factors are significantly lower than predicted theoretically. This is attributed to deviations from the ideal structural characteristics such as non-vertical [224] and rough [225] side walls, and size-, shape- and position disorder of the holes [125]. The mode volumes for the five modes supported by the

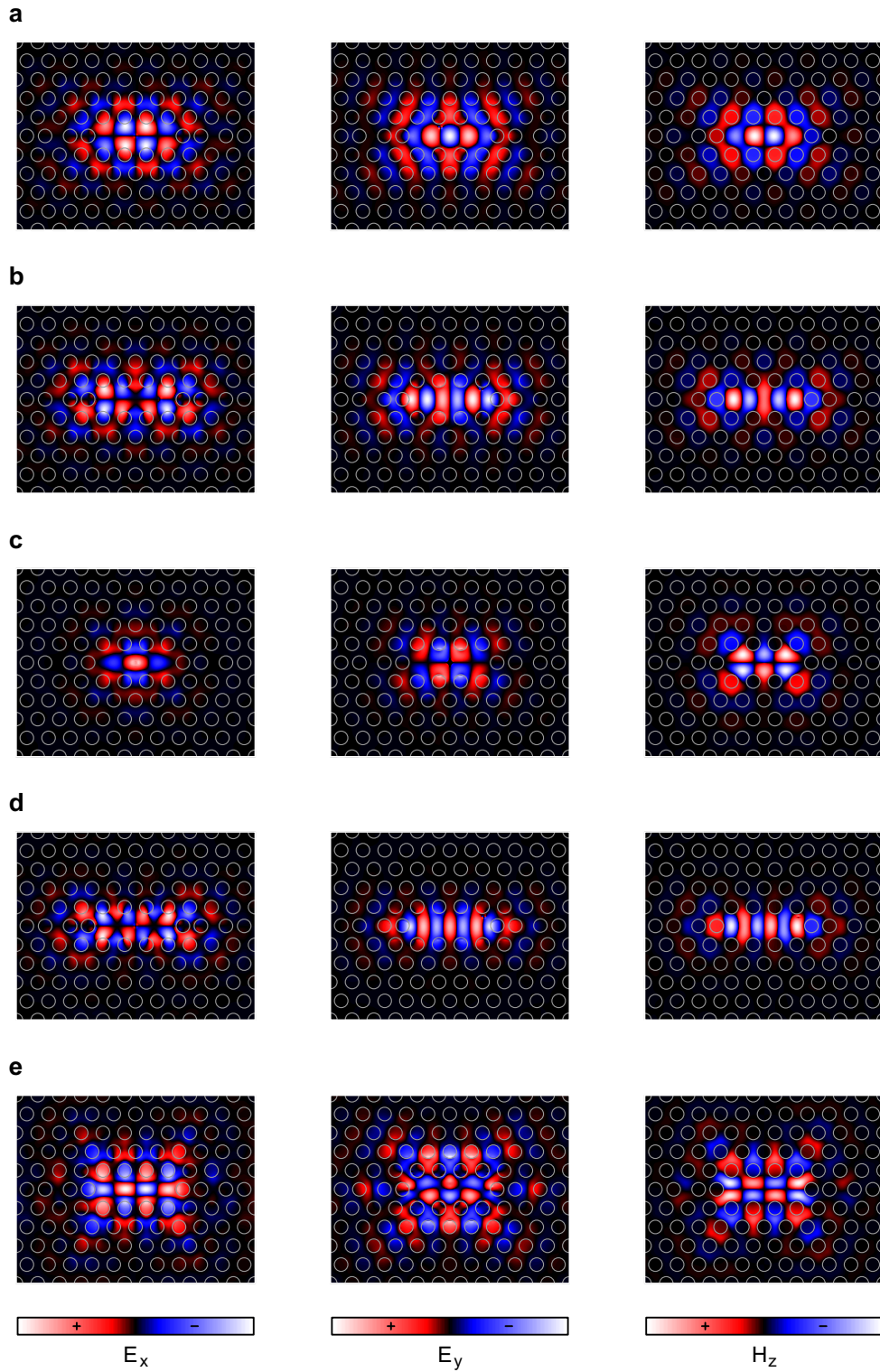


Figure 5.3 | Field profiles of the L3 defect cavity's modes. Left, centre, and right panels correspond to the E_x , E_y , and H_z field components, respectively. The structural parameters were $\frac{r}{a} = 0.312$ and $\frac{d}{a} = 0.851$ **a**, M_0 . **b**, M_1 . **c**, M_2 . **d**, M_3 . **e**, M_4 .

Mode	Q_{sim}	Q_{exp}	$V_m \left(\frac{\lambda^3}{n^3} \right)$
M_0	263 020	$2\,200 \pm 460$	0.81
M_1	2 510	890 ± 360	0.81
M_2	615	550 ± 150	0.72
M_3	1 030	400 ± 240	0.79
M_4	395	270 ± 120	1.11

Table 5.1 | Experimental and simulated characteristics of the modes of the L3 cavity.

Comparison of the simulated Q -factors (Q_{sim}) for the ideal structure, the mean of the experimentally observed Q -factors (Q_{exp} , with statistical standard deviation), and simulated mode volumes (V_m) in cubic wavelengths. The structural parameters for the simulations were $\frac{r}{a} = 0.312$ and $\frac{d}{a} = 0.851$.

L3 cavity are also given in Table 5.1, and are around 0.8 cubic wavelengths for all modes with the notable exception of mode M_4 , for which it is 1.11 cubic wavelengths.

In view of the previously discussed properties of the different modes supported by the L3 cavity, mode M_0 is particularly attractive for effective Purcell enhancement since it provides a low mode volume and simultaneously high Q -factors, both in theory and experiment.

Another important factor for a suitable mode for the Purcell enhancement of radiative transitions in quantum dots is the mode profile, which should exhibit the electric field maximum at the centre of the cavity, as far as possible from any gallium arsenide–vacuum interfaces. This is because surface defect states can be optically absorbing [211], which would limit experimentally attainable Q -factors. Furthermore, quantum dots need to be placed at the field maximum in order to obtain maximum Purcell enhancement. Since the proximity of quantum dots to gallium arsenide–vacuum interfaces degrades their optical properties [226, 227], modes with the field maximum close to such interfaces are not desirable. Due to the design used here for the in-plane extraction of single photons from the cavity (see Section 5.2), this requirement is of particular importance for the E_y field component. Figure 5.3 shows the simulated mode profiles of the five modes supported by the L3 defect cavity for the E_x , E_y , and H_z field components. The mode profile of the E_y field component of mode M_0 (Fig. 5.3 a, central panel) indeed exhibits a field maximum right at the centre of the cavity, making it well suited for the Purcell enhancement of transitions in quantum dots. The modes M_1 and M_3 could also be useful for this purpose from a mode profile point of view. Another notable feature is that the profiles of mode M_4 extend significantly further into the photonic crystal region than those of the remaining modes, reflecting the significantly larger mode volume discussed before.

In conclusion, mode M_0 has been identified in the previous discussion as the best suited mode of the L3 defect cavity for the Purcell enhancement of radiative transitions in quantum dots owing to large Q -factors, low mode volumes, and suitable mode profiles. The following subsection therefore discusses the optimised design parameters for this mode.

5.1.1 Optimisation of the design parameters for the M_0 mode of the L3 defect cavity

Figure 5.4 a illustrates the design parameters that are optimised in this subsection for the maximum Purcell factors achievable with the M_0 mode of the L3 defect cavity. The most basic structural parameters of a photonic crystal slab are the hole radius r and the slab thickness d . For the L3 defect cavity, it has been found that Q -factors can be increased significantly by shifting the lateral position of the nearest-neighbour holes [228]. This increase is attributed to phase-matching of the partial Bragg reflections at the photonic crystal mirrors by smoothing the envelope function of the electric field profile at the cavity edges [112], or alternatively by transverse mode-matching at the cavity edge [229, 230]. The corresponding shifts are denoted A , B , and C for the first, second and third nearest-neighbour holes, respectively. All parameters discussed in this subsection are normalised to the photonic crystal periodicity a .

Figure 5.4 b (upper panel) shows that the Q -factor peaks at a normalised hole radius $\frac{r}{a} = 0.315$, while the mode volume stays virtually constant across the range presented here. At the largest hole radius, the mode volume increases sharply, though, since the mode spectrally shifts out of the photonic band gap. For the maximum Purcell factor (lower panel), the ideal hole radius is $\frac{r}{a} = 0.315$.

As a general trend, both the Q -factor and the mode volume increase with increasing slab thickness (Fig. 5.4 c, upper panel). This behaviour is very similar to that observed for the slow-light mode studied in the previous chapter (see Fig. 4.4 b). As a result, the Purcell factor is not very sensitive to the slab thickness in the range studied here (Fig. 5.4 c, lower panel) since it is proportional to the ratio of Q -factor and mode volume. The maximum value is obtained for a normalised slab thickness of $\frac{d}{a} = 0.855$.

The mode volume is found to be relatively sensitive to the shift A of the first hole (Fig. 5.4 d, upper panel), a finding that can be understood intuitively as the cavity physically increases in size as the first hole is shifted away from the cavity center. However, the corresponding Q -factor peaks sharply at a first hole shift of $\frac{A}{a} = 0.18$, dominating the resulting Purcell factor (lower panel), which attains its maximum for the same first hole shift.

While shifting the second and third holes (Figs. 5.4 e and f) affects the Q -factors substantially, it does not change the mode volumes significantly. The ideal Purcell factors were found for shifts of $\frac{B}{a} = 0.01$ and $\frac{C}{a} = 0.16$.

In conclusion, the ideal parameters for the M_0 mode of the L3 cavity were found to be a hole radius of $r = 0.315a$, a slab thickness of $d = 0.855a$, and first, second, and third hole shifts of

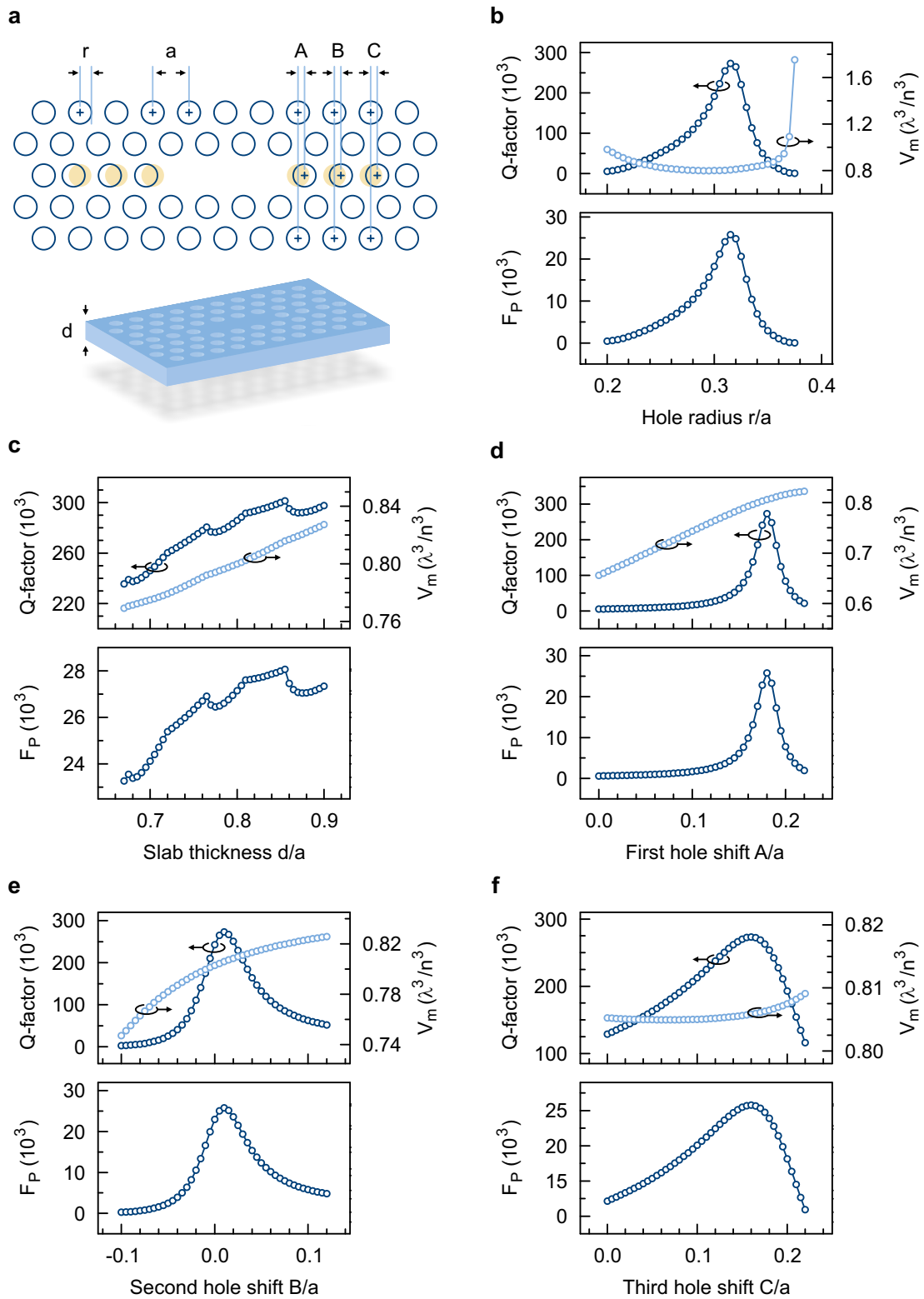


Figure 5.4 | Optimisation scans for the M_0 mode of the L3 defect cavity. a, Illustration of device parameters. **b-f**, Optimisation scans of the individual parameters.

$A = 0.18a$, $B = 0.01a$, and $C = 0.16a$, respectively. The resulting cavity is characterised by a M_0 mode with a Q -factor of 273 000 and a mode volume of 0.81 cubic wavelengths, which gives a maximum Purcell factor of 28 800 for an ideally positioned emitter.

5.2 Coupling of the L3 defect cavity to a waveguide

The discussion of the complete mode structure of the L3 defect cavity in the previous section concluded that the mode M_0 was the most attractive mode for Purcell enhancement owing to the high Q/V_m -ratio and the suitable mode profile. In order to direct the emission of single photons from a quantum dot in the L3 cavity into the chip plane to allow for integration with quantum photonic circuits, it is necessary to couple it to a propagating mode in a photonic crystal waveguide. This coupling is the subject of this section.

5.2.1 Fundamental requirements for cavity – waveguide coupling

A fundamental requirement for the coupling of a cavity mode to a waveguide is the existence of a guided mode in the waveguide at the resonant frequency given by the cavity. The left panel in Fig. 5.5 a shows the dispersion relation of a W1 waveguide in the hexagonal lattice of a two-dimensional photonic crystal slab, as simulated with the plane wave expansion technique. Within the photonic band gap and below the light cone, a number of guided modes is present. The right panel in Fig 5.5 a shows the mode structure of an L3 defect cavity in a photonic crystal slab characterised by the same structural parameters. The position of the nearest neighbour holes of the cavity was adjusted as discussed in the previous section to allow for the highest Q/V_m -ratio for mode M_0 . The y -scales of the plots in both panels of Fig. 5.5 a are identical, and the red dashed lines serve as guides to the eye, indicating that a simple W1 waveguide exhibits a guided mode at the frequency of the mode M_0 of the L3 defect cavity. Please note that at this frequency, the corresponding guided mode in the W1 exhibits a relatively low dispersion $\frac{\partial\omega}{\partial k}$, or equivalently a low group velocity. This improves the coupling between a cavity and a waveguide mode due to a longer interaction time [231], but it also increases losses in the photonic crystal waveguide due to optical scattering, which scale inversely with the group velocity [232]. For future designs of larger photonic circuits with photonic crystal waveguides, it would therefore be advantageous to optimise the dispersion in different parts of the waveguide by tailoring the design of the waveguide [127, 233]. Since only a short portion of a waveguide was used in the devices studied here, however, dispersion optimisation of the waveguide was not required.

As an aside, please note that the plane wave expansion simulation shown in Fig. 5.5 a (left panel) reveal that at the frequency of mode M_4 , the photonic band gap does not extend to all k -vectors below the light line. This results in less effective confinement of this mode and explains the comparatively large mode volume and the extension of the fields well into the

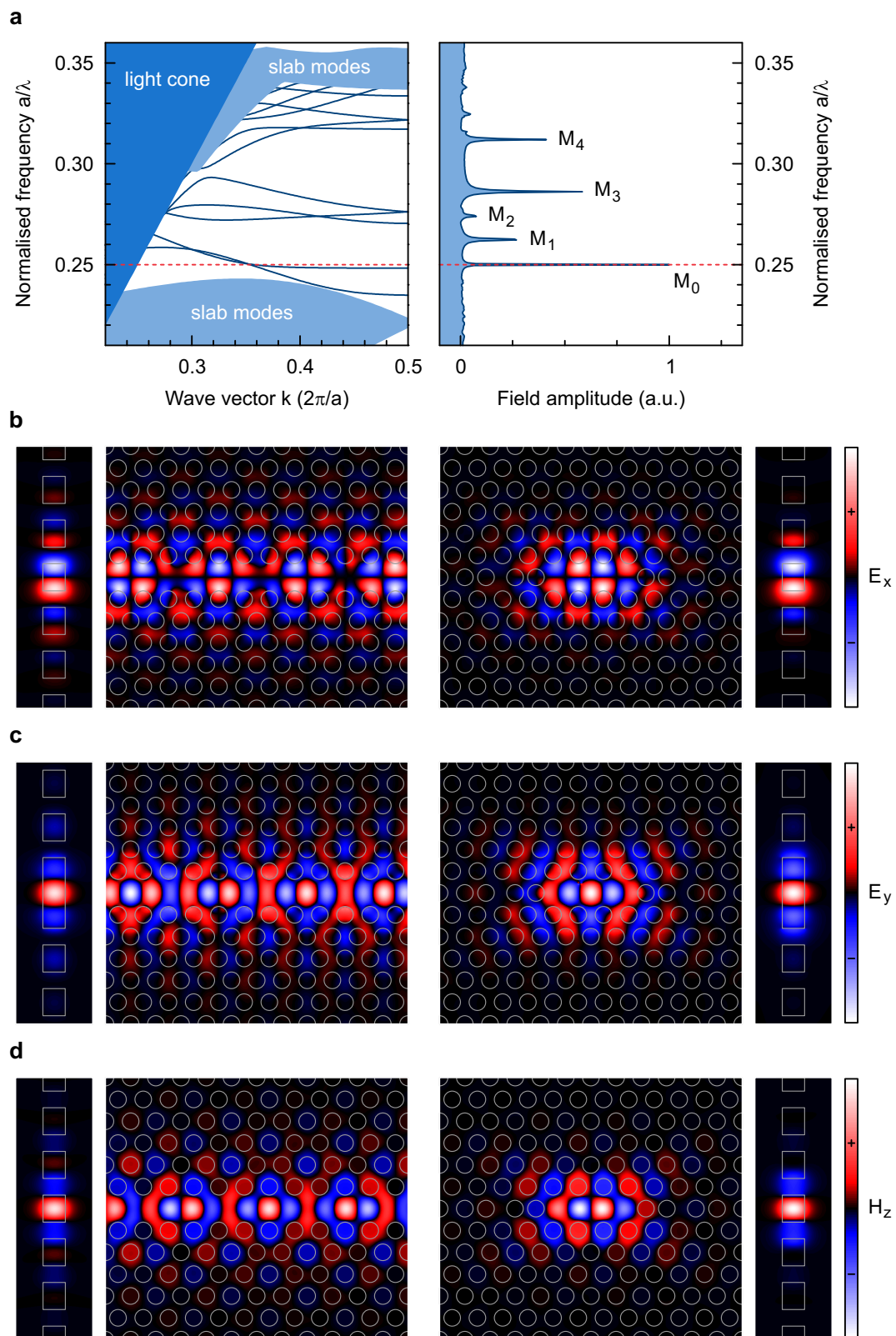


Figure 5.5 | Fundamental considerations for L3 cavity – waveguide coupling. **a**, Band diagram and mode structure. **b-d**, Mode profiles of the E_x , E_y , and H_z fields.

photonic crystal for the M_4 mode, which was discussed in the previous section.

In order to obtain efficient coupling between the cavity and the waveguide modes, a good matching between their field patterns and their parities is required [231]. Figures 5.5 b - d show the modes' field patterns at the frequency given by the mode M_0 of the L3 cavity for the E_x , E_y , and H_z fields, respectively. The right panels show the mode profiles in an optimised L3 defect cavity, and the left panels those for a W1 waveguide in a photonic crystal slab characterised by the same parameters. The corresponding field patterns exhibit not only the same parities, but indeed very similar field patterns. This striking similarity can be understood if the L3 defect cavity is viewed as Fabry-Perot resonator in a short W1 waveguide terminated at both ends with matched photonic crystal mirrors [230]. In terms of field patterns and their parity, the M_0 mode of the L3 cavity and the corresponding W1 waveguide mode are hence ideally suited for coupling.

5.2.2 Cavity – waveguide separation

For evanescent coupling [28, 231], the L3 defect cavity and the W1 waveguide are brought into proximity, separated only by a few unit cells of the photonic crystal lattice. To this end, different geometries have been studied experimentally, including side-coupling the L3 cavity to the waveguide [234, 235] or tilting the L3 cavity by 60° with respect to the waveguide axis [236]. For the sake of simplicity and in order to obtain efficient coupling to a unidirectional waveguide [28], devices with a straight cavity configuration are studied here, in which the L3 cavity and the W1 waveguide share the same axis (see Fig. 5.1). Figure 5.6 a shows the simulated Q -factor of the mode M_0 of the L3 cavity as a function of cavity – waveguide separation. As expected, the Q -factor of the cavity mode decreases as the waveguide is brought into close proximity due to the coupling to and energy transfer into the waveguide. The resulting Q -factor of the coupled cavity, Q_{cpl} , relates to the Q -factor of the uncoupled cavity, Q_{cav} , as [236]

$$\frac{1}{Q_{\text{cpl}}} = \frac{1}{Q_{\text{cav}}} + \Gamma, \quad (5.1)$$

where Γ is the coupling strength, which is proportional to the decay rate of the cavity field into the waveguide. Figure 5.6 a shows the corresponding coupling strength Γ as a function of the cavity – waveguide separation. For separations of four or more unit cells, or holes, the coupling strength is negligible, but it increases strongly for three, two, and one holes. For an efficient on-chip single photon source with strong Purcell enhancement, there is therefore a trade-off between high Q -factors of the coupled cavity mode and efficient coupling of single photons into the waveguide. Since Q_{cpl} for a separation of one unit cell is very low even for the ideal structure simulated here, and Γ becomes negligible for separations exceeding three unit cells, only devices with cavity – waveguide separations of two and three unit cells were fabricated for experimental study (Figs. 5.6 c and d).

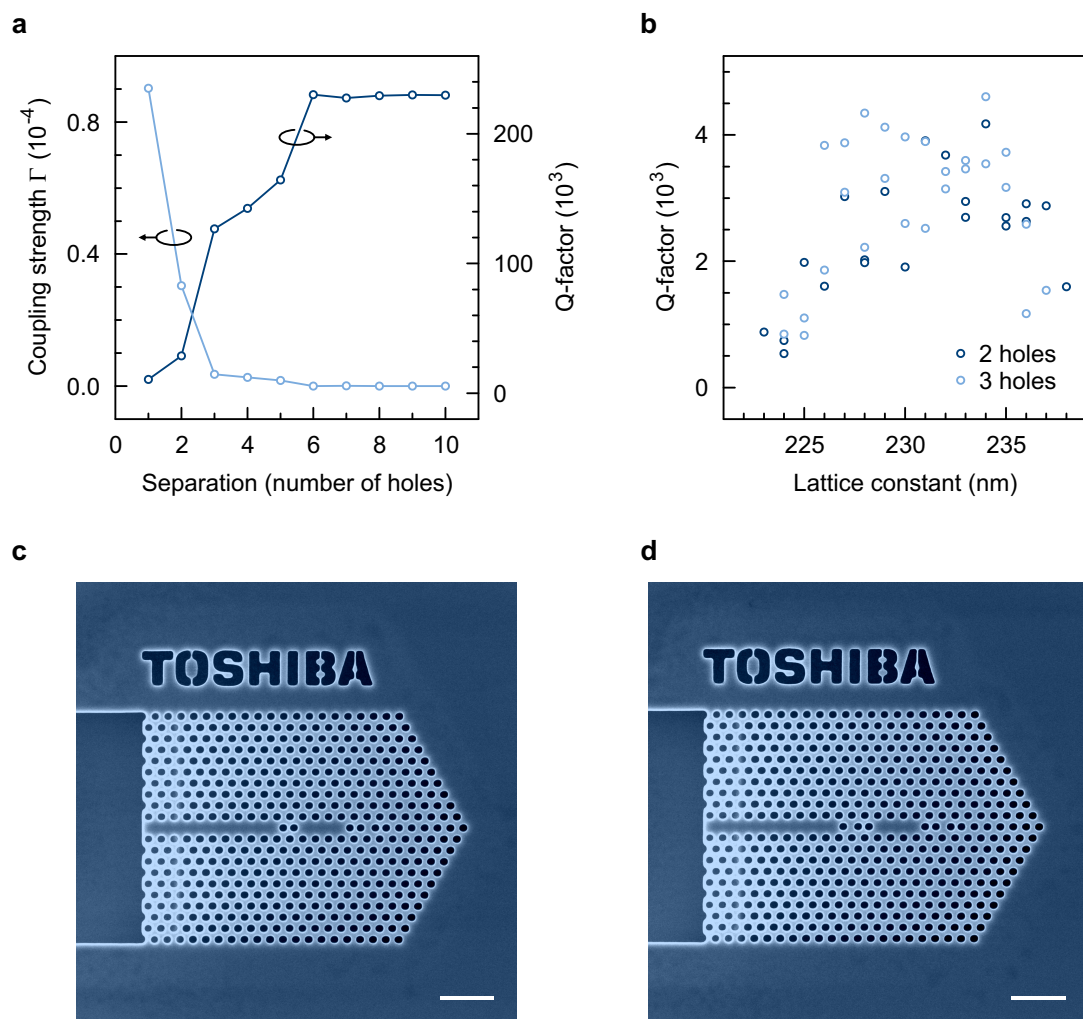


Figure 5.6 | Coupling strength and cavity–waveguide separation. **a**, Coupled Q -factor of the M_0 mode of the L3 cavity and corresponding coupling strength as a function of the cavity–waveguide separation. **b**, Experimental Q -factors of the fundamental mode of waveguide–coupled L3 cavities observed in-plane for cavity–waveguide separations of two and three holes. **c** and **d**, Scanning electron micrograph of L3 cavities separated by two and three holes from a waveguide, respectively. The scale bars correspond to $1\ \mu\text{m}$.

Similar to the experiments with stand-alone L3 defect cavities described in Section 5.1, devices with a small range of lattice constants were fabricated such that the expected spectral position of the mode M_0 of the coupled L3 cavity covers the emission range of the wetting layer and medium-density quantum dots. These were used as internal light sources for photoluminescence experiments, in which the samples were excited optically from the top, and the in-plane emission was collected at the exit of the waveguide. Unfortunately, this tech-

nique does not allow for a direct study of the coupling strength since the detected emission intensities vary strongly from device to device due to the random nucleation of quantum dots. However, the Q -factors of the M_0 mode of the coupled L3 cavity could be extracted from the recorded spectra by Lorentzian fitting.

Figure 5.6 b compares the experimentally observed Q -factors for devices with cavity – waveguide separations of two and three holes, but otherwise nominally identical structural parameters (the small differences in the normalised slab thickness for different lattice constants are negligible here). While Q -factors generally scatter around 3000 for the sets of devices studied here, devices with lattice constants below 226 nm exhibit markedly lower Q -factors. This behaviour is attributed to the spectral overlap of the mode M_0 with the wetting layer for these lattice constants, which results in a degradation of Q -factors due to increased absorption in the slab material [125]. Ignoring these devices, the mean Q -factor is found to be 2720 ± 750 for devices with a cavity – waveguide separation of two holes and 3200 ± 890 for those with a separation of three holes. The mean values therefore represent to a limited extent the decrease in coupled cavity Q -factors with decreasing cavity – waveguide separation that is predicted by the simulated results shown in Fig. 5.6 a. However, the substantial deviation of the experimentally observed from the simulated Q_{cpl} , in particular for the devices with three hole separations, suggests that these Q -factors are not limited by radiation losses into the waveguide but rather by systematic fabrication imperfections. Moreover, experimentally observed Q -factors exhibit considerable scatter for both types of devices, which in turn is attributed to random fabrication imperfections. In view of this scatter, and since the lower coupling strength Γ for devices with a cavity – waveguide separation of three holes is not accompanied by drastically higher Q -factors as theoretically expected, the device design with a separation of two holes is preferable with current fabrication techniques. The remainder of this chapter will therefore focus on this type of devices.

Figures 5.7 a - c show the mode profiles of a complete waveguide-coupled L3 defect cavity with a cavity – waveguide separation of two holes for the E_x , E_y , and H_z field components. The mode profiles closely resemble those for the individual component of the device presented in Figs. 5.5 b - d, but the relative field intensities in the cavity and waveguide areas show that light is confined much more strongly in the cavity area, and only slowly leaks into the waveguide area, resulting in a relatively lower field intensity in the waveguide area.

With the experience from previous sample fabrication runs fed back into the mask design in order to obtain structural parameters even closer to the optimised ones discussed in Subsection 5.1.1, another set of waveguide – coupled L3 defect cavities was processed in order to achieve higher Q -factors. The result of the in-plane photoluminescence study of this set of devices is shown in Fig. 5.8 a. The mode M_0 of the waveguide – coupled L3 defect cavity was systematically observed in a wavelength range from about 870 nm to 900 nm for devices with lattice constants ranging from 222 nm to 233 nm. Small deviations from the quasi-linear

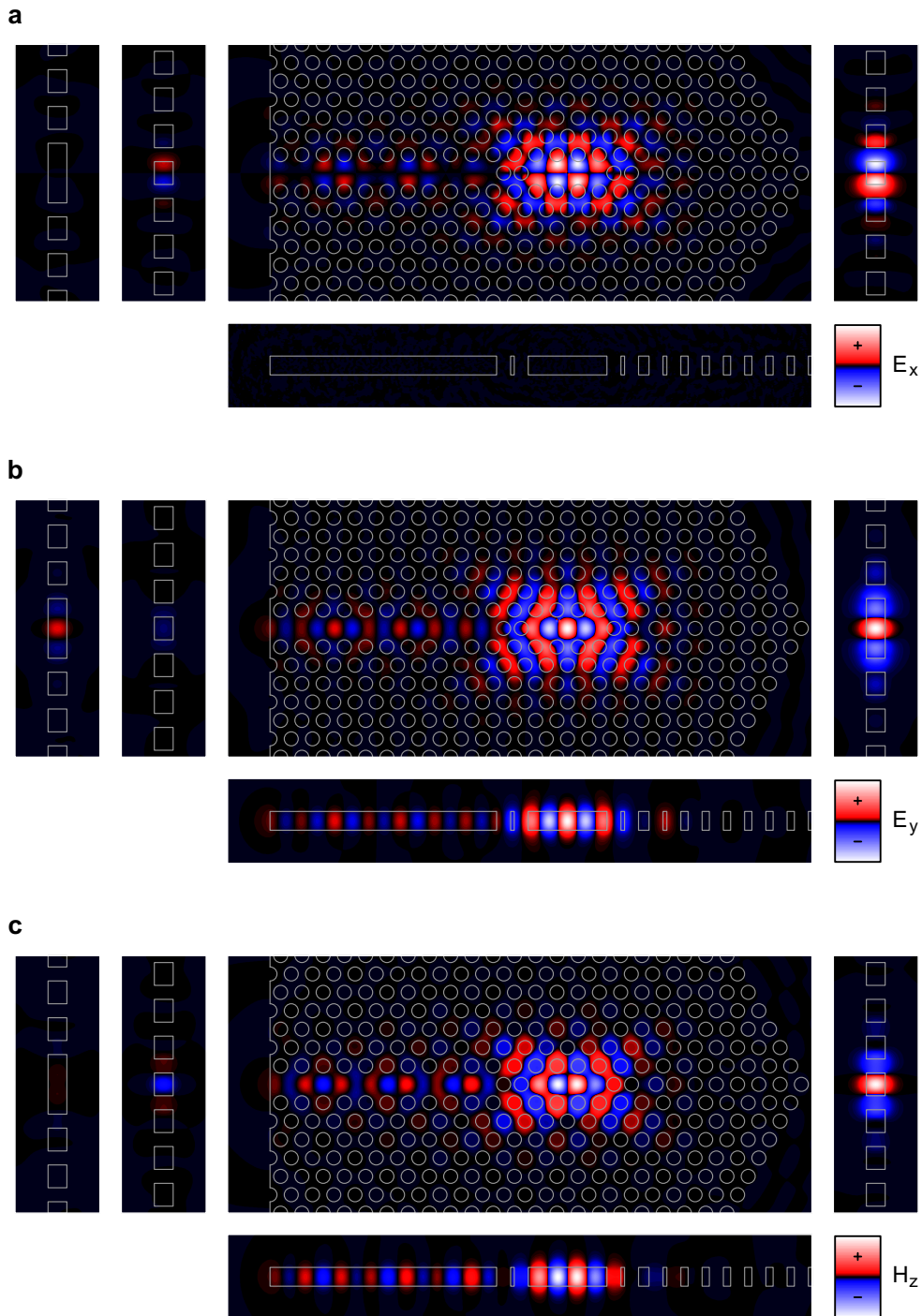


Figure 5.7 | Mode profiles of a waveguide-coupled L3 cavity. The central panels show a top view of the device at the centre of the slab, and the remaining panels show cross-sectional views in between nearest neighbour holes of the waveguide (far left), through nearest neighbour holes of the waveguide (left), through the field maximum in the L3 cavity (right), and along the axis of the cavity and waveguide (bottom). The photonic crystal slab is characterised by $\frac{r}{a} = 0.329$ and $\frac{d}{a} = 0.885$. **a**, E_x field. **b**, E_y field. **c**, H_z field.

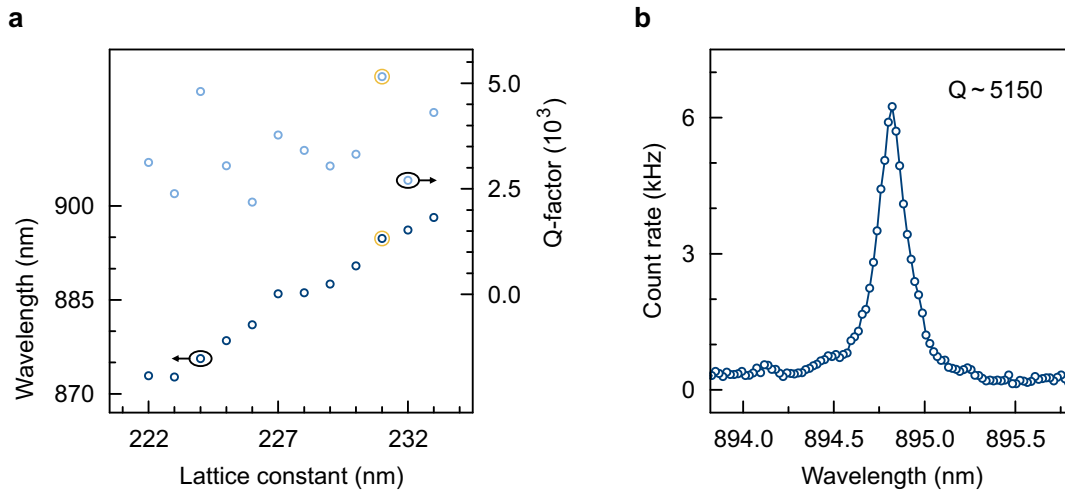


Figure 5.8 | High- Q waveguide-coupled L3 defect cavities. **a**, Experimental Q -factors and spectral position of the M_0 mode of waveguide-coupled L3 cavities as observed in in-plane experiments. **b**, Record Q -factor of the fundamental mode of 5150 for the device with a lattice constant of 231 nm (marked with yellow circles in a).

trend of increasing cavity mode wavelength with increasing lattice constants are attributed to random fabrication imperfections. This systematic and reproducible in-plane observation of the coupled L3 cavity mode M_0 nevertheless makes this device design a promising candidate for the scaling to larger numbers of devices with very similar properties. The corresponding Q -factors, also shown in Fig. 5.8 a, have increased compared to the previous set of devices, with a mean of 3440 ± 920 , significantly larger than mean values for sets of similar devices reported previously (in out-of-plane and indirect in-plane experiments) [236, 237]. The device with a lattice constant of 231 nm (the corresponding data points are marked with a yellow circle in Fig. 5.8 a, spectrum shown in Fig. 5.8 b) exhibits a Q -factor of 5150, exceeding the previously highest reported value on an individual device of this kind [237].

5.3 On-chip single photon emission from a quantum dot in a waveguide-coupled L3 defect cavity

In the previous sections of this chapter, the complete mode structure of the L3 defect cavity, the optimisation of the M_0 mode of this type of cavity and its coupling to a W1 waveguide for on-chip extraction of light from the cavity was discussed. The resulting, optimised design for a waveguide-coupled L3 cavity is used in this section to demonstrate on-chip single photon emission with such a structure.

Figure 5.9 a shows a device similar to the one studied and discussed in this section. The lattice constant of the device studied here is $a = 226$ nm, resulting in a normalised slab thick-

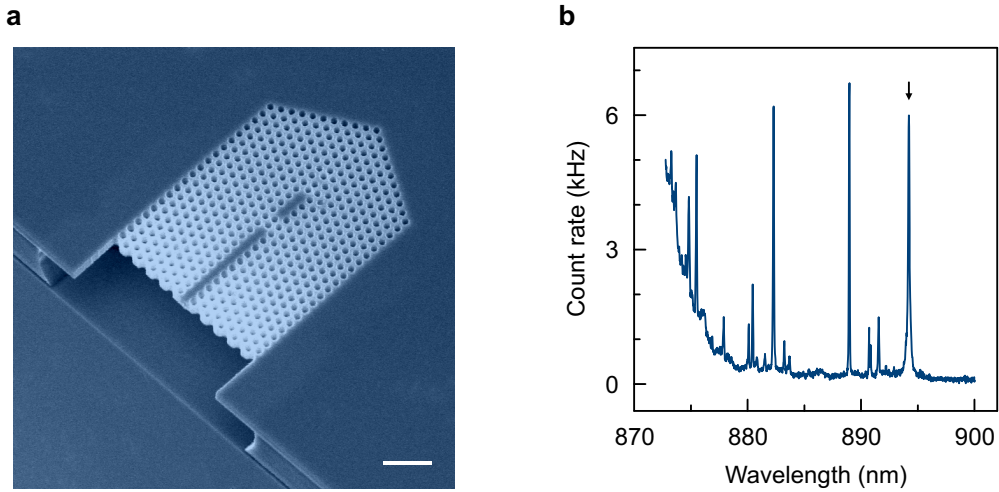


Figure 5.9 | In-plane emission of a waveguide–coupled L3 cavity. **a**, Oblique view of a device similar to the one discussed in this section. The scale bar corresponds to $1 \mu\text{m}$. **b**, In-plane emission spectrum of the L3–waveguide single photon source. The wetting layer extends to about 880 nm, while the transition of interest is marked with an arrow at 894.2 nm. This spectrum was recorded at $T = 5 \text{ K}$ and under pulsed excitation with $P_{\text{ex}} = 0.34 \mu\text{W}$.

ness of $\frac{d}{a} = \frac{200 \text{ nm}}{226 \text{ nm}} = 0.885$. The analysis of scanning electron micrographs of nominally identical devices from the same chip revealed a normalised hole radius of $\frac{r}{a} = 0.329$, reasonably close to the optimised value found in Subsection 5.1.1. Please note that Figs. 5.1 and 5.5 - 5.7 were prepared for these structural parameters and can be referred to for comparison. The spectrum of the in-plane emission is shown in Fig. 5.9 b, and exhibits emission from the wetting layer that extends to about 880 nm, similar to the in-plane emission spectrum of the slow-light enhanced device studied in the previous chapter (see Fig. 4.6 a). However, the spectrum of the waveguide–coupled L3 cavity comprises a larger number of transitions stemming from different quantum dots, which is a result of a comparatively higher quantum dot density in this sample. This is required to maintain a reasonable yield of promising devices as the mode volume of the M_0 mode in the L3 cavity is significantly smaller than that of the slow-light mode studied in the previous chapter. The transition of interest, which will be studied in the remainder of this section, is marked with an arrow in Fig. 5.9 b at 894.2 nm.

Figure 5.10 a shows the evolution of this part of the spectrum with increasing temperature from $T = 5 \text{ K}$ to $T = 37 \text{ K}$. While the transition is approximately in resonance with the mode M_0 in a temperature range from 5 K to 30 K, it clearly tunes out of resonance for higher temperatures. The spectral location of the experimentally observed M_0 mode at about 894.2 nm is in reasonable agreement with the corresponding simulation, which predicts the mode to be at a wavelength of 904.8 nm for these structural parameters. The deviation is comparable

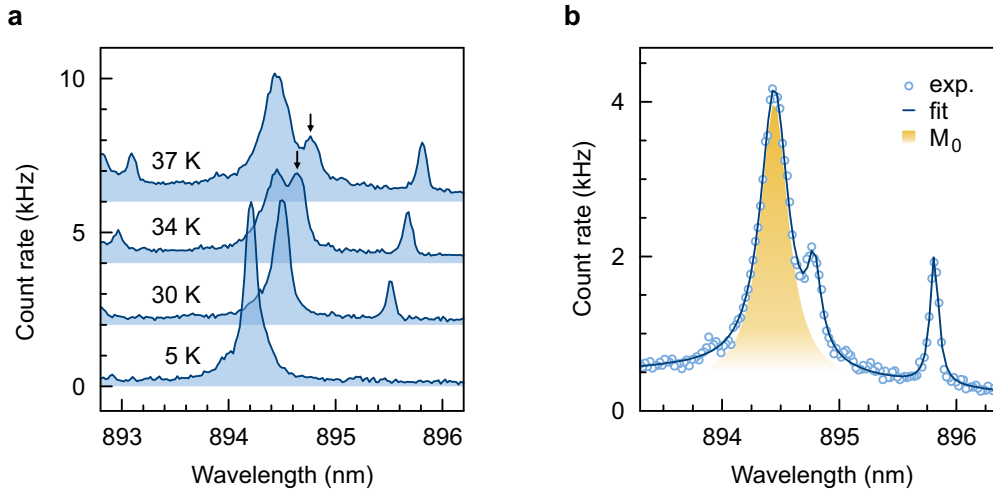


Figure 5.10 | Coupling of the quantum dot transition to the L3 cavity mode. The spectra were recorded under pulsed excitation with $P_{\text{ex}} = 0.34 \mu\text{W}$. **a**, Temperature dependence of the spectrum for temperatures ranging from 5 K to 37 K. While the transition is approximately in resonance for the temperature range from 5 K to 30 K, it tunes out of resonance at higher temperatures (transition marked with an arrow). **b**, Fitting of the spectrum at $T = 37 \text{ K}$ shows a Q -factor of 3100 for the M_0 mode of the L3 cavity (highlighted in yellow).

to those observed in the discussion of the stand-alone L3 defect cavity in Section 5.1, and equally attributed to local-field perturbations at the gallium arsenide–vacuum interface due to fabrication imperfections [223]. A Lorentzian fit of the spectrum at $T = 37 \text{ K}$ in Fig. 5.10 b reveals a Q -factor of 3100 for the mode M_0 (highlighted in yellow), about one order of magnitude lower than predicted by simulations for this device. The deviation is attributed to structural deviations from the ideal values.

The time-resolved photoluminescence signal of the transition at temperatures $T = 30 \text{ K}$, 34 K and 37 K is shown in Fig. 5.11 a. Off-resonance, at $T = 37 \text{ K}$, the lifetime was found to be $\tau = 2.4 \text{ ns}$. While this is relatively long for an excitonic transition, it is still within the scatter range typically observed experimentally. At lower temperatures, as the transition tunes into resonance with the mode of the L3 defect cavity, the lifetime decreases to 1.7 ns and 1.4 ns for $T = 34 \text{ K}$ and $T = 30 \text{ K}$, respectively. This decrease is attributed to Purcell enhancement of the radiative recombination of the exciton state in the quantum dot due to coupling to the M_0 mode of the L3 cavity. The corresponding Purcell factor of 1.7 compares favourably with the measured Purcell factor of the slow-light enhanced device discussed in the previous chapter. However, the maximum Purcell factor for the M_0 with the experimentally observed Q -factor of 3100 is 292. This considerable deviation is attributed to poor spatial overlap of the quantum dot position with the field maximum of the M_0 mode at the centre of the cavity and

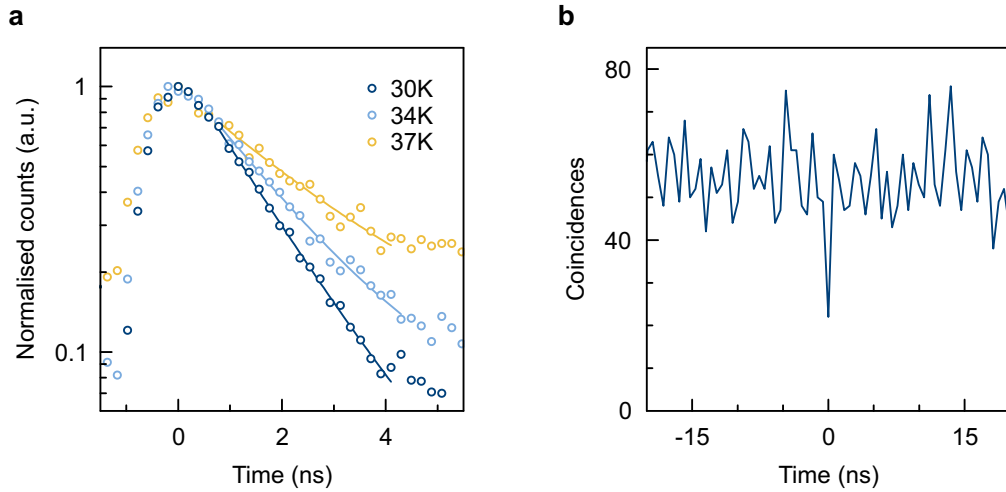


Figure 5.11 | Purcell enhancement and on-chip single photon emission. The signals were recorded for the exciton transition. **a**, Time-resolved photoluminescence measurements at $T = 30$ K, 34 K, and 37 K reveal exciton lifetimes of 1.4 ns, 1.7 ns and 2.4 ns, respectively. The measurements were taken under pulsed excitation with $P_{\text{ex}} = 0.34 \mu\text{W}$. **b**, Autocorrelation measurements in a Hanbury Brown and Twiss interferometer show clear anti-bunching with $g^{(2)}(0) = 0.4 \pm 0.15$, confirming on-chip single photon emission from a waveguide-coupled L3 cavity. This measurement was taken at $T = 5$ K and under continuous-wave excitation with and $P_{\text{ex}} = 2.2 \mu\text{W}$.

highlights the importance of growing site-controlled quantum dots, which would not only provide true scalability, but also help to more effectively harness the potential for Purcell enhancement of the device structure discussed in this chapter.

Finally, the photon statistics of the transition at $T = 5$ K, i.e. in resonance with the M_0 mode, was studied with a Hanbury Brown and Twiss experiment. The coincidence histogram shown in Fig. 5.11 b exhibits a pronounced dip at $\tau = 0$ ns. For non-zero delay, 55 coincidences were recorded on average with a standard deviation of eight counts, whereas at the dip at zero delay, only 22 coincidences were observed. From this data, $g^{(2)}(0) = 0.40 \pm 0.15$ can be inferred, which is a significant improvement over previous studies [237] and represents the first demonstration of on-chip single photon emission from a waveguide-coupled L3 defect cavity. The deviation from a perfect single photon source ($g^{(2)}(0) = 0$) is mainly attributed to far off-resonant coupling of emission into the cavity mode [238–243]. Resonant excitation schemes have been shown to suppress this far off-resonant coupling and to lead to essentially background-free single photon emission [244]. Another factor to take into account is the relatively large time bin-size in this autocorrelation measurement, which could mask a potentially lower dip. Unfortunately, the limited detected count rate led to prohibitively long

accumulation times for statistically significant autocorrelations with smaller time bins.

In conclusion, an in-depth discussion and experimental study of the complete mode structure of the L3 defect cavity was presented in this chapter. The entire mode structure was observed experimentally for the first time, with a reasonable agreement between experiment and the accompanying simulations. The mode M_0 was identified to be attractive for the Purcell enhancement of the radiative recombination of excitonic states in quantum dots, and optimised structural parameters for this mode were identified. This mode was furthermore shown to be well suited for the coupling to a W1 waveguide for on-chip light extraction. This coupling was first studied with finite-difference time-domain simulations, and the most promising configurations were studied experimentally. The design with a cavity – waveguide separation of two holes was found to be preferable with current fabrication techniques, and record Q -factors for this type of device were demonstrated both for the mean value of a set of devices and for an individual device. Finally, Purcell-enhanced on-chip single photon emission was for the first time demonstrated for a waveguide – coupled L3 defect cavity.

6 Electrically controllable on-chip single photon sources

The integrable quantum light sources presented in the previous chapters emitted single photons at wavelengths of 893.7 nm for the slow-light enhanced source in Chapter 4 and at 894.2 nm for the waveguide-coupled L3 cavity in Chapter 5. The difference in emission wavelengths highlights an important challenge for the use of distinct self-assembled quantum dots as single photon sources in quantum information processing, since the most promising schemes rely on two-photon interference [11]. This process, however, requires photons with identical wavelengths [24], which contrasts with the randomly distributed size and hence emission wavelength of quantum dots. True scalability will therefore require the ability to independently tune the emission wavelengths of individual quantum dots in order to obtain a set of quantum light sources that emit single photons at identical wavelengths.

The most common technique used to tune the emission wavelength of quantum dots is thermo-optical tuning, in which the temperature of the sample is changed either globally [63] or locally [245], which leads to a modification of the band gap of the quantum dot and its environment and therefore to a change in the emission wavelength. Thermo-optical tuning, however, is not completely satisfactory as it is a slow process and leads to acoustic phonon broadening at increased temperatures [91]. Electro-optical tuning by exploiting the quantum-confined Stark effect has been demonstrated as a fast and readily scalable alternative [246], and unparalleled tuning ranges have been demonstrated with this technique for the out-of-plane emission of quantum dots [89].

The aim of this chapter is therefore to combine the electro-optical tuning of the single photon emission wavelengths of quantum dots with a photonic crystal device structure that is integrable with planar light circuits. Figure 6.1 illustrates the corresponding device concept. As in the previous chapters, an indium arsenide quantum dot embedded at the centre of a gallium arsenide slab is optically excited from the top and used to generate single photons. In order to allow for the electric manipulation of the band structure of the quantum dot and its environment and hence for the exploitation of the quantum-confined Stark effect, the gallium arsenide slab comprises a vertical PIN structure, as shown in the inset of Fig. 6.1. The *p*- and *n*-doped layers of this PIN structure are independently contacted electrically. For the in-plane extraction of the electrically controlled single photon emission of the quantum dot, the corresponding transition is coupled to a propagating mode in a unidirectional waveguide.

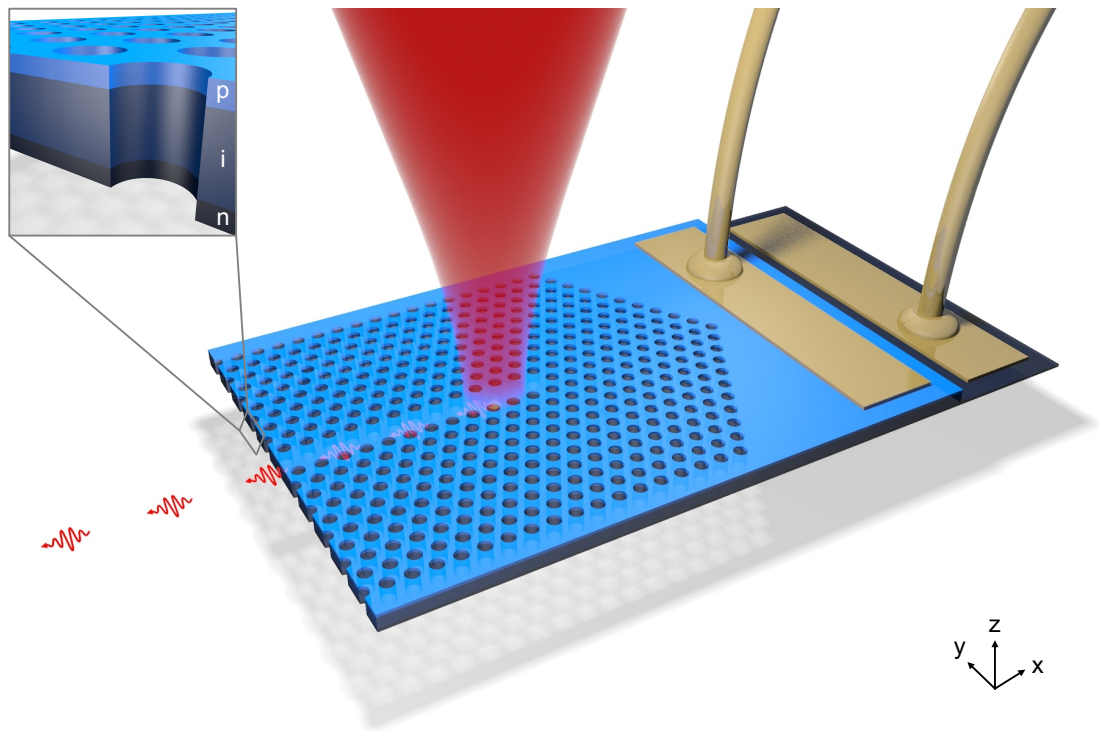


Figure 6.1 | Device concept for an electrically controllable on-chip single photon source. The quantum dot is embedded in an electrically contacted PIN diode in order to modify its electronic band structure. Following the optical excitation of the quantum dot with a focussed laser beam from the top (red cone), single photons (shown as wavepackets) are emitted into a photonic crystal waveguide.

uide formed by the omission of holes along a half-line in a two-dimensional photonic crystal in the gallium arsenide slab.

The first section of this chapter is dedicated to a brief theoretical discussion of the quantum-confined Stark effect that is exploited in the device to electrically control the emission wavelength of the quantum dot. This is followed by a section describing in more detail the device design and the additional nanofabrication steps that were required in order to realise the device. Finally, in the third section, the experimental demonstration of electrically controllable in-plane single photon emission from two different devices is presented.

6.1 Quantum-confined Stark effect

As described in more detail in Section 2.1, the excellent single photon emission properties of semiconductor quantum dots stem from the discrete electronic states resulting from the three-dimensional carrier confinement in the quantum dot. Figure 6.2 a shows a schematic of the electronic states in a quantum dot, which here are populated by one electron and one

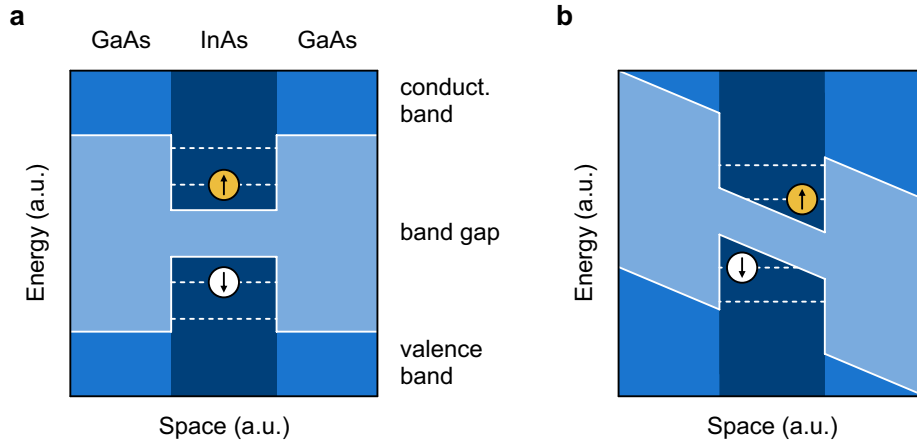


Figure 6.2 | Illustration of the quantum-confined Stark effect. **a**, Schematic of the electronic band diagram of the immediate environment of the quantum dot at zero effective electric field (flat band). **b**, Same, but for a non-zero effective field. The transition energy of the exciton state is decreased compared to the flat band configuration.

hole, forming the excitonic state. The wavelength of the single photon that is emitted upon radiative recombination of this excitonic state is defined by the energy separation between the least energetic electron and hole states and the excitonic binding energy. The application of an external electric field to a quantum dot structure leads to a manipulation of the band structure as illustrated in Fig. 6.2 b. While the charge carriers forming the exciton are still confined to the quantum dot due to the band gap difference between the indium arsenide in the dot and the surrounding gallium arsenide matrix, the energy level separation between the electron and hole states decreases as a result of the band bending induced by the external electric field. This change of the transition energy with external electric field is called the quantum-confined Stark effect and was first observed experimentally in semiconductor quantum well structures in 1984 [247]. The shift in transition energy ΔE as a function of the external field F is described by [248, 249]

$$\Delta E = pF + \beta F^2, \quad (6.1)$$

where the linear term arises from the non-zero permanent electric dipole moment p , and the quadratic term from the quantum-confined Stark effect with the polarisability β .

The possibility to exploit the quantum-confined Stark effect to conveniently tune the emission wavelength of quantum dots by applying an external electric field has been demonstrated experimentally [89, 246, 248]. It has been employed successfully in cavity quantum electrodynamic experiments with quantum dots [88], and its enormous potential for quantum information processing has been demonstrated by tuning remote quantum dots into

resonance for two-photon interference [90]. All these demonstrations, however, relied on vertical light emission, which does not lend itself to the planar integration with quantum photonic circuits. The device design used here to realise an electrically tunable in-plane single photon source will be described in the following section.

6.2 Device design and nanofabrication

In order to obtain in-plane emission from the quantum dot, it is embedded in a two-dimensional photonic crystal slab similar to the ones used in the previous chapters. For the application of an external electric field to the quantum dot and its environment, however, a wafer with a different layer structure as illustrated in Fig. 6.3 a is required. Similarly to the previously used wafers, the 200 nm thick slab is grown on top of a 900 nm sacrificial layer of aluminium gallium arsenide with an aluminium composition of 75%. In order to apply a homogeneous external electric field in a controlled manner, the slab comprises a PIN diode structure. To this end, both the entire sacrificial layer and the bottom 42 nm of the slab are *n*-doped with silicon atoms at a doping level of $2 \times 10^{18} \text{ cm}^{-3}$. The top 42 nm of the slab are *p*-doped with carbon atoms at a doping level of $2 \times 10^{18} \text{ cm}^{-3}$, leaving an intrinsic region of 116 nm at the core of the slab with the indium arsenide quantum dot layer at its centre. Furthermore, tunnel barriers are included in order to prevent charge carriers from tunnelling out of the quantum dot under the influence of strong external electric fields [89]. Therefore, the quantum dot layer is embedded in a 10 nm thick gallium arsenide quantum well clad by 60 nm of aluminium gallium arsenide with an aluminium composition of 35% at either side. The choice of the aluminium composition of these barriers is a compromise: on the one hand, a low aluminium composition leads to a high etch selectivity between the sacrificial layer and the tunnel barriers during the under-etching with hydrofluoric acid; on the other hand, a high aluminium composition provides an effective tunnel barrier due to the resulting large band gap. The band gap of the barrier with the chosen aluminium composition of 35% is 1.97 eV at $T = 5 \text{ K}$ [42]. The calculated band diagram of the resulting full slab structure is shown in Fig. 6.3 b.

The fabrication of electrically contacted PIN diodes that are suitable for the subsequent nanofabrication of photonic crystal structures required additional processing steps that will be described in the following. As shown in Fig. 6.4, the sample design comprises an individual mesa with dimensions of $31 \times 19 \mu\text{m}$ for each device for in-plane emission. Since the samples are eventually cleaved for in-plane optical access, the mesa structure and alignment markers for the subsequent fabrication steps were defined in a PMMA resist layer with electron beam lithography, as this technique allowed for the best alignment to the crystallographic axes of the gallium arsenide crystal. The mesas were then defined by wet etching with a dilute etchant comprising hydrogen peroxide and sulphuric acid. The etching depth was carefully

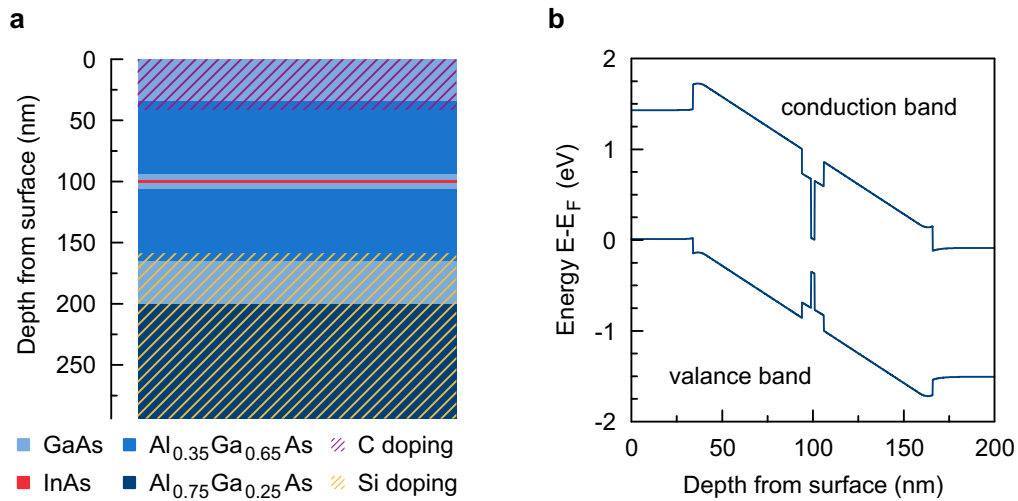


Figure 6.3 | Illustration of the layer structure and the resulting band diagram of the wafer used in this chapter. a, Schematic of the layer structure with aluminium gallium arsenide tunnel barriers and doped areas to form a PIN diode. **b**, Electronic band diagram for the layer structure shown in subfigure a calculated by solving the one-dimensional Poisson equation [250]. The diagram was calculated for zero applied bias at $T = 5$ K. For simplicity, the quantum dot layer was assumed to be pure indium arsenide.

monitored to make sure to etch well into the buried n -doped region of the slab, but to stop short of the sacrificial layer in order to avoid exposure of the aluminium gallium arsenide. An ohmic contact to the n -doped gallium arsenide layer which is common to all mesas was then formed by the evaporation and annealing of a gold germanium nickel alloy [251]. The p -doped layer was contacted for each mesa individually by evaporating a thin titanium adhesion layer followed by layer of gold, forming the electrical contact. To eliminate leakage current through areas of the sample that did not contain devices, the titanium gold contact was insulated from the sample by a layer of silicon nitride except for a small area on each mesa (see Fig. 6.4 a). The subsequent under-etching of the photonic crystal slabs in hydrofluoric acid also etches both the insulating silicon nitride layer and the titanium adhesion layer of the top contact, which leads to a degradation of the contact characteristics. The top contact was therefore encapsulated with a cured layer of polyimide, which is essentially inert to hydrofluoric acid [252]. As shown in Fig. 6.4 b, in the sample design used here, the top contacts of 37 mesas were connected in parallel in order to reduce the number of required bond wires. This completes the fabrication of the PIN diodes required for the electrical tuning of the emission wavelength of quantum dots, and it was followed by the standard processing steps for the nanofabrication of the photonic crystal structures described in Section 3.2. The short plasma etch that is employed at the end of the photonic crystal processing to remove the side wall

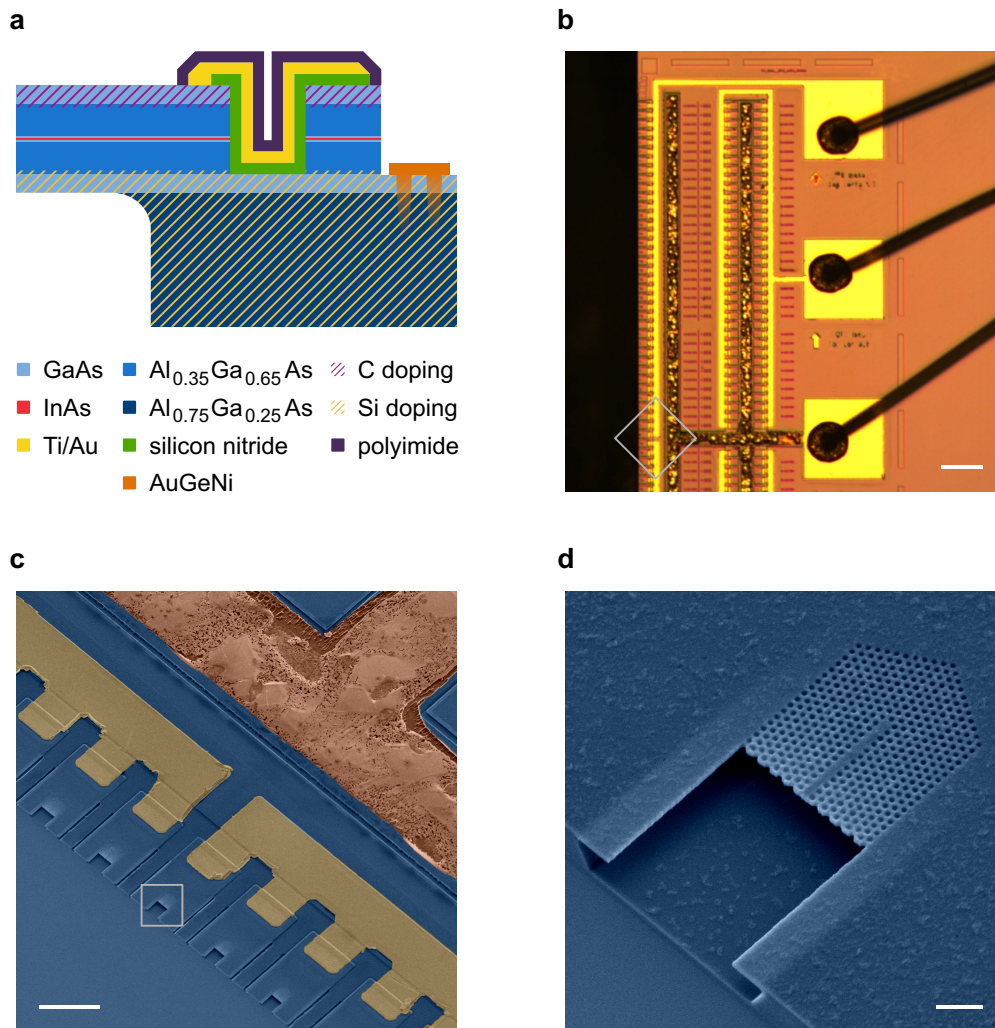


Figure 6.4 | Sample design for electrically tunable on-chip single photon sources. **a**, Cross-section of a device including mesa and top and bottom contacts. The illustration is not to scale. **b**, Chip layout including devices for in-plane emission and bond pads for top and bottom contacts. The scale bar corresponds to 100 μm . **c**, Sample layout with mesas, top contact (false colour gold), and bottom contact (false colour bronze). The scale bar corresponds to 20 μm . **d**, Unidirectional photonic crystal waveguide. The scale bar corresponds to 1 μm .

passivation layer also strips both the polyimide and any silicon nitride that extends beyond the metallisation, which is why these two components of the sample design are not visible in the micrographs shown in Fig. 6.4 b and c.

The device functionality for directing the emission of an electrically controllable quantum dot into the sample plane was obtained by coupling the quantum dot transition to a y -polarised propagating mode in a photonic crystal waveguide [200]. The photonic crystal

structure used in the experiments described in the following section therefore consists of a unidirectional waveguide with a length of 12.5 unit cells. It is surrounded by 10 periods of the two-dimensional photonic crystal, and is basically identical to the design used in Chapter 4 for the demonstration of slow-light enhanced on-chip single photon emission. The hole normalised diameter was chosen to be nominally 0.315. The scanning electron micrograph of such a device shown in Fig. 6.4 d reveals an undesirable contamination of the sample surface, which is attributed to remnants from the additional processing steps required to fabricate the electrical contacts for the PIN diode.

This concludes the description of the design and nanofabrication of devices for the electro-optic tuning of the emission wavelength of integrable single photon sources based on quantum dots in photonic crystal waveguides. In the following section, the electrical and optical characteristics of such devices will be presented.

6.3 Electrically tunable in-plane single photon emission

The most pronounced difference between the devices discussed in the previous chapters and those studied in this section is the combination of the photonic crystal – quantum dot system with an electrical PIN diode. Good electrical characteristics of this diode structure are a prerequisite for the successful electro-optical tuning of the single photon emission wavelength

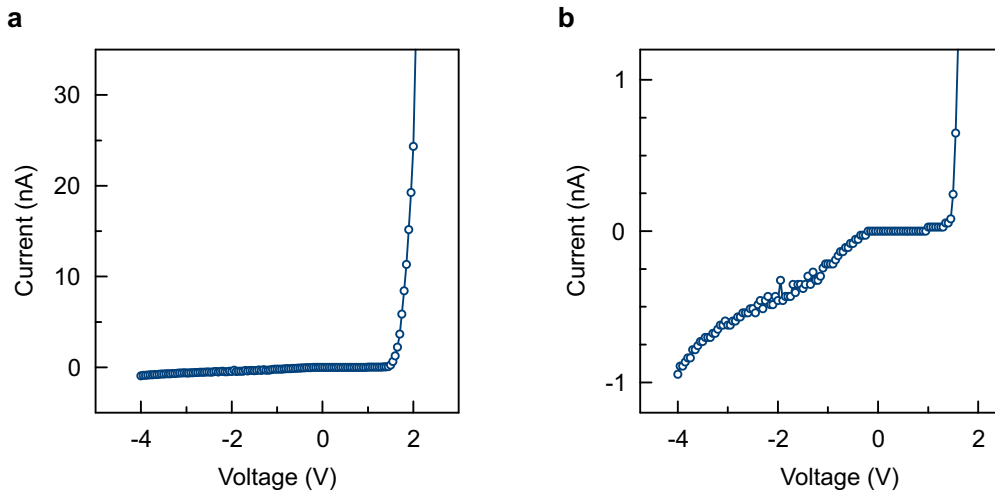


Figure 6.5 | Typical I - V characteristics of the PIN diode mesas for in-plane emission. The data was recorded at $T = 5$ K without illumination. Shown are average currents per mesa as measured for a set of 37 mesas connected in parallel. **a**, The I - V curve shows the typical characteristics of a PIN diode with a turn-on voltage of +1.71 V. **b**, The magnification of subfigure a reveals low leakage currents of less than 1 nA even at a reverse bias of -4 V.

of the devices under study here. Figure 6.5 a shows the current-voltage characteristics of a typical mesa containing a photonic crystal device at $T = 5$ K and without illumination. It exhibits a low leakage current at reverse bias voltages and negligible currents for forward bias voltages up to the turn-on voltage of 1.71 V. At higher forward voltages, the current increases sharply. From the experimentally determined turn-on voltage V_{on} and the thickness of the intrinsic region d_{int} , the diode's built-in field can be determined as

$$F_{\text{bi}} = \frac{V_{\text{on}}}{d_{\text{int}}} = 147.4 \frac{\text{kV}}{\text{cm}}. \quad (6.2)$$

The turn-on voltage is slightly lower than would be expected in view of the band gap of the aluminium gallium arsenide barriers of 1.97 eV. This discrepancy is attributed to relatively low doping densities of the p - and n -doped regions of the structure, which are required to obtain photonic crystals with good optical properties [88]. The magnification of the current-voltage characteristics shown in Fig. 6.5 b reveals very low leakage currents of less than 1 nA per mesa even for reverse bias voltages of up to -4 V, which is a result of the electrical insulation of the top contacts everywhere except on the mesas, as described in the previous section.

For the optical characterisation of the devices described in the following subsections, originally the previously employed above-band excitation was used. However, charge carriers created in the gallium arsenide matrix led to a partial screening of the applied electric field and therefore limited the achievable tuning range. The samples were therefore excited with a continuous-wave diode laser emitting at a wavelength of 850 nm. Since the corresponding photon energy of 1.46 eV is lower than the band gap energy of the gallium arsenide matrix (1.52 eV at $T = 5$ K [42]), this excitation scheme creates carriers only in the wetting layer and the quantum dots [89]. Unfortunately, a pulsed laser emitting at a similar wavelength was not available, preventing time-resolved photoluminescence spectroscopy on these samples.

6.3.1 Device A: tuning range of 1.3 nm

The first device that is presented has a lattice constant of 235 nm. The analysis of scanning electron micrographs of nominally identical devices from the same chip showed that the normalised hole radius was $\frac{r}{a} = 0.308$, close to the designed value. Figure 6.6 shows the in-plane photoluminescence spectra as a function of the applied bias voltage. The emission wavelength of the transition of interest shifts from 901.7 nm at a bias voltage of -3.9 V to 900.3 nm at $V_{\text{bias}} = +1.1$ V, which corresponds to a total tuning range of 1.3 nm. The emission intensity stays approximately constant across the entire tuning range. Most of the tuning appears in a bias voltage range from -0.5 V to $+1.0$ V, where it exhibits the theoretically expected parabolic characteristic described by Eqn. 6.1. At more negative voltages, however, a clear deviation from this behaviour was observed, which limited the achievable total tuning range. This could be caused by the charging of dangling bonds at the gallium arsenide–vacuum interfaces of the photonic crystal structure that partly screen the external electric field [253],

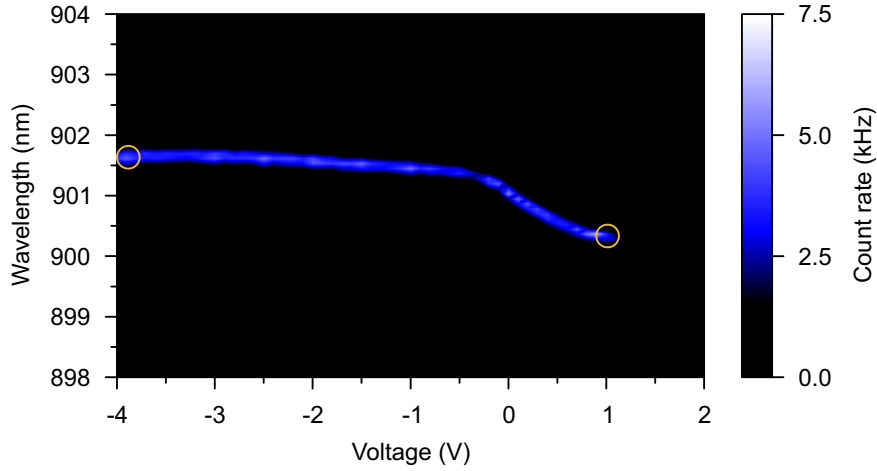


Figure 6.6 | Emission spectrum as a function of bias voltage. The emission wavelength tunes with bias voltage from 901.7 nm at $V_{\text{bias}} = -3.9$ V to 900.3 nm at $V_{\text{bias}} = +1.1$ V. The yellow circles indicate the data points for which the autocorrelation measurements shown in Fig. 6.8 were taken. The data was recorded at $T = 5$ K and $P_{\text{ex}} = 43 \mu\text{W}$.

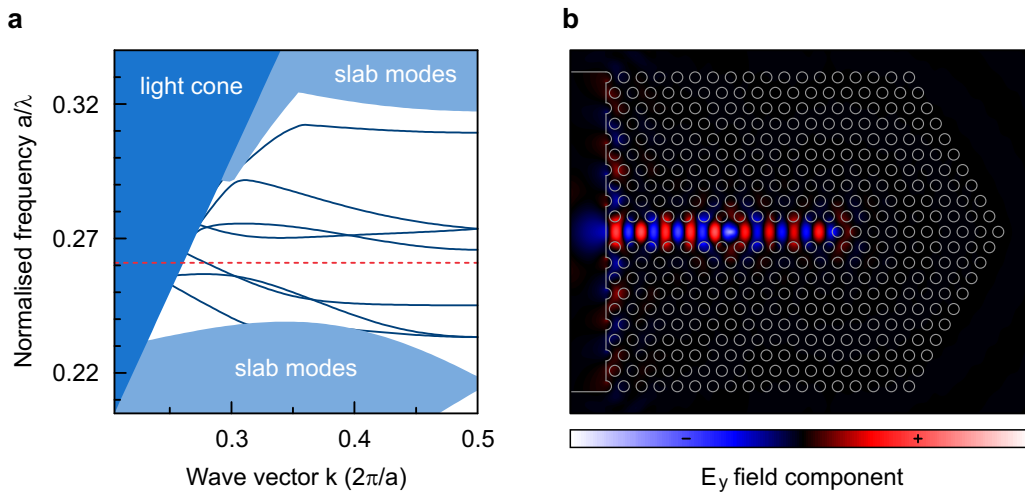


Figure 6.7 | Coupling of the transition to a guided mode in the unidirectional waveguide. The data was simulated for $\frac{r}{a} = 0.308$ and $\frac{d}{a} = 0.851$. **a**, Band diagram of an infinite photonic crystal waveguide corresponding to the unidirectional waveguide used in the experiments. The transition frequency is indicated by a dashed red line. **b**, Mode profile of the E_y field component of the corresponding mode in the unidirectional waveguide. The structure was excited at $\lambda = 900.33$ nm, corresponding to a normalised frequency of $\frac{a}{\lambda} = 0.261$.

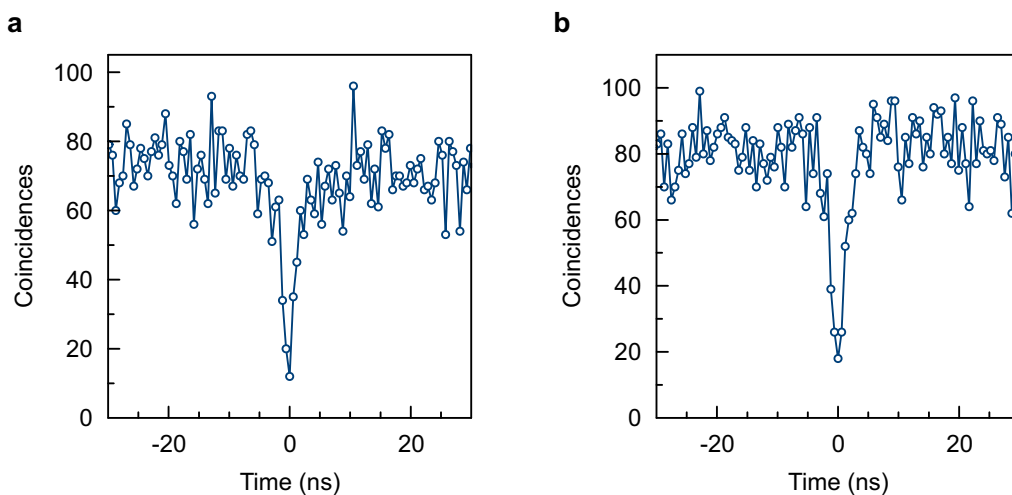


Figure 6.8 | Autocorrelation measurements for different bias voltages. The measurements were taken at $T = 5$ K and $P_{\text{ex}} = 43 \mu\text{W}$. **a**, Autocorrelation at $V_{\text{bias}} = -3.9$ V, i.e. at a wavelength of 901.7 nm. **b**, Autocorrelation at $V_{\text{bias}} = +1.1$ V, i.e. at a wavelength of 900.3 nm.

or alternatively by a depletion of carriers in the doped gallium arsenide layers at larger bias voltages.

Figure 6.7 a shows the band diagram of an infinite photonic crystal waveguide with the structural parameters of the device under study in this subsection. The red dashed line indicates the normalised frequency of the quantum dot transition of interest, which shows that the unidirectional waveguide exhibits a propagating mode at this frequency. Figure 6.7 b shows the corresponding mode profile of the E_y field component, which reveals that this propagating mode is indeed y -polarised due to the field profile's parity with respect to the waveguide axis. The observation of the in-plane photoluminescence signal from the quantum dot is therefore due to the coupling of this transition to this y -polarised propagating mode in the waveguide.

The photon statistics of the in-plane emission was studied with a Hanbury Brown and Twiss experiment (see Section 3.3) at opposite ends of the tuning range, i.e. at applied bias voltages of -3.9 V and $+1.1$ V, as marked with yellow circles in Fig. 6.6. The corresponding measured autocorrelations are shown in Fig. 6.8 a and b, respectively, and prove that the good single photon emission characteristics with $g^{(2)}(0) \leq 0.23$ are preserved across the tuning range.

6.3.2 Device B: tuning range of 1.9 nm

A second device with a nominal lattice constant of 237 nm was studied in the same manner as the one presented in the previous subsection. The scanning electron micrograph analysis

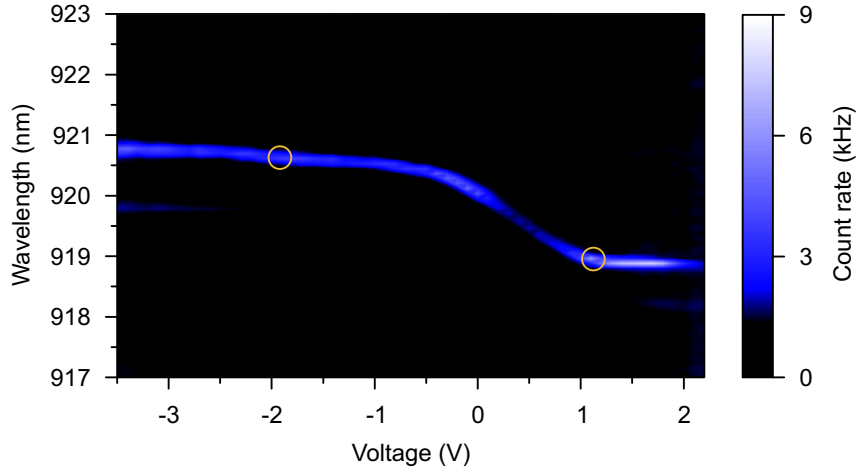


Figure 6.9 | Emission spectrum as a function of bias voltage. The emission wavelength tunes with bias voltage from 920.8 nm at $V_{\text{bias}} = -3.5$ V to 918.9 nm at $V_{\text{bias}} = +2.0$ V. The yellow circles indicate the data points for which the autocorrelation measurements shown in Fig. 6.11 were taken. The data was recorded at $T = 5$ K and $P_{\text{ex}} = 64 \mu\text{W}$.

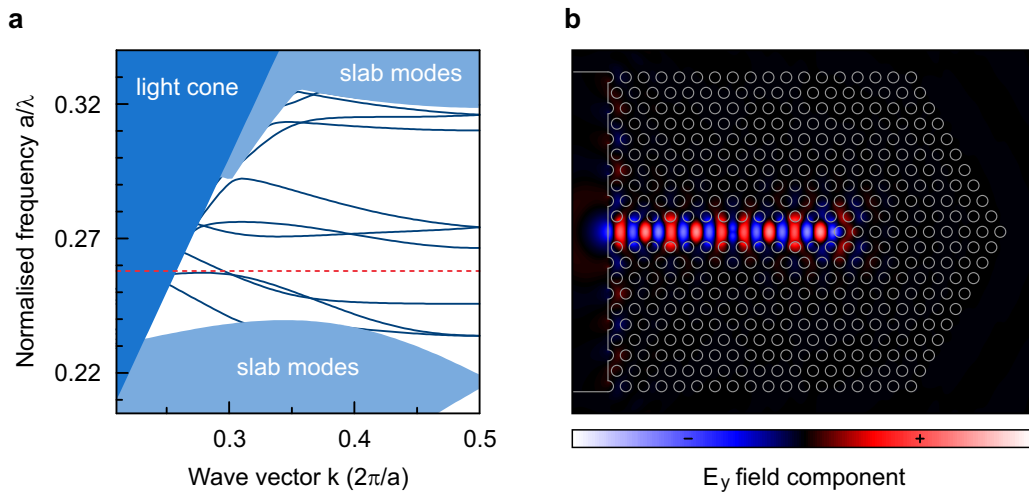


Figure 6.10 | Coupling of the transition to a guided mode in the unidirectional waveguide. The data was simulated for $\frac{r}{a} = 0.309$ and $\frac{d}{a} = 0.844$. **a**, Band diagram of an infinite photonic crystal waveguide corresponding to the unidirectional waveguide used in the experiments. The transition frequency is indicated by a dashed red line. **b**, Mode profile of the E_y field component of the corresponding mode in the unidirectional waveguide. The structure was excited at $\lambda = 921.08$ nm, corresponding to a normalised frequency of $\frac{a}{\lambda} = 0.257$.

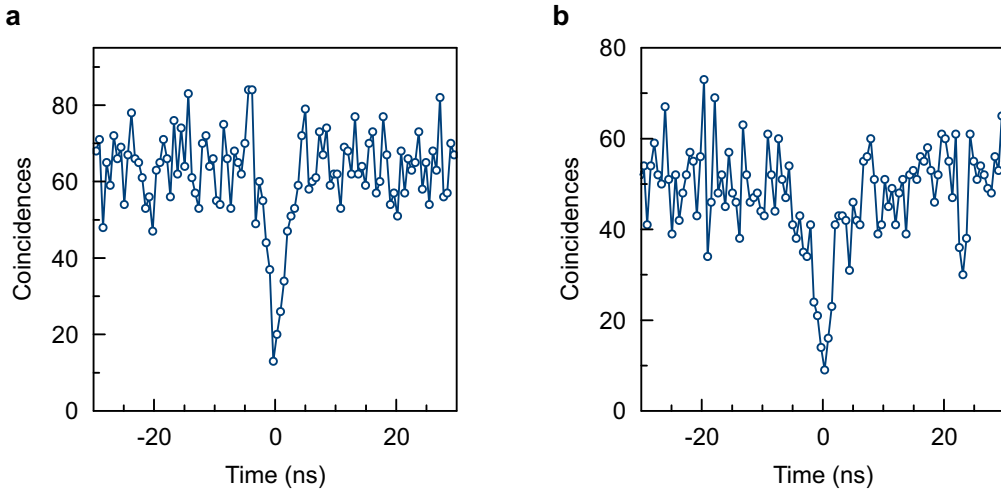


Figure 6.11 | Autocorrelation measurements for different bias voltages. The measurements were taken at $T = 5$ K and $P_{\text{ex}} = 64 \mu\text{W}$. **a**, Autocorrelation at $V_{\text{bias}} = -1.9$ V, i.e. at a wavelength of 921.0 nm. **b**, Autocorrelation at $V_{\text{bias}} = +1.2$ V, i.e. at a wavelength of 919.3 nm.

of a nominally identical device showed a normalised hole radius of $\frac{r}{a} = 0.309$, close to the designed value and almost identical to device A. The transition that is studied in this subsection was at a slightly longer wavelength, at around 920 nm, and the tuning behaviour of this transition as a function of the applied bias voltage is shown in Fig. 6.9. The transition tunes from a wavelength of 920.8 nm at a bias voltage of -3.5 V to 918.9 nm at $V_{\text{bias}} = +2.0$ V, corresponding to a total tuning range of 1.9 nm. The overall tuning behaviour of device A is essentially reproduced with the device under study here, indicating that it is similarly affected by the charging of dangling bonds or contact depletion. Most of the tuning again appears for bias voltages ranging from -0.5 V to $+1.0$ V. However, the emission intensity drops slightly in the voltage range with the highest tuning rate, a feature not observed in device A. The larger total tuning range is attributed to the longer transition wavelength, or equivalently the larger dimension of the quantum dot, which results in a stronger quantum-confined Stark effect [254, 255].

Figure 6.10 shows the band diagram of an infinite photonic crystal waveguide with the structural parameters of device B. The red dashed line indicates the normalised frequency of the corresponding transition, which shows that the transition of interest in device B is coupled to the same propagating mode as that in device A (albeit at a different wave vector). The corresponding mode profile of the E_y field component shown in Fig. 6.10 b consequently has very similar characteristics to that shown for device A in Fig. 6.7 b.

Finally, the photon statistics of the in-plane emission of device B was studied, and the resulting autocorrelations are shown in Fig. 6.11 a and b for applied bias voltages of -1.9 V and $+1.2$ V (indicated by yellow circles in Fig. 6.9), in between which most of the tuning appears.

The good single photon emission characteristics of device B are also preserved across the tuning range with $g^{(2)}(0) \leq 0.20$ at these two bias voltages.

In conclusion, the motivation for scalably and independently tunable in-plane single photon sources was given, and the quantum-confined Stark effect was introduced and discussed as a promising mechanism to realise this feature. The modified wafer structure and the additional processing steps that were necessary to fabricate PIN diodes that are compatible with two-dimensional photonic crystal structures was discussed in detail. Finally, two different electrically tunable in-plane single photon sources with tuning ranges of 1.3 nm and 1.9 nm were presented. These results are an important step towards realising a large number of integrable single photon sources that all emit single photons at the same wavelength, which is a prerequisite for the realisation of scalable schemes in quantum information processing.

7 Summary and outlook

One of the many attractive properties of semiconductor quantum dots as sources of single photons is the possibility to monolithically implement them with fully integrated quantum photonic circuits on a single chip. Even though this prospect holds enormous potential for the scalability of schemes in optical quantum information processing, in all the experimental demonstrations of single photon sources based on quantum dots prior to this work, the emission was directed vertically out of the chip plane, which is inherently incompatible with planar integration. This shortcoming was addressed in this dissertation by combining semiconductor quantum dots with two-dimensional photonic crystal slab structures, which led to the successful demonstration of on-chip single photon sources.

The first experimental demonstration of an integrable in-plane single photon source at optical wavelengths was presented in this dissertation. Single photons were generated by spontaneous recombination of excitons in an indium arsenide quantum dot, and the emission was directed into an optimised unidirectional photonic crystal waveguide by resonant coupling of the quantum dot transition to a slow-light mode of the waveguide with a Q -factor of 600. A study of the temporal evolution of in-plane photoluminescence signal revealed slow-light induced Purcell enhancement by an estimated factor of up to 2.1. Autocorrelation measurements in a Hanbury Brown and Twiss experiment showed $g^{(2)}(\tau = 0)$ values as low as 0.23, and the internal single photon emission rate after correction for multi-photon pulses was determined to be up to 18.7 MHz. This translates into a remarkable estimated internal device efficiency of up to 47%.

Applications of quantum light sources in quantum information processing will require single photons with a high indistinguishability, which can be increased by Purcell enhancement. Compared to slow-light modes in photonic crystal waveguides, point defect cavities in two-dimensional photonic crystal slabs are better suited for the Purcell enhancement of radiative transitions owing to their smaller mode volumes and higher Q -factors. To harness this potential for integrable single photon sources, waveguide-coupled L3 defect cavities were studied in great detail in this dissertation. The full mode structure of a stand-alone L3 cavity was studied experimentally to identify the resonant mode that is most suitable for Purcell enhancement. The coupling of this mode to propagating modes in photonic crystal waveguides for in-plane emission was then studied both theoretically and experimentally. For the optimised device design, a record Q -factor of 5150 for a waveguide-coupled L3 cavity was demonstrated, and Purcell-enhanced in-plane single photon emission from such a device

with a Q -factor of 3100 was achieved. These encouraging results demonstrate the potential of waveguide-coupled L3 cavities for the generation of indistinguishable single photons with integrable sources.

The indistinguishability of single photons from different quantum dot-based sources is strongly compromised by the random distribution of emission wavelengths owing to size differences caused by the self-assembly of quantum dots during growth. In order to address this problem, the quantum-confined Stark effect was exploited in this dissertation to electrically tune the emission wavelength of in-plane single photon sources. A suitable wafer structure including tunnel barriers was designed, and a chip layout was specifically devised for the combination of the required PIN diodes and photonic crystal structures with the ability of in-plane emission. By coupling the quantum dot transitions to propagating modes in unidirectional photonic crystal waveguides, the emission was directed into the chip plane. Two different in-plane single photon sources with $g^{(2)}(\tau = 0)$ values below 0.23 were presented. A first device emitting at approximately 901 nm exhibited an electrical tuning range of 1.3 nm, while a second device with a larger tuning range of 1.9 nm emitted single photons with a wavelength of about 920 nm. These results pave the way for larger sets of single photon sources emitting at identical wavelengths.

Despite the progress that has been made towards the integration of single photon sources with quantum photonic circuits in this dissertation, many challenges still remain. Possible future work can be broadly grouped into two main directions. The first is concerned with the further development of the single photon sources and the improvement of their properties. Unquestionably the biggest challenge in terms of scalability is the random positioning of the nucleation sites of nanoislands during the growth process of quantum dots. Since very promising progress on the position-controlled growth of quantum dots has been made recently [85], a combination of such dots with the device structures studied in this thesis is an exciting prospect. This could help to fully harness the potential of the waveguide-coupled L3 cavities for Purcell-enhancement, and could eventually lead to the demonstration of the in-plane emission of indistinguishable single photons. Another worthwhile direction for the improvement of the sources could be the realisation of electrically driven [20] in-plane single photon sources, which would be very attractive from a practical point of view as this excitation technique is more easily scalable than the optical excitation used here. The second main direction would be concerned with the actual integration of in-plane single photon sources with larger, more complex quantum photonic circuits. The direct integration with photonic crystal waveguides would be one option, as waveguide bends [256], beamsplitters [257, 258] and phase shifters [134, 138] have been demonstrated with these structures. An alternative would be the coupling of the photonic crystal waveguides to other types of waveguides, with which building blocks of a quantum computer have already been demonstrated successfully [15, 16].

Bibliography

- [1] G. Moore. “Cramming more components onto integrated circuits.” *Electronics Magazine* **38**, 114 (1965).
- [2] P. Peercy. “The drive to miniaturization.” *Nature* **406**, 1023 (2000).
- [3] C. Forst, C. Ashman, K. Schwarz, and P. Blochl. “The interface between silicon and a high- k oxide.” *Nature* **427**, 53 (2004).
- [4] M. Nielsen and I. Chuang. *Quantum Computation and Quantum Information*. Cambridge University Press (2000).
- [5] D. Deutsch. “Quantum theory, the Church-Turing principle and the universal quantum computer.” *Proceedings of the Royal Society of London A* **400**, 97 (1985).
- [6] J. L. O’Brien, A. Furusawa, and J. Vučković. “Photonic quantum technologies.” *Nature Photonics* **3**, 687 (2009).
- [7] C. H. W. Barnes, J. M. Shilton, and A. M. Robinson. “Quantum computation using electrons trapped by surface acoustic waves.” *Physical Review B* **62**, 8410 (2000).
- [8] T. D. Ladd, F. Jelezko, R. Laflamme, Y. Nakamura, C. Monroe, and J. L. O’Brien. “Quantum computers.” *Nature* **464**, 45 (2010).
- [9] J. L. O’Brien. “Optical quantum computing.” *Science* **318**, 1567 (2007).
- [10] G. J. Milburn. “Quantum optical Fredkin gate.” *Physical Review Letters* **62**, 2124 (1989).
- [11] E. Knill, R. Laflamme, and G. Milburn. “A scheme for efficient quantum computation with linear optics.” *Nature* **409**, 46 (2001).
- [12] T. C. Ralph, N. K. Langford, T. B. Bell, and A. G. White. “Linear optical controlled-NOT gate in the coincidence basis.” *Physical Review A* **65**, 062324 (2002).
- [13] T. B. Pittman, M. J. Fitch, B. C. Jacobs, and J. D. Franson. “Experimental controlled-NOT logic gate for single photons in the coincidence basis.” *Physical Review A* **68**, 032316 (2003).
- [14] J. O’Brien, G. Pryde, A. White, T. Ralph, and D. Branning. “Demonstration of an all-optical quantum controlled-NOT gate.” *Nature* **426**, 264 (2003).

- [15] A. Politi, M. J. Cryan, J. G. Rarity, S. Yu, and J. L. O'Brien. "Silica-on-silicon waveguide quantum circuits." *Science* **320**, 646 (2008).
- [16] M. A. Pooley, D. J. P. Ellis, R. B. Patel, A. J. Bennett, K. H. A. Chan, I. Farrer, D. A. Ritchie, and A. J. Shields. "Controlled-NOT gate operating with single photons." *Applied Physics Letters* **100**, 211103 (2012).
- [17] B. Lounis and M. Orrit. "Single-photon sources." *Reports on Progress in Physics* **68**, 1129 (2005).
- [18] A. J. Shields. "Semiconductor quantum light sources." *Nature Photonics* **1**, 215 (2007).
- [19] H. Drexler, D. Leonard, W. Hansen, J. P. Kotthaus, and P. M. Petroff. "Spectroscopy of quantum levels in charge-tunable InGaAs quantum dots." *Physical Review Letters* **73**, 2252 (1994).
- [20] Z. Yuan, B. Kardynal, R. Stevenson, A. Shields, C. Lobo, K. Cooper, N. Beattie, D. Ritchie, and M. Pepper. "Electrically driven single-photon source." *Science* **295**, 102 (2002).
- [21] P. Michler, A. Kiraz, C. Becher, W. Schoenfeld, P. Petroff, L. Zhang, E. Hu, and A. Imamoglu. "A quantum dot single-photon turnstile device." *Science* **290**, 2282 (2000).
- [22] C. Santori, D. Fattal, J. Vučković, G. Solomon, and Y. Yamamoto. "Indistinguishable photons from a single-photon device." *Nature* **419**, 594 (2002).
- [23] C. K. Hong, Z. Y. Ou, and L. Mandel. "Measurement of subpicosecond time intervals between two photons by interference." *Physical Review Letters* **59**, 2044 (1987).
- [24] A. Kiraz, M. Atatüre, and A. Imamoglu. "Quantum-dot single-photon sources: prospects for applications in linear optics quantum-information processing." *Physical Review A* **69**, 032305 (2004).
- [25] K. Vahala. "Optical microcavities." *Nature* **424**, 839 (2003).
- [26] J. Joannopoulos, P. Villeneuve, and S. Fan. "Photonic crystals: putting a new twist on light." *Nature* **386**, 143 (1997).
- [27] J. Vučković, M. Lončar, H. Mabuchi, and A. Scherer. "Design of photonic crystal microcavities for cavity QED." *Physical Review E* **65**, 016608 (2001).
- [28] P. Yao and S. Hughes. "Controlled cavity QED and single-photon emission using a photonic-crystal waveguide cavity system." *Physical Review B* **80**, 165128 (2009).
- [29] M. A. Reed, R. T. Bate, K. Bradshaw, W. M. Duncan, W. R. Frensley, J. W. Lee, and H. D. Shih. "Spatial quantization in GaAs-AlGaAs multiple quantum dots." *Journal of Vacuum Science & Technology B* **4**, 358 (1986).

- [30] W. Izumida, O. Sakai, and S. Tarucha. “Tunneling through a quantum dot in local spin singlet-triplet crossover region with Kondo effect.” *Physical Review Letters* **87**, 216803 (2001).
- [31] G. Chen, T. H. Stievater, E. T. Batteh, X. Li, D. G. Steel, D. Gammon, D. S. Katzer, D. Park, and L. J. Sham. “Biexciton quantum coherence in a single quantum dot.” *Physical Review Letters* **88**, 117901 (2002).
- [32] B. Lounis, H. A. Bechtel, D. Gerion, P. Alivisatos, and W. E. Moerner. “Photon antibunching in single CdSe/ZnS quantum dot fluorescence.” *Chemical Physics Letters* **329**, 399 (2000).
- [33] L. Goldstein, F. Glas, J. Y. Marzin, M. N. Charasse, and G. L. Roux. “Growth by molecular beam epitaxy and characterization of InAs/GaAs strained-layer superlattices.” *Applied Physics Letters* **47**, 1099 (1985).
- [34] D. Leonard, M. Krishnamurthy, C. M. Reaves, S. P. Denbaars, and P. M. Petroff. “Direct formation of quantum-sized dots from uniform coherent islands of InGaAs on GaAs surfaces.” *Applied Physics Letters* **63**, 3203 (1993).
- [35] P. Michler (editor). *Single Quantum Dots*. Springer (2003).
- [36] K. Brunner. “Si/Ge nanostructures.” *Reports on Progress in Physics* **65**, 27 (2002).
- [37] G. Walter, J. N. Holonyak, J. H. Ryou, and R. D. Dupuis. “Room-temperature continuous photopumped laser operation of coupled InP quantum dot and InGaP quantum well InP–InGaP–In(AlGa)P–InAlP heterostructures.” *Applied Physics Letters* **79**, 1956 (2001).
- [38] O. Moriwaki, T. Someya, K. Tachibana, S. Ishida, and Y. Arakawa. “Narrow photoluminescence peaks from localized states in InGaN quantum dot structures.” *Applied Physics Letters* **76**, 2361 (2000).
- [39] J. C. Kim, H. Rho, L. M. Smith, H. E. Jackson, S. Lee, M. Dobrowolska, J. L. Merz, and J. K. Furdyna. “Spectroscopic characterization of the evolution of self-assembled CdSe quantum dots.” *Applied Physics Letters* **73**, 3399 (1998).
- [40] R. Nötzel. “Self-organized growth of quantum-dot structures.” *Semiconductor Science and Technology* **11**, 1365 (1996).
- [41] M. Tytus, J. Krasnyj, W. Jacak, A. Chuchmała, W. Donderowicz, and L. Jacak. “Differences between photoluminescence spectra of type-I and type-II quantum dots.” *Journal of Physics: Conference Series* **104**, 012011 (2008).
- [42] M. Levinstein, S. Rumyantsev, and M. Shur. *Handbook Series on Semiconductor Parameters, vol. 2*. World Scientific Publishing Company (1996).

- [43] S. Guha, A. Madhukar, and K. C. Rajkumar. “Onset of incoherency and defect introduction in the initial stages of molecular beam epitaxial growth of highly strained $\text{In}_x\text{Ga}_{1-x}\text{As}$ on $\text{GaAs}(100)$.” *Applied Physics Letters* **57**, 2110 (1990).
- [44] G. A. Narvaez, G. Bester, and A. Zunger. “Dependence of the electronic structure of self-assembled $(\text{In,Ga})\text{As}/\text{GaAs}$ quantum dots on height and composition.” *Journal of Applied Physics* **98**, 043708 (2005).
- [45] W. Sheng and J.-P. Leburton. “Electron-hole alignment in InAs/GaAs self-assembled quantum dots: effects of chemical composition and dot shape.” *Physical Review B* **63**, 161301 (2001).
- [46] A. P. Alivisatos. “Semiconductor clusters, nanocrystals, and quantum dots.” *Science* **271**, 933 (1996).
- [47] R. M. Thompson, R. M. Stevenson, A. J. Shields, I. Farrer, C. J. Lobo, D. A. Ritchie, M. L. Leadbeater, and M. Pepper. “Single-photon emission from exciton complexes in individual quantum dots.” *Physical Review B* **64**, 201302 (2001).
- [48] A. Milnes and A. Polyakov. “Indium arsenide: a semiconductor for high speed and electro-optical devices.” *Materials Science and Engineering B* **18**, 237 (1993).
- [49] F. Hofbauer, S. Grimminger, J. Angele, G. Böhm, R. Meyer, M. C. Amann, and J. J. Finley. “Electrically probing photonic bandgap phenomena in contacted defect nanocavities.” *Applied Physics Letters* **91**, 201111 (2007).
- [50] K. F. Karlsson, E. S. Moskalenko, P. O. Holtz, B. Monemar, W. V. Schoenfeld, J. M. Garcia, and P. M. Petroff. “Temperature influence on optical charging of self-assembled InAs/GaAs semiconductor quantum dots.” *Applied Physics Letters* **78**, 2952 (2001).
- [51] F. Adler, M. Geiger, A. Bauknecht, F. Scholz, H. Schweizer, M. H. Pilkuhn, B. Ohnesorge, and A. Forchel. “Optical transitions and carrier relaxation in self assembled InAs/GaAs quantum dots.” *Journal of Applied Physics* **80**, 4019 (1996).
- [52] D. Heiss, V. Jovanov, M. Caesar, M. Bichler, G. Abstreiter, and J. J. Finley. “Selective optical charge generation, storage, and readout in a single self-assembled quantum dot.” *Applied Physics Letters* **94**, 072108 (2009).
- [53] A. Boyer de la Giroday, A. J. Bennett, M. A. Pooley, R. M. Stevenson, N. Sköld, R. B. Patel, I. Farrer, D. A. Ritchie, and A. J. Shields. “All-electrical coherent control of the exciton states in a single quantum dot.” *Physical Review B* **82**, 241301 (2010).
- [54] A. Baumgartner, E. Stock, A. Patané, L. Eaves, M. Henini, and D. Bimberg. “Optical imaging of electrical carrier injection into individual InAs quantum dots.” *Physical Review Letters* **105**, 257401 (2010).

- [55] P. Michler, A. Imamoglu, M. Mason, P. Carson, G. Strouse, and S. Buratto. “Quantum correlation among photons from a single quantum dot at room temperature.” *Nature* **406**, 968 (2000).
- [56] M. Fox. *Quantum Optics*. Oxford University Press (2006).
- [57] J. S. Foresi, P. R. Villeneuve, J. Ferrera, E. R. Thoen, G. Steinmeyer, S. Fan, J. D. Joannopoulos, L. C. Kimerling, H. I. Smith, and E. P. Ippen. “Photonic-bandgap microcavities in optical waveguides.” *Nature* **390**, 143 (1997).
- [58] G. Wentzel. “Über strahlungslose Quantensprünge.” *Zeitschrift für Physik* **43**, 524 (1927).
- [59] E. Fermi. *Nuclear Physics*. University of Chicago Press (1950).
- [60] E. M. Purcell, H. C. Torrey, and R. V. Pound. “Resonance absorption by nuclear magnetic moments in a solid.” *Physical Review* **69**, 37 (1946).
- [61] D. Englund, D. Fattal, E. Waks, G. Solomon, B. Zhang, T. Nakaoka, Y. Arakawa, Y. Yamamoto, and J. Vučković. “Controlling the spontaneous emission rate of single quantum dots in a two-dimensional photonic crystal.” *Physical Review Letters* **95**, 013904 (2005).
- [62] A. Kress, F. Hofbauer, N. Reinelt, H. Krenner, M. Bichler, D. Schuh, R. Meyer, G. Abstreiter, and J. J. Finley. “Investigation of cavity modes and direct observation of Purcell enhancement in 2D photonic crystal defect microcavities.” *Physica E* **26**, 351 (2005).
- [63] D. Englund, A. Faraon, I. Fushman, N. Stoltz, P. Petroff, and J. Vučković. “Controlling cavity reflectivity with a single quantum dot.” *Nature* **450**, 857 (2007).
- [64] A. Kress, F. Hofbauer, N. Reinelt, M. Kaniber, H. J. Krenner, R. Meyer, G. Böhm, and J. J. Finley. “Manipulation of the spontaneous emission dynamics of quantum dots in two-dimensional photonic crystals.” *Physical Review B* **71**, 241304 (2005).
- [65] M. Fujita, S. Takahashi, Y. Tanaka, T. Asano, and S. Noda. “Simultaneous inhibition and redistribution of spontaneous light emission in photonic crystals.” *Science* **308**, 1296 (2005).
- [66] M. Kaniber, A. Kress, A. Laucht, M. Bichler, R. Meyer, M.-C. Amann, and J. J. Finley. “Efficient spatial redistribution of quantum dot spontaneous emission from two-dimensional photonic crystals.” *Applied Physics Letters* **91**, 061106 (2007).
- [67] M. Kaniber, A. Laucht, T. Hürlimann, M. Bichler, R. Meyer, M.-C. Amann, and J. J. Finley. “Highly efficient single-photon emission from single quantum dots within a two-dimensional photonic band-gap.” *Physical Review B* **77**, 073312 (2008).

- [68] E. Moreau, I. Robert, J. M. Gérard, I. Abram, L. Manin, and V. Thierry-Mieg. “Single-mode solid-state single photon source based on isolated quantum dots in pillar microcavities.” *Applied Physics Letters* **79**, 2865 (2001).
- [69] E. Jaynes and F. Cummings. “Comparison of quantum and semiclassical radiation theories with application to the beam maser.” *Proceedings of the IEEE* **51**, 89 (1963).
- [70] I. I. Rabi. “Space quantization in a gyrating magnetic field.” *Physical Review* **51**, 652 (1937).
- [71] J. J. Hopfield. “Theory of the contribution of excitons to the complex dielectric constant of crystals.” *Physical Review* **112**, 1555 (1958).
- [72] M. Brune, F. Schmidt-Kaler, A. Maali, J. Dreyer, E. Hagley, J. M. Raimond, and S. Haroche. “Quantum Rabi oscillation: a direct test of field quantization in a cavity.” *Physical Review Letters* **76**, 1800 (1996).
- [73] J. Reithmaier, G. Sek, A. Löffler, C. Hofmann, S. Kuhn, S. Reitzenstein, L. Keldysh, V. Kulakovskii, T. Reinecke, and A. Forchel. “Strong coupling in a single quantum dot-semiconductor microcavity system.” *Nature* **432**, 197 (2004).
- [74] S. M. Thon, M. T. Rakher, H. Kim, J. Gudat, W. T. M. Irvine, P. M. Petroff, and D. Bouwmeester. “Strong coupling through optical positioning of a quantum dot in a photonic crystal cavity.” *Applied Physics Letters* **94**, 111115 (2009).
- [75] A. Laucht, N. Hauke, J. M. Villas-Bôas, F. Hofbauer, G. Böhm, M. Kaniber, and J. J. Finley. “Dephasing of exciton polaritons in photoexcited InGaAs quantum dots in GaAs nanocavities.” *Physical Review Letters* **103**, 087405 (2009).
- [76] G. Cui and M. Raymer. “Quantum efficiency of single-photon sources in the cavity-QED strong-coupling regime.” *Optics Express* **13**, 9660 (2005).
- [77] D. Press, S. Götzinger, S. Reitzenstein, C. Hofmann, A. Löffler, M. Kamp, A. Forchel, and Y. Yamamoto. “Photon antibunching from a single quantum-dot-microcavity system in the strong coupling regime.” *Physical Review Letters* **98**, 117402 (2007).
- [78] P. Kaer, P. Lodahl, A. P. Jauho, and J. Mork. “Microscopic theory of indistinguishable single-photon emission from a quantum dot coupled to a cavity: the role of non-Markovian phonon-induced decoherence.” *arXiv* 1203.6268v3 (2012).
- [79] K. Hennessy, A. Badolato, M. Winger, D. Gerace, M. Atatuere, S. Gulde, S. Faelt, E. L. Hu, and A. Imamoglu. “Quantum nature of a strongly coupled single quantum dot-cavity system.” *Nature* **445**, 896 (2007).

- [80] K. Hennessy, A. Badolato, P. Petroff, and E. Hu. “Positioning photonic crystal cavities to single InAs quantum dots.” *Photonics and Nanostructures* **2**, 65 (2004).
- [81] A. Badolato, K. Hennessy, M. Atature, J. Dreiser, E. Hu, P. M. Petroff, and A. Imamoglu. “Deterministic coupling of single quantum dots to single nanocavity modes.” *Science* **308**, 1158 (2005).
- [82] K. H. Lee, A. M. Green, R. A. Taylor, D. N. Sharp, J. Scrimgeour, O. M. Roche, J. H. Na, A. F. Jarjour, A. J. Turberfield, F. S. F. Brossard, D. A. Williams, and G. A. D. Briggs. “Registration of single quantum dots using cryogenic laser photolithography.” *Applied Physics Letters* **88**, 193106 (2006).
- [83] A. Dousse, L. Lanco, J. Suffczyński, E. Semenova, A. Miard, A. Lemaitre, I. Sagnes, C. Roblin, J. Bloch, and P. Senellart. “Controlled light-matter coupling for a single quantum dot embedded in a pillar microcavity using far-field optical lithography.” *Physical Review Letters* **101**, 267404 (2008).
- [84] A. Mohan, P. Gallo, M. Felici, B. Dwir, A. Rudra, J. Faist, and E. Kapon. “Record-low inhomogeneous broadening of site-controlled quantum dots for nanophotonics.” *Small* **6**, 1268 (2010).
- [85] J. Skiba-Szymanska, A. Jamil, I. Farrer, M. B. Ward, C. A. Nicoll, D. J. P. Ellis, J. P. Griffiths, D. Anderson, G. A. C. Jones, D. A. Ritchie, and A. J. Shields. “Narrow emission linewidths of positioned InAs quantum dots grown on pre-patterned GaAs(100) substrates.” *Nanotechnology* **22**, 065302 (2011).
- [86] P. Gallo, M. Felici, B. Dwir, K. A. Atlasov, K. F. Karlsson, A. Rudra, A. Mohan, G. Biasiol, L. Sorba, and E. Kapon. “Integration of site-controlled pyramidal quantum dots and photonic crystal membrane cavities.” *Applied Physics Letters* **92**, 263101 (2008).
- [87] D. C. Unitt, A. J. Bennett, P. Atkinson, D. A. Ritchie, and A. J. Shields. “Polarization control of quantum dot single-photon sources via a dipole-dependent Purcell effect.” *Physical Review B* **72**, 033318 (2005).
- [88] A. Laucht, F. Hofbauer, N. Hauke, J. Angele, S. Stobbe, M. Kaniber, G. Böhm, P. Lodahl, M.-C. Amann, and J. J. Finley. “Electrical control of spontaneous emission and strong coupling for a single quantum dot.” *New Journal of Physics* **11**, 023034 (2009).
- [89] A. J. Bennett, R. B. Patel, J. Skiba-Szymanska, C. A. Nicoll, I. Farrer, D. A. Ritchie, and A. J. Shields. “Giant Stark effect in the emission of single semiconductor quantum dots.” *Applied Physics Letters* **97**, 031104 (2010).

- [90] R. B. Patel, A. J. Bennett, I. Farrer, C. A. Nicoll, D. A. Ritchie, and A. J. Shields. “Two-photon interference of the emission from electrically tunable remote quantum dots.” *Nature Photonics* **4**, 632 (2010).
- [91] G. Khitrova, H. Gibbs, M. Kira, S. Koch, and A. Scherer. “Vacuum Rabi splitting in semiconductors.” *Nature Physics* **2**, 81 (2006).
- [92] J. P. Reithmaier. “Strong exciton–photon coupling in semiconductor quantum dot systems.” *Semiconductor Science and Technology* **23**, 123001 (2008).
- [93] O. Painter, R. K. Lee, A. Scherer, A. Yariv, J. D. O’Brien, P. D. Dapkus, and I. Kim. “Two-dimensional photonic band-gap defect mode laser.” *Science* **284**, 1819 (1999).
- [94] S. Combrié, A. D. Rossi, Q. V. Tran, and H. Benisty. “GaAs photonic crystal cavity with ultrahigh Q: microwatt nonlinearity at 1.55 μm .” *Optics Letters* **33**, 1908 (2008).
- [95] J. Joannopoulos, S. Johnson, J. Winn, and R. Meade. *Photonic Crystals*. Princeton University Press (2008).
- [96] S. Wang. “Principles of distributed feedback and distributed Bragg-reflector lasers.” *IEEE Journal of Quantum Electronics* **QE10**, 413 (1974).
- [97] J. W. Strutt (Lord Rayleigh). “On the maintenance of vibrations by forces of double frequency, and on the propagation of waves through a medium endowed with a periodic structure.” *Philosophical Magazine* **24**, 145 (1887).
- [98] E. Yablonovitch. “Inhibited spontaneous emission in solid-state physics and electronics.” *Physical Review Letters* **58**, 2059 (1987).
- [99] S. John. “Strong localization of photons in certain disordered dielectric superlattices.” *Physical Review Letters* **58**, 2486 (1987).
- [100] S. Lin, J. Fleming, D. Hetherington, B. Smith, R. Biswas, K. Ho, M. Sigalas, W. Zubrzycki, S. Kurtz, and J. Bur. “A three-dimensional photonic crystal operating at infrared wavelengths.” *Nature* **394**, 251 (1998).
- [101] H. M. Ng, T. D. Moustakas, and S. N. G. Chu. “High reflectivity and broad bandwidth AlN/GaN distributed Bragg reflectors grown by molecular-beam epitaxy.” *Applied Physics Letters* **76**, 2818 (2000).
- [102] P. Velha, E. Picard, T. Charvolin, E. Hadji, J. Rodier, P. Lalanne, and D. Peyrade. “Ultra-high Q/V Fabry-Perot microcavity on SOI substrate.” *Optics Express* **15**, 16090 (2007).
- [103] K. Aoki, H. Miyazaki, H. Hirayama, K. Inoshita, T. Baba, K. Sakoda, N. Shinya, and Y. Aoyagi. “Microassembly of semiconductor three-dimensional photonic crystals.” *Nature Materials* **2**, 117 (2003).

- [104] Y. Arakawa, A. Tандаechanurat, S. Iwamoto, M. Nomura, and D. Guimard. “Advances in 3D photonic crystal nanocavity with quantum dots.” *Proceedings of SPIE* **7608**, 76081A (2010).
- [105] S. Reitzenstein, C. Hofmann, A. Gorbunov, M. Strauß, S. H. Kwon, C. Schneider, A. Löffler, S. Höfling, M. Kamp, and A. Forchel. “AlAs/GaAs micropillar cavities with quality factors exceeding 150,000.” *Applied Physics Letters* **90**, 251109 (2007).
- [106] E. Kuramochi, M. Notomi, S. Mitsugi, A. Shinya, T. Tanabe, and T. Watanabe. “Ultra-high-Q photonic crystal nanocavities realized by the local width modulation of a line defect.” *Applied Physics Letters* **88**, 041112 (2006).
- [107] N. Hauke, A. Tандаechanurat, T. Zabel, T. Reichert, H. Takagi, M. Kaniber, S. Iwamoto, D. Bougeard, J. J. Finley, G. Abstreiter, and Y. Arakawa. “A three-dimensional silicon photonic crystal nanocavity with enhanced emission from embedded germanium islands.” *New Journal of Physics* **14**, 083035 (2012).
- [108] A. Tандаechanurat, S. Ishida, K. Aoki, D. Guimard, M. Nomura, S. Iwamoto, and Y. Arakawa. “Demonstration of high-Q (> 8600) three-dimensional photonic crystal nanocavity embedding quantum dots.” *Applied Physics Letters* **94**, 171115 (2009).
- [109] I. Staude, G. von Freymann, S. Essig, K. Busch, and M. Wegener. “Waveguides in three-dimensional photonic-bandgap materials by direct laser writing and silicon double inversion.” *Optics Letters* **36**, 67 (2011).
- [110] A. K. Raub and S. R. J. Brueck. “Large area three-dimensional photonic crystals with embedded waveguides.” *Journal of Vacuum Science & Technology B* **28**, C6O38 (2010).
- [111] T. Krauss, R. DeLaRue, and S. Brand. “Two-dimensional photonic-bandgap structures operating at near-infrared wavelengths.” *Nature* **383**, 699 (1996).
- [112] Y. Akahane, T. Asano, B. Song, and S. Noda. “High-Q photonic nanocavity in a two-dimensional photonic crystal.” *Nature* **425**, 944 (2003).
- [113] A. Xing, M. Davanco, D. J. Blumenthal, and E. L. Hu. “Fabrication of InP-based two-dimensional photonic crystal membrane.” *Journal of Vacuum Science & Technology B* **22**, 70 (2004).
- [114] B. Rong, H. W. M. Salemink, E. M. Roeling, R. van der Heijden, F. Karouta, and E. van der Drift. “Fabrication of two dimensional GaN nanophotonic crystals.” *Journal of Vacuum Science & Technology B* **25**, 2632 (2007).
- [115] S. Yamada, B.-S. Song, T. Asano, and S. Noda. “Silicon carbide-based photonic crystal nanocavities for ultra-broadband operation from infrared to visible wavelengths.” *Applied Physics Letters* **99**, 201102 (2011).

- [116] J. Riedrich-Möller, L. Kipfstuhl, C. Hepp, E. Neu, C. Pauly, F. Mücklich, A. Baur, M. Wandt, S. Wolff, M. Fischer, S. Gsell, M. Schreck, and C. Becher. “One- and two-dimensional photonic crystal microcavities in single crystal diamond.” *Nature Nanotechnology* **7**, 69 (2012).
- [117] G. Si, E. J. Teo, A. A. Bettiol, J. Teng, and A. J. Danner. “Suspended slab and photonic crystal waveguides in lithium niobate.” *Journal of Vacuum Science & Technology B* **28**, 316 (2010).
- [118] T. Baba. “Photonic crystals and microdisk cavities based on GaInAsP-InP system.” *IEEE Journal of Selected Topics in Quantum Electronics* **3**, 808 (1997).
- [119] Y. Kurosaka, S. Iwahashi, Y. Liang, K. Sakai, E. Miyai, W. Kunishi, D. Ohnishi, and S. Noda. “On-chip beam-steering photonic-crystal lasers.” *Nature Photonics* **4**, 447 (2010).
- [120] L. Yang, J. Motohisa, J. Takeda, and T. Fukui. “Photonic crystal slabs with hexagonal air holes fabricated by selective area metal organic vapor phase epitaxy.” *Sensors and Actuators A* **133**, 288 (2007).
- [121] H.-Y. Ryu, S.-H. Kim, H.-G. Park, and Y.-H. Lee. “Characteristics of single defect laser modes in a two-dimensional square lattice photonic crystal slab.” *Journal of Applied Physics* **93**, 831 (2003).
- [122] K. Hennessy, C. Reese, A. Badolato, C. F. Wang, A. Imamoğlu, P. M. Petroff, and E. Hu. “Fabrication of high Q square-lattice photonic crystal microcavities.” *Journal of Vacuum Science & Technology B* **21**, 2918 (2003).
- [123] A. Garcia-Adeva. “Band gap atlas for photonic crystals having the symmetry of the kagomé and pyrochlore lattices.” *New Journal of Physics* **8**, 86 (2006).
- [124] S. G. Johnson, S. Fan, P. R. Villeneuve, J. D. Joannopoulos, and L. A. Kolodziejski. “Guided modes in photonic crystal slabs.” *Physical Review B* **60**, 5751 (1999).
- [125] U. K. Khankhoje, S.-H. Kim, B. C. Richards, J. Hendrickson, J. Sweet, J. D. Olitzky, G. Khitrova, H. M. Gibbs, and A. Scherer. “Modelling and fabrication of GaAs photonic-crystal cavities for cavity quantum electrodynamics.” *Nanotechnology* **21**, 065202 (2010).
- [126] O. Painter, J. Vučković, and A. Scherer. “Defect modes of a two-dimensional photonic crystal in an optically thin dielectric slab.” *Journal of the Optical Society of America B* **16**, 275 (1999).

- [127] S. G. Johnson, P. R. Villeneuve, S. Fan, and J. D. Joannopoulos. "Linear waveguides in photonic-crystal slabs." *Physical Review B* **62**, 8212 (2000).
- [128] K. Srinivasan and O. Painter. "Momentum space design of high-Q photonic crystal optical cavities." *Optics Express* **10**, 670 (2002).
- [129] K. Nozaki and T. Baba. "Laser characteristics with ultimate-small modal volume in photonic crystal slab point-shift nanolasers." *Applied Physics Letters* **88**, 211101 (2006).
- [130] M. Shirane, S. Kono, J. Ushida, S. Ohkouchi, N. Ikeda, Y. Sugimoto, and A. Tomita. "Mode identification of high-quality-factor single-defect nanocavities in quantum dot-embedded photonic crystals." *Journal of Applied Physics* **101**, 073107 (2007).
- [131] M. Fujita, Y. Tanaka, and S. Noda. "Light emission from silicon in photonic crystal nanocavity." *IEEE Journal of Selected Topics in Quantum Electronics* **14**, 1090 (2008).
- [132] A. Mekis, J. C. Chen, I. Kurland, S. Fan, P. R. Villeneuve, and J. D. Joannopoulos. "High transmission through sharp bends in photonic crystal waveguides." *Physical Review Letters* **77**, 3787 (1996).
- [133] S. McNab, N. Moll, and Y. Vlasov. "Ultra-low loss photonic integrated circuit with membrane-type photonic crystal waveguides." *Optics Express* **11**, 2927 (2003).
- [134] Y. Vlasov, M. O'Boyle, H. Hamann, and S. McNab. "Active control of slow light on a chip with photonic crystal." *Nature* **438**, 65 (2005).
- [135] M. G. Banaee, A. G. Pattantyus-Abraham, M. W. McCutcheon, G. W. Rieger, and J. F. Young. "Efficient coupling of photonic crystal microcavity modes to a ridge waveguide." *Applied Physics Letters* **90**, 193106 (2007).
- [136] T. F. Krauss. "Why do we need slow light?" *Nature Photonics* **2**, 448 (2008).
- [137] T. F. Krauss. "Slow light in photonic crystal waveguides." *Journal of Physics D* **40**, 2666 (2007).
- [138] T. Baba. "Slow light in photonic crystals." *Nature Photonics* **2**, 465 (2008).
- [139] E. Weidner, S. Combrié, N.-V.-Q. Tran, A. D. Rossi, J. Nagle, S. Cassette, A. Talneau, and H. Benisty. "Achievement of ultrahigh quality factors in GaAs photonic crystal membrane nanocavity." *Applied Physics Letters* **89**, 221104 (2006).
- [140] B. Song, S. Noda, T. Asano, and Y. Akahane. "Ultra-high-Q photonic double-heterostructure nanocavity." *Nature Materials* **4**, 207 (2005).

- [141] F. S. F. Brossard, X. L. Xu, D. A. Williams, M. Hadjipanayi, M. Hugues, M. Hopkinson, X. Wang, and R. A. Taylor. "Strongly coupled single quantum dot in a photonic crystal waveguide cavity." *Applied Physics Letters* **97**, 111101 (2010).
- [142] S. Gehrsitz, F. K. Reinhart, C. Gourgon, N. Herres, A. Vonlanthen, and H. Sigg. "The refractive index of $\text{Al}_x\text{Ga}_{1-x}\text{As}$ below the band gap: accurate determination and empirical modeling." *Journal of Applied Physics* **87**, 7825 (2000).
- [143] A. Taflove. *Computational Electrodynamics – The Finite-Difference Time-Domain Method*. Artech House (1995).
- [144] K. Yee. "Numerical solution of initial boundary value problems involving Maxwell's equations in isotropic media." *IEEE Transactions on Antennas and Propagation* **14**, 302 (1966).
- [145] R. Courant, K. Friedrichs, and H. Lewy. "Über die partiellen Differenzgleichungen der mathematischen Physik." *Mathematische Annalen* **100**, 32 (1928).
- [146] J.-P. Berenger. "A perfectly matched layer for the absorption of electromagnetic waves." *Journal of Computational Physics* **114**, 185 (1994).
- [147] S. Dey and R. Mittra. "Efficient computation of resonant frequencies and quality factors of cavities via a combination of the finite-difference time-domain technique and the Pade approximation." *IEEE Microwave and Guided Wave Letters* **8**, 415 (1998).
- [148] V. A. Mandelshtam and H. S. Taylor. "Harmonic inversion of time signals and its applications." *The Journal of Chemical Physics* **107**, 6756 (1997).
- [149] S. Johnson and J. Joannopoulos. "Block-iterative frequency-domain methods for Maxwell's equations in a planewave basis." *Optics Express* **8**, 173 (2001).
- [150] A. Cho and J. Arthur. "Molecular beam epitaxy." *Progress in Solid State Chemistry* **10**, 157 (1975).
- [151] M. A. Herman and H. Sitter. "MBE growth physics: application to device technology." *Microelectronics Journal* **27**, 257 (1996).
- [152] D. Leonard, M. Krishnamurthy, S. Fafard, J. L. Merz, and P. M. Petroff. "Molecular-beam epitaxy growth of quantum dots from strained coherent uniform islands of InGaAs on GaAs." *Journal of Vacuum Science & Technology B* **12**, 1063 (1994).
- [153] M. Tanaka and H. Sakaki. "Atomistic models of interface structures of $\text{GaAs} - \text{Al}_x\text{Ga}_{1-x}\text{As}$ ($x = 0.2-1$) quantum wells grown by interrupted and uninterrupted MBE." *Journal of Crystal Growth* **81**, 153 (1987).

- [154] R. Fornari and L. Sorba (editors). *Crystal growth of materials for energy production and energy-saving applications*. Edizioni ETS (2001).
- [155] F. C. Frank and J. H. van der Merwe. “One-dimensional dislocations. I. Static theory.” *Proceedings of the Royal Society of London A* **198**, 205 (1949).
- [156] M. Kasu and N. Kobayashi. “Surface diffusion of AlAs on GaAs in metalorganic vapor phase epitaxy studied by high-vacuum scanning tunneling microscopy.” *Applied Physics Letters* **67**, 2842 (1995).
- [157] E. Bauer. “Phänomenologische Theorie der Kristallabscheidung an Oberflächen. I.” *Zeitschrift für Kristallographie* **110**, 372 (1958).
- [158] D. J. Eaglesham and M. Cerullo. “Dislocation-free Stranski-Krastanow growth of Ge on Si(100).” *Physical Review Letters* **64**, 1943 (1990).
- [159] I. N. Stranski and L. von Krastanow. *Akademie der Wissenschaften und der Literatur in Mainz. Abhandlungen der Mathematisch-Naturwissenschaftlichen Klasse* **146**, 797 (1939).
- [160] D. Leonard, K. Pond, and P. M. Petroff. “Critical layer thickness for self-assembled InAs islands on GaAs.” *Physical Review B* **50**, 11687 (1994).
- [161] V. A. Shchukin and D. Bimberg. “Spontaneous ordering of nanostructures on crystal surfaces.” *Review of Modern Physics* **71**, 1125 (1999).
- [162] Q. Xie, P. Chen, and A. Madhukar. “InAs island-induced-strain driven adatom migration during GaAs overlayer growth.” *Applied Physics Letters* **65**, 2051 (1994).
- [163] A. N. Vamivakas and M. Atatüre. “Photons and (artificial) atoms: an overview of optical spectroscopy techniques on quantum dots.” *Contemporary Physics* **51**, 17 (2010).
- [164] K. Hjort, J. Soderkvist, and J.-A. Schweitz. “Gallium arsenide as a mechanical material.” *Journal of Micromechanics and Microengineering* **4**, 1 (1994).
- [165] W. Bogaerts, V. Wiaux, D. Taillaert, S. Beckx, B. Luyssaert, P. Bienstman, and R. Baets. “Fabrication of photonic crystals in silicon-on-insulator using 248-nm deep UV lithography.” *IEEE Journal of Selected Topics in Quantum Electronics* **8**, 928 (2002).
- [166] K. Kurihara, K. Iwadate, H. Namatsu, M. Nagase, H. Takenaka, and K. Murase. “An electron beam nanolithography system and its application to Si nanofabrication.” *Japanese Journal of Applied Physics* **34**, 6940 (1995).
- [167] S. Matsui. “Nanostructure fabrication using electron beam and its application to nanometer devices.” *Proceedings of the IEEE* **85**, 629 (1997).

- [168] T. Nishida, M. Notomi, R. Iga, and T. Tamamura. “Quantum wire fabrication by e-beam lithography using high-resolution and high-sensitivity e-beam resist ZEP-520.” *Japanese Journal of Applied Physics* **31**, 4508 (1992).
- [169] K. Yamaguchi, H. Ozaki, A. Hirao, N. Hirose, Y. Harada, Y. Uzawa, M. Sekine, S. Yoshimori, and M. Kawamura. “New positive EB resist with strong resistance to plasma damage.” *Journal of The Electrochemical Society* **139**, L33 (1992).
- [170] T. Stomeo, M. Grande, A. Quattieri, A. Passaseo, A. Salhi, M. D. Vittorio, D. Biallo, A. D’orazio, M. D. Sario, V. Marrocco, V. Petruzzelli, and F. Prudeniano. “Fabrication of force sensors based on two-dimensional photonic crystal technology.” *Microelectronic Engineering* **84**, 1450 (2007).
- [171] D. M. Tanenbaum, C. W. Lo, M. Isaacson, H. G. Craighead, M. J. Rooks, K. Y. Lee, W. S. Huang, and T. H. P. Chang. “High resolution electron beam lithography using ZEP-520 and KRS resists at low voltage.” *Journal of Vacuum Science & Technology B* **14**, 3829 (1996).
- [172] D. A. Czaplewski and L. E. Ocola. “Increased pattern transfer fidelity of ZEP 520A during reactive ion etching through chemical modifications by additional dosing of the electron beam resist.” *Journal of Vacuum Science & Technology B* **29**, 021601 (2011).
- [173] K. Koshelev, M. A. Mohammad, T. Fito, K. L. Westra, S. K. Dew, and M. Stepanova. “Comparison between ZEP and PMMA resists for nanoscale electron beam lithography experimentally and by numerical modeling.” *Journal of Vacuum Science & Technology B* **29**, 06F306 (2011).
- [174] A. Grill. *Cold Plasma in Materials Fabrication*. IEEE Press (1994).
- [175] R. J. Shul, G. B. McClellan, R. D. Briggs, D. J. Rieger, S. J. Pearton, C. R. Abernathy, J. W. Lee, C. Constantine, and C. Barratt. “High-density plasma etching of compound semiconductors.” *Journal of Vacuum Science & Technology A* **15**, 633 (1997).
- [176] S. Combr e, S. Bansropun, M. Lecomte, O. Parillaud, S. Cassette, H. Benisty, and J. Nagle. “Optimization of an inductively coupled plasma etching process of GaInP/GaAs based material for photonic band gap applications.” *Journal of Vacuum Science & Technology B* **23**, 1521 (2005).
- [177] M. Balooch, D. R. Olander, and W. J. Siekhaus. “The thermal and ion-assisted reactions of GaAs(100) with molecular chlorine.” *Journal of Vacuum Science & Technology B* **4**, 794 (1986).

- [178] R. Braive, L. L. Gratiot, S. Guilet, G. Patriarche, A. Lemaitre, A. Beveratos, I. Robert-Philip, and I. Sagnes. “Inductively coupled plasma etching of GaAs suspended photonic crystal cavities.” *Journal of Vacuum Science & Technology B* **27**, 1909 (2009).
- [179] E. L. Hu and R. E. Howard. “Reactive ion etching of GaAs in a chlorine plasma.” *Journal of Vacuum Science & Technology B* **2**, 85 (1984).
- [180] S. Golka, M. Arens, M. Reetz, T. Kwapien, S. Bouchoule, and G. Patriarche. “Time-multiplexed, inductively coupled plasma process with separate SiCl_4 and O_2 steps for etching of GaAs with high selectivity.” *Journal of Vacuum Science & Technology B* **27**, 2270 (2009).
- [181] S. Golka, S. Schartner, W. Schrenk, and G. Strasser. “Low bias reactive ion etching of GaAs with a $\text{SiCl}_4/\text{N}_2/\text{O}_2$ time-multiplexed process.” *Journal of Vacuum Science & Technology B* **25**, 839 (2007).
- [182] S. Golka, C. Pflügl, W. Schrenk, and G. Strasser. “Quantum cascade lasers with lateral double-sided distributed feedback grating.” *Applied Physics Letters* **86**, 111103 (2005).
- [183] P. Collot, T. Diallo, and J. Canteloup. “Dry-etch monitoring of III–V heterostructures using laser reflectometry and optical emission spectroscopy.” *Journal of Vacuum Science & Technology B* **9**, 2497 (1991).
- [184] S. E. Hicks, W. Parkes, J. A. H. Wilkinson, and C. D. W. Wilkinson. “Reflectance modeling for in situ dry etch monitoring of bulk SiO_2 and III–V multilayer structures.” *Journal of Vacuum Science & Technology B* **12**, 3306 (1994).
- [185] H. Moussa, R. Daneau, C. Mériadec, L. Manin, I. Sagnes, and R. Raj. “Deep in situ dry-etch monitoring of III-V multilayer structures using laser reflectometry and reflectivity modeling.” *Journal of Vacuum Science & Technology A* **20**, 748 (2002).
- [186] H. Jiang and J. Sabarinathan. “Effects of coherent interactions on the sensing characteristics of near-infrared gold nanorings.” *The Journal of Physical Chemistry C* **114**, 15243 (2010).
- [187] M. Voncken, J. Schermer, G. Bauhuis, P. Mulder, and P. Larsen. “Multiple release layer study of the intrinsic lateral etch rate of the epitaxial lift-off process.” *Applied Physics A* **79**, 1801 (2004).
- [188] C. A. Schneider, W. S. Rasband, and K. W. Eliceiri. “NIH Image to ImageJ: 25 years of image analysis.” *Nature Methods* **9**, 671 (2012).
- [189] F. Nikolajeff, J. Bengtsson, M. Larsson, M. Ekberg, and S. Hård. “Measuring and modeling the proximity effect in direct-write electron-beam lithography kinoforms.” *Applied Optics* **34**, 897 (1995).

- [190] C. Hedlund, H. Blom, and S. Berg. “Microloading effect in reactive ion etching.” *Journal of Vacuum Science & Technology A* **12**, 1962 (1994).
- [191] A. Javan, W. R. Bennett, and D. R. Herriott. “Population inversion and continuous optical maser oscillation in a gas discharge containing a He-Ne mixture.” *Physical Review Letters* **6**, 106 (1961).
- [192] A. White and J. Rigden. “Continuous gas maser operation in the visible.” *Proceedings of the IRE* **50**, 1697 (1962).
- [193] M. Czerny and A. F. Turner. “Über den Astigmatismus bei Spiegelspektrometern.” *Zeitschrift für Physik* **61**, 792 (1930).
- [194] S. Cova, M. Ghioni, A. Lacaita, C. Samori, and F. Zappa. “Avalanche photodiodes and quenching circuits for single-photon detection.” *Applied Optics* **35**, 1956 (1996).
- [195] C. Santori, G. S. Solomon, M. Pelton, and Y. Yamamoto. “Time-resolved spectroscopy of multiexcitonic decay in an InAs quantum dot.” *Physical Review B* **65**, 073310 (2002).
- [196] R. Brown and R. Twiss. “A test of a new type of stellar interferometer on Sirius.” *Nature* **178**, 1046 (1956).
- [197] H. J. Kimble, M. Dagenais, and L. Mandel. “Photon antibunching in resonance fluorescence.” *Physical Review Letters* **39**, 691 (1977).
- [198] A. Auffeves, D. Gerace, S. Portolan, A. Drezet, and M. F. Santos. “Few emitters in a cavity: from cooperative emission to individualization.” *New Journal of Physics* **13**, 093020 (2011).
- [199] A. A. Houck, D. I. Schuster, J. M. Gambetta, J. A. Schreier, B. R. Johnson, J. M. Chow, L. Frunzio, J. Majer, M. H. Devoret, S. M. Girvin, and R. J. Schoelkopf. “Generating single microwave photons in a circuit.” *Nature* **449**, 328 (2007).
- [200] A. Laucht, S. Pütz, T. Günthner, N. Hauke, R. Saive, S. Frédérick, M. Bichler, M.-C. Amann, A. W. Holleitner, M. Kaniber, and J. J. Finley. “A waveguide-coupled on-chip single-photon source.” *Physical Review X* **2**, 0111014 (2012).
- [201] Manga Rao, V. S. C. and S. Hughes. “Single quantum dot spontaneous emission in a finite-size photonic crystal waveguide: proposal for an efficient “on chip” single photon gun.” *Physical Review Letters* **99**, 193901 (2007).
- [202] R. A. Integlia, W. Song, J. Tan, and W. Jiang. “Longitudinal and angular dispersions in photonic crystals: a synergistic perspective on slow light and superprism effects.” *Journal of Nanoscience and Nanotechnology* **10**, 1596 (2010).

- [203] S. J. Dewhurst, D. Granados, D. J. P. Ellis, A. J. Bennett, R. B. Patel, I. Farrer, D. Anderson, G. A. C. Jones, D. A. Ritchie, and A. J. Shields. “Slow-light-enhanced single quantum dot emission in a unidirectional photonic crystal waveguide.” *Applied Physics Letters* **96**, 031109 (2010).
- [204] V. S. C. Manga Rao and S. Hughes. “Single quantum-dot Purcell factor and β factor in a photonic crystal waveguide.” *Physical Review B* **75**, 205437 (2007).
- [205] S.-H. Kim, G.-H. Kim, S.-K. Kim, H.-G. Park, Y.-H. Lee, and S.-B. Kim. “Characteristics of a stick waveguide resonator in a two-dimensional photonic crystal slab.” *Journal of Applied Physics* **95**, 411 (2004).
- [206] V. S. C. Manga Rao and S. Hughes. “Numerical study of exact Purcell factors in finite-size planar photonic crystal waveguides.” *Optics Letters* **33**, 1587 (2008).
- [207] J. Hendrickson, B. C. Richards, J. Sweet, S. Mosor, C. Christenson, D. Lam, G. Khitrova, H. M. Gibbs, T. Yoshie, A. Scherer, O. B. Shchekin, and D. G. Deppe. “Quantum dot photonic-crystal-slab nanocavities: quality factors and lasing.” *Physical Review B* **72**, 193303 (2005).
- [208] A. Kiraz, P. Michler, C. Becher, B. Gayral, A. Imamoğlu, L. Zhang, E. Hu, W. V. Schoenfeld, and P. M. Petroff. “Cavity-quantum electrodynamics using a single InAs quantum dot in a microdisk structure.” *Applied Physics Letters* **78**, 3932 (2001).
- [209] B. Wild, R. Ferrini, R. Houdré, M. Mulot, S. Anand, and C. J. M. Smith. “Temperature tuning of the optical properties of planar photonic crystal microcavities.” *Applied Physics Letters* **84**, 846 (2004).
- [210] C. H. Lin, H. S. Lin, C. C. Huang, S. K. Su, S. D. Lin, K. W. Sun, C. P. Lee, Y. K. Liu, M. D. Yang, and J. L. Shen. “Temperature dependence of time-resolved photoluminescence spectroscopy in InAs/GaAs quantum ring.” *Applied Physics Letters* **94**, 183101 (2009).
- [211] S. Strauf, K. Hennessy, M. T. Rakher, Y.-S. Choi, A. Badolato, L. C. Andreani, E. L. Hu, P. M. Petroff, and D. Bouwmeester. “Self-tuned quantum dot gain in photonic crystal lasers.” *Physical Review Letters* **96**, 127404 (2006).
- [212] S. Strauf, N. G. Stoltz, M. T. Rakher, L. A. Coldren, P. M. Petroff, and D. Bouwmeester. “High-frequency single-photon source with polarization control.” *Nature Photonics* **1**, 704 (2007).
- [213] M. Pelton, C. Santori, J. Vučković, B. Zhang, G. S. Solomon, J. Plant, and Y. Yamamoto. “Efficient source of single photons: a single quantum dot in a micropost microcavity.” *Physical Review Letters* **89**, 233602 (2002).

- [214] T. Flissikowski, A. Hundt, M. Lowisch, M. Rabe, and F. Henneberger. “Photon beats from a single semiconductor quantum dot.” *Physical Review Letters* **86**, 3172 (2001).
- [215] S. Trumm, M. Wesseli, H. J. Krenner, D. Schuh, M. Bichler, J. J. Finley, and M. Betz. “Spin-preserving ultrafast carrier capture and relaxation in InGaAs quantum dots.” *Applied Physics Letters* **87**, 153113 (2005).
- [216] K. Kowalik, O. Krebs, A. Lemaître, B. Eble, A. Kudelski, P. Voisin, S. Seidl, and J. A. Gaj. “Monitoring electrically driven cancellation of exciton fine structure in a semiconductor quantum dot by optical orientation.” *Applied Physics Letters* **91**, 183104 (2007).
- [217] M. Kaniber, A. Neumann, A. Laucht, M. F. Huck, M. Bichler, M.-C. Amann, and J. J. Finley. “Efficient and selective cavity-resonant excitation for single photon generation.” *New Journal of Physics* **11**, 013031 (2009).
- [218] R. Warburton, C. Schaflein, D. Haft, F. Bickel, A. Lorke, K. Karrai, J. Garcia, W. Schoenfeld, and P. Petroff. “Optical emission from a charge-tunable quantum ring.” *Nature* **405**, 926 (2000).
- [219] W.-H. Chang, W.-Y. Chen, H.-S. Chang, T.-P. Hsieh, J.-I. Chyi, and T.-M. Hsu. “Efficient single-photon sources based on low-density quantum dots in photonic-crystal nanocavities.” *Physical Review Letters* **96**, 117401 (2006).
- [220] S. Laurent, S. Varoutsis, L. L. Gratiet, A. Lemaître, I. Sagnes, F. Raineri, A. Levenson, I. Robert-Philip, and I. Abram. “Indistinguishable single photons from a single-quantum dot in a two-dimensional photonic crystal cavity.” *Applied Physics Letters* **87**, 163107 (2005).
- [221] A. R. A. Chalcraft, S. Lam, D. O’Brien, T. F. Krauss, M. Sahin, D. Szymanski, D. Sanvitto, R. Oulton, M. S. Skolnick, A. M. Fox, D. M. Whittaker, H.-Y. Liu, and M. Hopkinson. “Mode structure of the L3 photonic crystal cavity.” *Applied Physics Letters* **90**, 241117 (2007).
- [222] W. Fan, Z. Hao, E. Stock, J. Kang, Y. Luo, and D. Bimberg. “Comparison between two types of photonic-crystal cavities for single-photon emitters.” *Semiconductor Science and Technology* **26**, 014014 (2011).
- [223] L. Ramunno and S. Hughes. “Disorder-induced resonance shifts in high-index-contrast photonic crystal nanocavities.” *Physical Review B* **79**, 161303 (2009).
- [224] M.-K. Kim, J.-K. Yang, Y.-H. Lee, and I.-K. Hwang. “Influence of etching slope on two-dimensional photonic crystal slab resonators.” *Journal of the Korean Physical Society* **50**, 1027 (2007).

- [225] D. Gerace and L. C. Andreani. “Effects of disorder on propagation losses and cavity Q-factors in photonic crystal slabs.” *Photonics and Nanostructures* **3**, 120 (2005).
- [226] C. F. Wang, A. Badolato, I. Wilson-Rae, P. M. Petroff, E. Hu, J. Urayama, and A. Imamoglu. “Optical properties of single InAs quantum dots in close proximity to surfaces.” *Applied Physics Letters* **85**, 3423 (2004).
- [227] J. Vučković and Y. Yamamoto. “Photonic crystal microcavities for cavity quantum electrodynamics with a single quantum dot.” *Applied Physics Letters* **82**, 2374 (2003).
- [228] Y. Akahane, T. Asano, B.-S. Song, and S. Noda. “Fine-tuned high-Q photonic-crystal nanocavity.” *Optics Express* **13**, 1202 (2005).
- [229] C. Sauvan, G. Lecamp, P. Lalanne, and J. Hugonin. “Modal-reflectivity enhancement by geometry tuning in photonic crystal microcavities.” *Optics Express* **13**, 245 (2005).
- [230] P. Lalanne, C. Sauvan, and J. Hugonin. “Photon confinement in photonic crystal nanocavities.” *Laser & Photonics Reviews* **2**, 514 (2008).
- [231] E. Waks and J. Vučković. “Coupled mode theory for photonic crystal cavity-waveguide interaction.” *Optics Express* **13**, 5064 (2005).
- [232] S. Hughes, L. Ramunno, J. F. Young, and J. E. Sipe. “Extrinsic optical scattering loss in photonic crystal waveguides: role of fabrication disorder and photon group velocity.” *Physical Review Letters* **94**, 033903 (2005).
- [233] M. Lončar, J. Vučković, and A. Scherer. “Methods for controlling positions of guided modes of photonic-crystal waveguides.” *Journal of the Optical Society of America B* **18**, 1362 (2001).
- [234] D. F. Dorfner, S. Iwamoto, M. Nomura, S. Nakayama, J. J. Finley, G. Abstreiter, and Y. Arakawa. “Outcoupling of light generated in a monolithic silicon photonic crystal nanocavity through a lateral waveguide.” *Japanese Journal of Applied Physics* **48**, 062003 (2009).
- [235] R. Bose, D. Sridharan, G. S. Solomon, and E. Waks. “Observation of strong coupling through transmission modification of a cavity-coupled photonic crystal waveguide.” *Optics Express* **19**, 5398 (2011).
- [236] A. Faraon, E. Waks, D. Englund, I. Fushman, and J. Vučković. “Efficient photonic crystal cavity-waveguide couplers.” *Applied Physics Letters* **90**, 073102 (2007).
- [237] D. Englund, A. Faraon, B. Zhang, Y. Yamamoto, and J. Vučković. “Generation and transfer of single photons on a photonic crystal chip.” *Optics Express* **15**, 5550 (2007).

- [238] M. Kaniber, A. Laucht, A. Neumann, J. M. Villas-Bôas, M. Bichler, M.-C. Amann, and J. J. Finley. “Investigation of the nonresonant dot-cavity coupling in two-dimensional photonic crystal nanocavities.” *Physical Review B* **77**, 161303 (2008).
- [239] U. Hohenester, A. Laucht, M. Kaniber, N. Hauke, A. Neumann, A. Mohtashami, M. Seliger, M. Bichler, and J. J. Finley. “Phonon-assisted transitions from quantum dot excitons to cavity photons.” *Physical Review B* **80**, 201311 (2009).
- [240] M. Winger, T. Volz, G. Tarel, S. Portolan, A. Badolato, K. J. Hennessy, E. L. Hu, A. Beveratos, J. J. Finley, V. Savona, and A. m. c. Imamoglu. “Explanation of photon correlations in the far-off-resonance optical emission from a quantum-dot cavity–system.” *Physical Review Letters* **103**, 207403 (2009).
- [241] A. Laucht, M. Kaniber, A. Mohtashami, N. Hauke, M. Bichler, and J. J. Finley. “Temporal monitoring of nonresonant feeding of semiconductor nanocavity modes by quantum dot multiexciton transitions.” *Physical Review B* **81**, 241302 (2010).
- [242] M. Calic, P. Gallo, M. Felici, K. A. Atlasov, B. Dwir, A. Rudra, G. Biasiol, L. Sorba, G. Tarel, V. Savona, and E. Kapon. “Phonon-mediated coupling of InGaAs/GaAs quantum-dot excitons to photonic crystal cavities.” *Physical Review Letters* **106**, 227402 (2011).
- [243] A. Laucht, N. Hauke, A. Neumann, T. Günthner, F. Hofbauer, A. Mohtashami, K. Müller, G. Böhm, M. Bichler, M.-C. Amann, M. Kaniber, and J. J. Finley. “Nonresonant feeding of photonic crystal nanocavity modes by quantum dots.” *Journal of Applied Physics* **109**, 102404 (2011).
- [244] S. Ates, S. M. Ulrich, A. Ulhaq, S. Reitzenstein, A. Loeffler, S. Hoefling, A. Forchel, and P. Michler. “Non-resonant dot-cavity coupling and its potential for resonant single-quantum-dot spectroscopy.” *Nature Photonics* **3**, 724 (2009).
- [245] A. Faraon, D. Englund, I. Fushman, J. Vučković, N. Stoltz, and P. Petroff. “Local quantum dot tuning on photonic crystal chips.” *Applied Physics Letters* **90**, 213110 (2007).
- [246] J. J. Finley, M. Sabathil, P. Vogl, G. Abstreiter, R. Oulton, A. I. Tartakovskii, D. J. Mowbray, M. S. Skolnick, S. L. Liew, A. G. Cullis, and M. Hopkinson. “Quantum-confined Stark shifts of charged exciton complexes in quantum dots.” *Physical Review B* **70**, 201308 (2004).
- [247] D. A. B. Miller, D. S. Chemla, T. C. Damen, A. C. Gossard, W. Wiegmann, T. H. Wood, and C. A. Burrus. “Band-edge electroabsorption in quantum well structures: the quantum-confined Stark effect.” *Physical Review Letters* **53**, 2173 (1984).
- [248] P. W. Fry, I. E. Itskevich, D. J. Mowbray, M. S. Skolnick, J. J. Finley, J. A. Barker, E. P. O’Reilly, L. R. Wilson, I. A. Larkin, P. A. Maksym, M. Hopkinson, M. Al-Khafaji, J. P. R.

- David, A. G. Cullis, G. Hill, and J. C. Clark. “Inverted electron-hole alignment in InAs-GaAs self-assembled quantum dots.” *Physical Review Letters* **84**, 733 (2000).
- [249] M. Sabathil, S. Hackenbuchner, S. Birner, J. A. Majewski, P. Vogl, and J. J. Finley. “Theory of vertical and lateral Stark shifts of excitons in quantum dots.” *physica status solidi (c)* **0**, 1181 (2003).
- [250] I.-H. Tan, G. L. Snider, L. D. Chang, and E. L. Hu. “A self-consistent solution of Schrödinger–Poisson equations using a nonuniform mesh.” *Journal of Applied Physics* **68**, 4071 (1990).
- [251] N. Braslau. “Ohmic contacts to GaAs.” *Thin Solid Films* **104**, 391 (1983).
- [252] P. Liou and H.-C. Yung. US Patent No 6 150 274 (2000).
- [253] T. Ohno and K. Shiraishi. “First-principles study of sulfur passivation of GaAs(001) surfaces.” *Physical Review B* **42**, 11194 (1990).
- [254] Y.-H. Kuo, Y. K. Lee, Y. Ge, S. Ren, J. Roth, T. Kamins, D. Miller, and J. Harris. “Quantum-confined Stark effect in Ge/SiGe quantum wells on Si for optical modulators.” *IEEE Journal of Selected Topics in Quantum Electronics* **12**, 1503 (2006).
- [255] C. Y. Ngo, S. F. Yoon, W. J. Fan, and S. J. Chua. “Effects of size and shape on electronic states of quantum dots.” *Physical Review B* **74**, 245331 (2006).
- [256] A. Chutinan, M. Okano, and S. Noda. “Wider bandwidth with high transmission through waveguide bends in two-dimensional photonic crystal slabs.” *Applied Physics Letters* **80**, 1698 (2002).
- [257] R. Wilson, T. J. Karle, I. Moerman, and T. F. Krauss. “Efficient photonic crystal Y-junctions.” *Journal of Optics A* **5**, S76 (2003).
- [258] M. Ayre, T. Karle, L. Wu, T. Davies, and T. Krauss. “Experimental verification of numerically optimized photonic crystal injector, Y-splitter, and bend.” *IEEE Journal on Selected Areas in Communications* **23**, 1390 (2005).

